Università degli Studi di Ferrara

DOTTORATO DI RICERCA IN FISICA
CICLO XXX

COORDINATORE: Prof. Vincenzo Guidi

# Hysteretic magnetic behavior of AuCo nanocomposite systems

Settore Scientifico Disciplinare FIS/03

**Dottorando**

**Dott. Chinni Federico**

**Tutori**

**Dott. Spizzo Federico**
**Dott. Del Bianco Lucia**

Anni 2014/2017

# Contents

# List of Figures

# List of Tables

# Introduction

Nowadays, an unavoidable driving force for technology advancement is the search for innovative materials tailored at the nanoscale level which often have properties dramatically different from their bulk scale counterparts. In this framework, bimetallic nanostructured materials, where two distinct metallic elements are mixed to form an alloy, can play an important role leading to new specific functions not otherwise achievable with phase-segregated mixtures. They offer, indeed, not only a simple combination or enhancement of the properties associated with their single counterparts, but also multiple functionalities and excellent properties among which catalytic, magnetic and photonic [1].

In the last decades, the dominant issue for innovative magnetic materials has been the creation of nanocomposite systems consisting of at least two different magnetic phases; generally, ferromagnetic nanosized particles distributed either in a non-magnetic or magnetic matrix [2, 3]. This approach adds some degrees of freedom to single phase materials and allows the overcoming of their intrinsic limits because it opens the possibility of finely tailoring the magnetic anisotropy and, hence, the overall hysteretic behavior. In this context, well-known examples are the Fe-rich [4] and the NdFeB-based [5] crystalline alloys composed of two different ferromagnetic phases so intimately mixed at the nanoscale as to be coupled by magnetic exchange interaction, which results in outstanding soft and hard magnetic properties, respectively. Moreover, magnetic nanocomposite systems offer fascinating implications for magneto-recording and spintronics applications. For instance, the magnetic exchange interaction between a ferromagnetic layer and an antiferromagnetic one is efficiently exploited to tune the anisotropy of the former and, thus, to control the magnetization reversal process, which represents a strategic goal in the construction of modern magnetoresistive devices [6, 7, 8, 9, 10, 11, 12]. For the same purpose, ferromagnetic soft-hard exchange-coupled composites are among the most investigated systems, allowing the control of the strength and direction of the hard phase anisotropy and favoring a faster magnetization switching and a decrease in the switching field [13, 14]. In layered materials, the substrate itself can be considered as a main component of the system, able to affect the magnetic behavior of the on-top magnetic film; in this perspective, properly engineered architectures of substrate plus underlayers are employed to govern the film growth and the microstructure and, hence, the magnetic properties [15]. A further scenario is that in which a mechanical stress is produced in the magnetic film because of the bonding with the substrate [16], opening the possibility of tuning the magnetic anisotropy via magneto-elastic coupling [17, 18, 19]. Tailoring the anisotropy has a crucial role in the field of magnetic sensors where, moreover, flexible substrates are now often employed [20, 21]

Recently, alloys and intermetallic compounds of Au with magnetic $3d$ elements have received a great scientific interest because of their magnetic, magneto-optical and magnetoplasmonics properties [22, 23, 24, 25, 26, 27]. In this rich scientific framework, in collaboration with Prof. G. Mattei of the Padua University, we have studied $AuCo$ alloyed systems with different concentration ratio of the two metals, in form of both continuous films with different thickness, and Nano Holes Arrays (NHA). Intersestingly, $Au$ and $Co$ do not form a binary alloy [28], since they are immiscible as bulk phases at temperatures below $693\,K$ [29] (almost $15\,\%$ lattice mismatch exists between $Au$ and $Co$), and, thus, they are ideal candidates to fabricate nanocomposite materials prepared by means of the physical vapor deposition methods, such as sputtering co-deposition, which work far from the thermodynamic equilibrium [28]. In literature, the study of $AuCo$ nanocomposite systems has been substantially proposed to explore material designs allowing for further optimization of the magneto-plasmonics properties such as the modulation of surface plasmon polariton modes [25, 26]. In these structures the magneto-optical active medium is spread through the whole thickness of the film in form of different nanocluster-matrix aggregates and it guarantees higher performances with respect to multilayers systems [30]. The attention has been focused on the factors which strongly condition the optical and magneto-optical response such as morphology, $Co$ concentrartion, nanoparticle size, and interparticle distance. Neverthless a comprehensive and exhaustive magnetic investigation is still lacking. The following research work is mainly focused on the magnetic properties of these $AuCo$ nanocomposite structures studied as function of both the concentration ratio between the two metals and the thickness. In addition, thanks to the investigation of the NHA systems, this research work highlights how

the nanostructuring process influences the overall magnetic behavior. In detail, the thesis is structured as described below.
Chapter 1 presents the possible the sources of magnetic anisotropy which may affect the hysteretic properties and, hence, the magnetization reorentation process of the investigated samples. Chapter 2 describes the experimental techniques employed for the characterization of the magnetic properties of the studied systems with focus on those exploited in the laboratories of the Department of Physics and Earth Sciences of the University of Ferrara. Chapter 3 is mainly dedicated to the analysis of the magnetic properties of $30\,nm$-thick $AuCo$ continuous films with different atomic ratio of the constituent metals whilst Chapter 4 focuses on the study of $80\,nm$-thick $AuCo$ continuous films with the same nominal stoichiometry of the thinner ones in order to highlight how the thickness affects the magnetic response of our samples. Chapter 5 points the attention on the hysteretic properties of $AuCo$ nanostructures in form of Nano Holes Array systems deposited in the same deposition batch of the thicker continuous films; the aim is to study the influence of the anisotropy induced by the nanostructuration step on the magnetization reversal process. Finally, the chapter dedicated to the conclusions summarizes the main results of this work.

Chapter 1

# Magnetic anisotropies

The study of new phenomena during the last years has compelled to investigate new properties at nano-scale level [31]. One of the simplest nanostructures is a thin continuous film where two dimensions may be very large (even of the order of centimeters) but the other is usually of the order of hundreds of nanometers. Continuous magnetic films play an important role in the field of spintronics [32, 33, 34, 35] and applications extend from tunnel junction [36, 37] to the study of switching dynamics [38]. Studies of materials with two or even three of the dimensions in the nanometer scale are becoming of great scientific interest aiming to the development of new devices for technologic applications, such as the storage media for reading and storing of information in magnetic RAMs [39].

In all of the examples, the functionalities of the systems are controlled by the size confinement effect, namely by the influence of the magnetic shape anisotropy. More in general, the overall anisotropy of a magnetic material may also include other contributions, as well, such as magnetocrystalline anisotropy, magnetoelastic anisotropy and exchange anisotropy. The fine interplay of all these terms rules the magnetic behavior of a specific system and, accordingly, determines its potential technological use.

In the following, an overview of the types of magnetic anisotropy that are considered and/or discussed in this research work is presented.

## 1.1 Magnetocrystalline anisotropy

The magnetic anisotropy in crystalline materials manifests itself as the tendency of the magnetization vector to align itself along a preferred crystallographic direction called, for this reason, easy magnetization direction. An example is a single crystal of $Fe$, where the $< 100 >$ directions are easy axes of magnetization, whereas the $< 111 >$ directions are hard axes of magnetization [40]. This has been ascertained by the measurement of magnetization loops. In the absence of any applied external field, the magnetization prefers to lie along an easy axis, since this minimizes the magnetic energy of the system. The easy and hard directions can be distinguished by the magnetic field value that is needed to achieve magnetic saturation. This form of magnetic anisotropy is referred to as the crystal anisotropy, or magnetocrystalline anisotrpy, and it is intrinsic to the material. The magnetocrystalline anisotropy is mainly due to the spin-orbit interaction. The orientations of the electronic orbits are fixed very strongly to the lattice because of the presence of a strong orbit-lattice coupling. Through the coupling between the spin and the orbital motion of electrons, when an external magnetic field tries to reorient the spin, the orbit also tends to be reoriented, but, since the orbit is strongly coupled to the lattice, it resists the attempt to rotate the spin axis. The energy required to rotate the spin system of a domain away from the easy direction is just the energy required to overcome the spin-orbit coupling. In the case of a cubic crystal, the magnetocrystalline anisotropy energy density $\varepsilon_{mc}$ can be expressed as a series expansion of the direction cosines $\alpha_1$, $\alpha_2$, $\alpha_3$ of the magnetization direction relatively to the crystal axes [40]

$$\varepsilon_{mc} = K_0 + K_1(\alpha_1^2\alpha_2^2 + \alpha_2^2\alpha_3^2 + \alpha_3^2\alpha_1^2) + K_2(\alpha_1^2\alpha_2^2\alpha_3^2) + ... \quad , \tag{1.1}$$

where $K_0$, $K_1$, $K_2$, ... , are the anisotropy constants, which are given for a particular material at a particular temperature. The magnitude and sign of the significant anisotropy constants determine what directions are easy axes. In the case of uniaxial anisotropy, which can be found in hexagonal crystals, the energy density is a function of a single angle $\theta$ [40]:

$$\varepsilon_{mc} = K_0 + K_1 \sin^2\theta + K_2 \sin^4\theta + ... \quad . \tag{1.2}$$

Depending on the value and on the sign of the anisotropy constants, there can be an easy axis of magnetization, an easy basal plane of magnetization or an easy cone of magnetization.

The intrinsic magnetocrystalline anisotropy is not preserved in amorphous materials, since the crystal field averages to "zero" on a macroscopic scale because of the arrangement of the atoms. On a local scale, it can be assumed that there is some "crystalline" anisotropy because of nearest neighbour interactions, which will be very of a short range and, therefore, the average macroscopic magnetocrystalline anisotropy is close to, or equal to, zero [40, 41].

## 1.2 Magnetoelastic anisotropy

When the state of magnetization of a magnetic material is altered by an external magnetic field, it also experiences a change in its physical dimensions. This effect is called magnetostriction. The fractional change in length $\lambda = \delta l/l$, which expresses a strain, allows to quantify the produced effect; the value of $\lambda$ measured at magnetic saturation is the saturation magnetostriction $\lambda_S$. The magnetostriction is due to the spin-orbit coupling which is also responsible for the magnetocrystalline anisotropy and they are both intrinsically related [41]. Although the magnetostrictive strain is small in most magnetic materials, the existence of magnetostriction means that an applied mechanical stress can create a new source of magnetic anisotropy: the magnetoelastic anisotropy. The amount of magnetostrictive strain exhibited by a crystal along a fixed direction depends on the direction of the magnetization; if we impose an additional strain by applying a mechanical stress, we expect that the direction of the magnetization will change. The reason can be explained by a general argument based on Le Chatelier's principle. If the crystal has a positive $\lambda_S$ for a specific direction, it will elongate when magnetized; an applied tensile stress, which tends to elongate it along the same direction, will therefore increase the magnetization determining the appearance of an easy axis, whilst an applied compressive stress will decrease the magnetization. The resultant anisotropy can be expressed by the magnetoelastic energy density $\varepsilon_{me}$, which for a cubic crystal takes the form [40]

$$\begin{aligned}\varepsilon_{me} = &-\frac{3}{2}\lambda_S^{100}\sigma(\alpha_1^2\gamma_1^2 + \alpha_2^2\gamma_2^2 + \alpha_3^2\gamma_3^2) \\ &- 3\lambda_S^{111}\sigma(\alpha_1\alpha_2\gamma_1\gamma_2 + \alpha_2\alpha_3\gamma_2\gamma_3 + \alpha_3\alpha_1\gamma_3\gamma_1)\ ,\end{aligned} \tag{1.3}$$

where $\alpha_1$, $\alpha_2$, $\alpha_3$ are the direction cosines of the magnetization relatively to the crystal axes; $\gamma_1$, $\gamma_2$, $\gamma_3$ are the direction cosines of the applied stress $\sigma$ and $\lambda_S^{100}$, $\lambda_S^{111}$ are the saturation magnetostriction in the indicated crystallographic directions. When the magnetostriction is isotropic, as in the case of amorphous materials [40, 41], the equation can be reduced to a simple form [40]

$$\varepsilon_{me} = \frac{3}{2}\lambda_S\sigma\sin^2\theta\ , \tag{1.4}$$

where $\theta$ is the angle between the magnetization and the applied stress. Basically, the effect of stress in magnetostrictive materials could be to induce a uniaxial magnetoelastic anisotropy. This source of magnetic anisotropy has an important role in sputtered deposited continuous films, where, in general, random micro-strains occur because of the growth process [42]. The interaction between stress and magnetic properties generally depends on the details of composition, growth texture, growth morphology (wheter the film is grown in columnar fashion or as equiaxial crystallites), grain size and thickness of the system under consideration [43]. Also the mechanical properties of the film-substrate system [109] and the working temperature [44] plays a fundamental role, actually. The strength of the stress significantly affect the magnetic properties of the system leading to modify its hysteretic behavior such as the loop shape and the coercive field [15]. In some cases, the enhancement of the stress present in the system could lead to the insurgence of perpendicular magnetic anisotropy (PMA). The PMA contribution to the magnetization reversal process can be related to the phenomena called spin reorentation transition (SRT) [45, 46, 47, 48, 49] and inverse SRT [50, 51]; effects consisting of the transition from out-of-plane to in-plane and from in-plane to out-of-plane magnetization, respectively. Other magnetic behaviors, related to the stress and, more generally to the magnetoelastic anisotropy, are the formation of stripe domains structure [42, 51, 52] and the formation of magnetization ripple [42]. Hence, stress has has significant consequences for both magnetic thin films devices' fabrication and performance. Moreover, in disordered systems, the orientation of the magnetization is largely determined by magnetoelastic anisotropy term [51]; hence, it has a crucial role in determining the overall hysteretic behavior of such magnetic structures, as, for example, in the case of sputtered $CoFeB$ films grown on flexible substrates [43].

## 1.3 Shape anisotropy

The magnetostatic energy originates from the classical interaction among the elementary magnetic dipoles which constitute a ferromagnet: being the anologous of the electrostatic energy for electric charges, it represents the energy contribution coming from the fact that each dipole is immersed in the magnetic field $H_d$ created by the other dipoles, called demagnetized field [41]. For a specimen with magnetization $\mathbf{M}$, the magnetostatic energy $E_{ms}$ can be evalueted as [40]

$$E_{ms} = -\frac{1}{8\pi}\int_V \mathbf{M}\cdot\mathbf{H}_d \, d\tau \ . \tag{1.5}$$

where the integration is over the volume of the sample. This energy term contributes to define the magnetic microstructure of a ferromagnetic material, but it can also be a source of anisotropy in small particles: the magnetostatic energy depends on the direction of the magnetization because the shape of the particles contributes in determining the field produced by the magnetization itself [40]. In the case of an ellipsoidal particle with uniform magnetization $\mathbf{M}$, the demagnetizing field can be expressed as [41]

$$\mathbf{H}_d = -\mathcal{N}_d \mathbf{M} \; , \tag{1.6}$$

where $\mathcal{N}_d$ is the demagnetizing tensor, characterized by an unitary trace. When the Cartesian coordinates are chosen along the principal axes of the ellipsoid the energy density becomes

$$\varepsilon_{ms} = \frac{1}{2}(N_x M_x^2 + N_y M_y^2 + N_z M_z^2) \; , \tag{1.7}$$

where $N_x$, $N_y$ and $N_z$ are called the demagnetizing factors. If we consider a prolate spheroid, as shown in figure 1.1 [40], the magnetostatic energy density will be given by

$$\begin{aligned} \varepsilon_{ms} &= \frac{1}{2}\left[(M\sin\theta)^2 N_a + (M\cos\theta)^2 N_c\right] \\ &= \frac{1}{2}\left[M^2 N_c + M^2 (N_a - N_c)\sin^2\theta\right] \; . \end{aligned} \tag{1.8}$$

where $\theta$ is the angle between the magnetization $\mathbf{M}$ and the third axis of length $c$. This expression for the magnetostatic energy density has an angle-dependent term of exactly the same form of an uniaxial anisotropy energy density. The long axis of the specimen plays the same role of an easy axis, and the shape anisotropy constant $K_s$ is given by

$$K_{ms} = \frac{1}{2} M^2 (N_a - N_c) \; . \tag{1.9}$$

It is evident that this coefficient depends on both the $c/a$ ratio and the intensity of the magnetization. If $c$ shrinks until it equals $a$, the specimen becomes spherical, $N_a = N_c$, $K_s = 0$, and the shape anisotropy disappears.

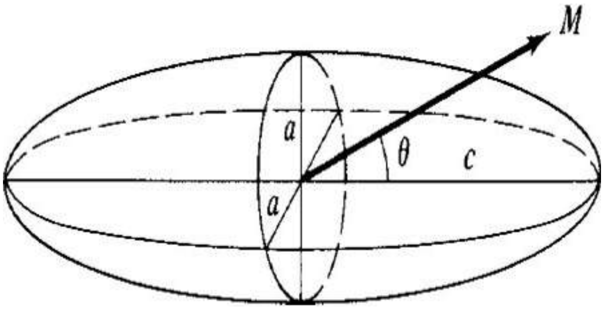

***Figure 1.1:*** *Prolate spheroid [40].*

## 1.4 Configurational anisotropy

Nanostructures arranged according to a geometrical pattern can be described as spatially ordered non-magnetic defects on a continuous thin film or as well as the counterpart of dot nanostructures [53]. The most important effect of such holes or antidots is to modify the magnetization process of the otherwise continuous film [54]. Locally, these defects produce a spatially dipolar field which depends on the array arrangement. In other words, the demagnetizing field introduced by the holes leads to a spatially variant shape anisotropy, which usually competes with the intrinsic uniaxial anisotropy of the compound, and gives rise to magnetically easy regions with respect to the applied field [55]. In this scientific framework, some works [56, 57, 58] claimed that the shape of the holes, their density (parameter related to both the diameter and the center-to-center distance of the holes) and the intrinsic anisotropy of the unpatterned film, and not the symmetry of the lattice, are the responsible of the anisotropy. On the other hand, more recent works [59, 60, 61, 62] found that the lattice symmetry plays an important role. In the case of antidots perforated in materilas with strong perpendicular anisotropy such as $Co/Pt$ multilayer [63, 64], the interplay between out of plane stray fields and antidot lattice has been used to enhance coercivity [63] and provides a promising alternative for the development of a bit-patterned media [64]. Lithographic techniques, such as Electron Beam Litography (EBL), allow designing different array arrangements as, for example, the square [65], the honeycomb [59] and the hexagonal [66] lattice geometries; each of these configurations results in different conditions for the minimization of the magnetostatic energy, showing different magnetic domain structures, which depend on the lattice pattern present in the film. Basically, each configuration could lead to a different overall magnetic behavior of the system.

Chapter 2

# Experimental Techniques

In this chapter we want review the main experimental techniques we employed for the magnetic characterization of the studied samples. This chapter is substantially divided into two sections. Section 2.1 describes the magneto-optic Kerr effect (MOKE) and the experimental setup based on it whilst section 2.2 focuses the attention on the system based on the superconductive quantum interference device (SQUID). We exploit these techniques to achieve magnetic information from both continuous films and Nano Holes Array (NHA) systems.

## 2.1 Magneto-optic Kerr effect magnetometry

The study of the magnetic properties of a material can be conducted through optics. In this case, we exploit the phenomenon of magneto-optical Kerr effect (MOKE) in order to reveal the state of magnetization of a material during an hysteresis loop. We can consider linearly polarized light (as, for example, emerging from a polarizer) as being a superposition of two circularly polarized components. We can actually distinguish two processes taking place for light propagating in a magnetized medium. First, the two circularly polarized modes propagate with different velocities inside the medium, gaining two different phase shifts that, when recombined at their exit, results in a rotation of the polarization plane of the reflected beam. Second, since the material is dichroic, it absorbs differently the two modes, hence the ellipticity effect is expected [67, 68]. These magneto-optic phenomena, namely the tilt angle $\theta_K$ of the polarization axis and the gained ellipticity $\epsilon_K$, are proportional to the net magnetization of the sample and not to the applied magnetic field as in the case of non-ferromagnetic materials [69]. The surface sensitivity of the magneto-optic Kerr effect, limited to within one absorption length of the material, typically

$\sim 20\,nm$ for most metals [70], makes this technique particularly relevant in surface and ultrathin films magnetism investigations. In this sense, if the thickness of the layer to be analyzed is compatible with this value, the information obtained will concern the whole layer. Conversely, if the thickness of the deposited film is larger, the information collected is limited to the surface layer. On the other hand, if the surface interacts in some way with what lies beneath, we can still extrapolate information relating greater depths, based on the interaction involved between the surface layer and layers located at different depth. Moreover, MOKE magnetometry has demonstrated to be a suitable probe [71] because of its capability to probe the magnetization in small regions of the sample. In particular, the magnetometer used, in combination with an optical system of lenses and a microscope with a CCD camera, allows us to measure the hysteresis loop of a specific portion of the sample surface, whose diameter can be optically tuned from $\sim 3\,mm$ down to $\sim 50\,\mu m$ thanks to the modulation of the size of the light spot used to probe the magnetization.

The Kerr effect can be observed in three different experimental configurations of the magnetization with respect to both the plane of incidence and the sample reflecting surface: the polar, the longitudinal and the transverse (or equatorial) configuration.

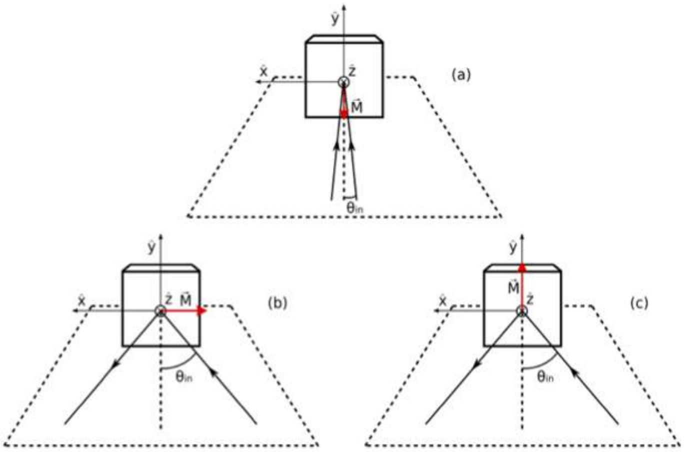

***Figure 2.1:*** *Geometries in terms of which the Kerr effect is generally described: (a) polar, (b) longitudinal an (c) transversal configuration. The plane of incidence is enclosed by the dotted line [72].*

As shown in figure 2.1(a), in a polar configuration a beam of light with linear polarization falls usually under normal incidence on a surface which is magnetized in a direction perpendicular to the surface. After reflection, the polarization has turned by an angle $\theta_K$, typically less than a degree, and some ellipticity has appeared. In the longitudinal Kerr effect 2.1(b), a beam strikes the surface under oblique incidence, this configuration is sensitive to the magnetization belonging to both the plane of incidence and the sample plane. If the polarization of the incident beam is perpendicular ($s$ polarization) or parallel ($p$ polarization) to the plane of incidence of the light, then the polarization of the reflected beam is slightly elliptical, with a major axis rotated with respect to the incident polarization by an angle generally less than a degree. The third configuration is the transverse one, where the geometry is the same as in the longitudinal case, except that the magnetization, although still in the plane of the sample surface, is perpendicular to the plane of incidence (2.1(c)) and the reflected beam is observed to change its intensity, but not rotation or ellipticity.

The MOKE measurements have been taken through the system sketched in figure 2.2.

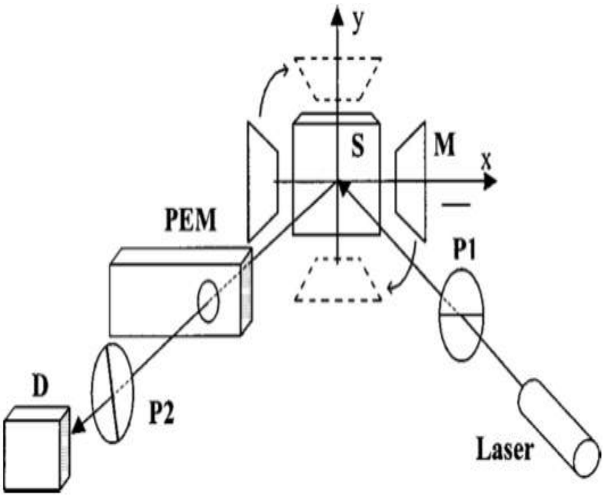

**Figure 2.2:** *A sketch of the MOKE measurements set up, taken from [73].*

The incident light beam originates from a He-Ne laser ($\lambda = 632.8\,nm$), passes through a rotatable Glan-Thompson polarizer (P1), impacts on the sample surface (S) and then it is reflected. The polarizer P1, is set so that the beam retains a $p$ polarization (parallel to the plane of incidence). The reflected light beam passes through a photoelastic modulator (PEM) vibrating at an angular frequency $\omega = 50\,kHz$, then through a second rotatable Glan-Thompson polarizer (P2) and finally it is detected by a photodiode (D). P2 is set almost at extinction with respect to P1, namely it is positioned at an angle $\alpha = 5°$ with respect to the extinction axis. The PEM is actually used for modulating the polarization of the light beam at the set frequency; the PEM function is simply based on the photoelastic effect, in which a mechanically stressed sample exhibits birefringence proportional to the resulting strain. Given the PEM optical axis, a linear polarization of the light parallel to that axis has a slightly different speed from that of a linear polarization perpendicular to the same axis. Defining $\Delta n$ the difference between the two indices of refraction, $\Delta n = A \cos \omega t$ where $A$ is proportional to the amplitude of the voltage applied to the piezoelectric transducer causing the vibration. As a consequence, the phase angle introduced between two waves with polarization parallel and perpendicular to the optic axis and travelling through the PEM can be written $\phi = \frac{2\pi l \Delta n}{\lambda} = \phi_0 \cos \omega t$, where $l$ is the thickness of the optical element and obviously $\phi_0 = \frac{2\pi l A}{\lambda}$. The component of the detected signal modulated at $\omega$ and $2\omega$ are measured with two lock-in amplifiers, as they contain information about $\epsilon_K$ and $\theta_K$ respectively. The sample is positioned between the two poles of an electromagnet whose voltage can be controlled via computer. The electromagnet can be rotated in order to produce a field $H$ that lies in the sample surface plane and that can be either parallel or perpendicular to the plane of incidence.

Each step of this system can now be analyzed considering that a possible representation of the light beam physical state is the one given in a bidimensional Hilbert space with a basis formed by the $s$ and $p$ polarizations. Using the Jones formalism [67, 72, 74], one can be associate a matrix to every optical element and study the light beam at the detector stage. Assuming the initial state was the one of $s$ polarization [75] (similar results are obtained if we consider $p$ polarization) the measured intensity $I$ in a first order approximation on the Fresnel reflective indices is

$$I = \alpha^2 |r_{ss}|^2 + 2\alpha |r_{ss}|^2 (\theta_K \cos\phi - \epsilon_K \sin\phi) \tag{2.1}$$

where it has been explicity written the Fresnel reflective index $r_{ss}$ relative to a $s$ polarized incident beam and $s$ polarized reflected beam. It can be noticed that $I$ is given by the sum of two main terms, where the second one includes both $\theta_K$ and $\epsilon_K$. Thus, we write both $\cos\phi$ and $\sin\phi$ in Fourier series using the Bessel functions:

$$\cos\phi = J_0(\phi_0) + 2 \sum_{m=1}^{\infty} J_{2m}(\phi_0) cos(2m\omega t) \tag{2.2}$$

$$\sin\phi = 2 \sum_{m=0}^{\infty} J_{2m+1}(\phi_0) sin[(2m+1)\omega t] \tag{2.3}$$

where $J_\psi(\phi_0)$ are the Bessel functions of $\psi$ order with $\phi_0$ as argument. Interrupting the expansion in terms of Bessel functions at their second-order, namely neglecting other terms not because subsequent orders are small, but because they will not be detected by selective lock-in amplifiers, we obtain:

$$I = I_0 + 2\alpha\theta_K|r_{ss}|^2 J_2(\phi_0)\cos(2\omega t) - 4\alpha\epsilon_K|r_{ss}|^2 J_1(\phi_0)\sin(\omega t) \tag{2.4}$$

namely a signal constituted of both constant ($I_0$) and two variable components. The two variable components are found to be proportional to the rotation $\theta_K$ and ellipticity $\epsilon_K$ and modulated at two different frequencies $2\omega$ and $\omega$, respectively. With the help of two lock-in amplifiers set at the same frequencies values, above mentioned, it is then possible to sense the two contributions, which are expected to be proportional to the longitudinal magnetization. In this sense, it is worth noting that the hysteresis loops, obtained with this technique, are typically normalized to their saturation magnetization values.

## 2.2 SQUID magnetometry

The Superconducting Quantum Interference Device (SQUID) is the main component of the quantum design Magnetic Property Measurement System (MPMS) that is recognized to be one of the most sensitive instrument for measuring magnetic properties; the intensity of the applied magnetic field, that is produced by a superconducting magnet made of wires wound in a solenoidal configuration, varies in the 0 - 50 $kOe$ range, and the sample temperature can be varied in the 2 $K$ - 400 $K$ temperature range. One of the difference between MOKE and SQUID magnetometry is that the latter allows to directly determine the overall magnetic moment of a sample in absolute units; in our case, the SQUID magnetometer is equipped with the reciprocating sample oscillation (RSO) option, that allows us to achieve a sensitivity of the order of $10^{-8}$ $emu$ [76] .

The SQUID sensor is based on the physical phenomena of flux quantization through a circuit including Josephson tunneling junction. The Josephson effect [77] is the fact that the flux change in a superconducting circuit separated by thin insulating layer is quantized. Flux quantization states that the flux inside the SQUID ring due to an external magnetic field can not change continuosly, but only in multiples of the flux quantum ($\phi_0 = h/2e = 2.7 * 10^{-15}$ $Oe/cm^2$). Thus if these flux can be counted exactly then the change can be detected very precisely and an accurate determination of the magnetization of the sample is possible.

In more details, a Josephson juntion consists of two metals separated by a very thin insulating layer (20 $\hat{A}$ or less). This insulator acts as a barrier to the flow of the electrons. Below a critical curret $I_C$, the junction offers no resistance because the electrons forming Cooper pairs can pass through the barrier by a quantum mechanical process called tunneling. Above $I_C$ becomes resistive, and a voltage develops across it. Now the total flux is the sum of the flux due to the superconducting ring and the external flux. Since the external flux is constant the flux due to the superconducting ring has to change so that the flux quantization is manteined. This is done by a superconductor which creates a screening current $J$, flowing around the loop. The screening current creates a magnetic field equal but opposite to the applied field thereby canceling it out. As the flux increases from 0 to $\phi_0/2$, the induced current increases to a maximum value and for flux values between $\phi/2$ and $\phi$, the induced current reverses direction to cancel this flux. Therefore an interference effect can be observed when the maximum current is measured as a function of the magnetic field. The critical current changes for a change of field of $10^{-7}\,Gauss$. In practice the SQUID operates with a current larger than the bias current and so the junction are normal. Hence the voltage across the SQUID is proportional to the current and therefore is periodic in flux. The change in voltage gives the change in flux. Any change in the flux can be determined by determining the number of periods of voltage that gives the integral number of flux quanta and the absolute value of the voltage gives the remaining fraction of the quantum. The total flux is obtained by adding these two values [78].

In figure 2.3, an explicative sketch of the measurement process is presented. The sample is moved through a system of superconducting detection coils which are connected to the SQUID with superconductiong wires, allowing the current from the detection coils to be persistent and to inductively couple to the circuit where the SQUID sensor is installed. To guarantee a high degree of accuracy of the measurement, to avoid the effect of external magnetic fields and to reduce the noise induces by possible fluctuations of the large magnetic field of the superconducting magnet of the magnetometer, the SQUID sensor is located within a superconducting shield, and the detection coils are installed in a second order gradiometer configuration, so in place of a single detection coils, four of them are used. The SQUID electronics produces a signal that is strictly proportional to the current flowing in the detection coils.

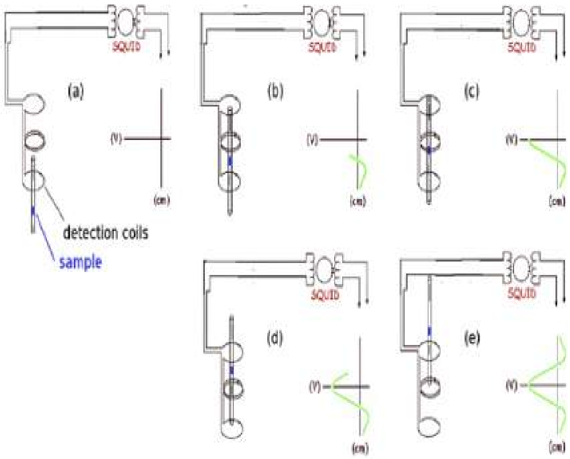

**Figure 2.3:** *A sketch of the MPMS measurements process, from (a) to (e), that brings to the development of the output voltage (in green). The picture was taken from Ref.[78].*

A measurement (figure 2.3) is performed in the MPMS by moving a sample through the superconducting detection coils. As the sample moves through the coils, the magnetic moment of the sample induces an electric current in the detection coils. Because the detection coils, the connecting wires, and the SQUID input coil form a closed superconducting loop, any change of magnetic flux in the detection coils produces a change in the persistent current in the detection circuit which is proportional to the change in magnetic flux. Since the SQUID operates as a highly linear current-to-voltage convertor, the variations in the current in the detection coils produce corresponding variations in the SQUID output voltage which are proportional to the magnetic moment of the investigated sample. In a fully calibrated system, measurements of the voltage variations from the SQUID detector as a sample is moved through the detection coils provide a highly accurate measurement of the sample's magnetic moment. The system is calibrated using a palladium sample, the susceptibility and the massof which are known. The palladium sample is subjected to a magnetization measurement and the susceptibility is calculated. Then using the known susceptibility and the calculated susceptibility from the measurement, a calibration factor is calculated.

The commercial MPMS we exploit at the laboratories of the University of Ferrara is further equipped with the RSO option. Unlike typical measurements where the sample is moved through the coils in discrete steps, the RSO option allows the sample to oscillate inside the detection coils (figure 2.4). By locking the frequency of the readout to the frequency of the oscillation, the magnetometer system can achieve the highest sensitivity described above for ultra-small magnetic signals.

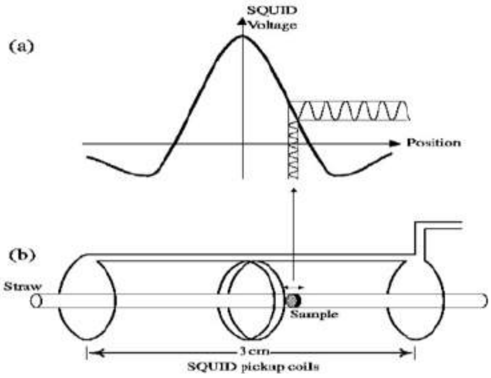

**Figure 2.4:** *Illustration of the measurement with the RSO option. (a) shows the ideal SQUID response for a dipole and (b) shows the movement of the sample within the SQUID pickup coils. The picture was taken from Ref.[76].*

In figure 2.5, the environment where the sample is placed during the measurements and the superconducting magnet are displayed. The sample is at the center of the superconducting magnet; all around the sample chamber there is the system that allows the temperature control. The temperature of the sample is fixed by balancing the heating power released by the sample chamber heater and the flux of the cold helium gas that is collected from the liquid helium reservoir where all the instrumentation (superconducting magnet, detection coils (or pick up coils, as in figure 2.5), SQUID sensor) is immersed; this guarantees that both the magnet and the SQUID electronics are in the superconducting state. The liquid helium reservoir is surrounded by a liquid nitrogen reservoir, that acts so as to reduce the liquid helium evaporation.

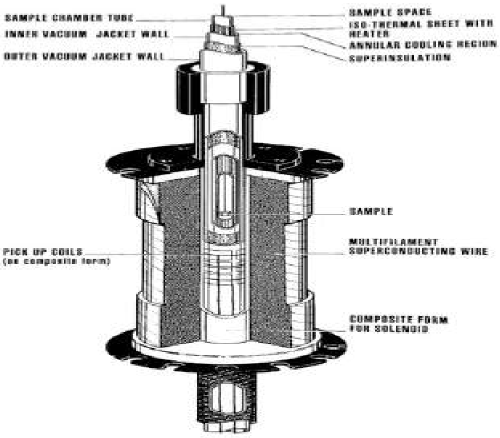

**Figure 2.5:** *The sample environment and the superconducting magnet. The picture was taken from Ref.[76].*

Chapter 3

# $30\,nm$ - thick continuous films

This chapter is mainly dedicated to the discussion of the magnetic properties of the $30\,nm$ - thick AuCo continuous films. It is divided into two sections. Section 3.1 briefly introduces the compositional and structural investigations carried out at the University of Padua while, the second one (3.2), focuses on the magnetic analyses of these samples made from both an experimental (3.2.1) and a micromagnetic (3.2.2) point of view. This in-depth study emphasizes the nanocomposite nature of the investigated samples which present peculiar hysteretic features, namely in-plane anisotropy, despite the deposition technique which favours an uniform coverage of the substrate, and crossed branches in the loops measured along the hard magnetization direction.

## 3.1 Production and composition of the AuCo samples

$30\,nm$ - thick continuous $AuCo$ films have been deposited at room temperature on natively oxidized (100)-silicon substrates by the magnetron co-sputtering technique in $Ar$ atmosphere, using a custom-built apparatus in which the metal targets have been tilted at $\sim 30°$ with respect to the axis normal to the sample plane, allowing a simultaneous deposition of the two metals. A rotating sample-holder has been employed, grounded to the deposition chamber, to favor a uniform coverage of the substrate. The $Ar$ working pressure was of $5 \times 10^{-3}\,mbar$. Au has been deposited with a $2\,inch.$ radio-frequency driven source, setting the power in the range of $28 - 55\,W$. In the case of Co (purity of $99.5\,\%$), a DC magnetron sputtering $2\,inch.$ source has been used, providing powers in the range of $48 - 96\,W$. The typical deposition rate was around $1 - 2\,\mathring{A}/s$. The source-target distance was about $18\,cm$ (see the semplified sketch in figure 3.1) [79].

**Table 3.1:** *Column 1: labels of the samples. Columns 2 and 3: Au and Co content in the films. Column 4: thickness of the films*

| Samples | Composition | | Thickness (nm) |
|---|---|---|---|
| | Au (at %) | Co (at %) | |
| $Au_2Co_1$ | 69 ± 1 | 31 ± 1 | 30 ± 2 |
| $Au_1Co_1$ | 49 ± 1 | 51 ± 1 | 28 ± 1 |
| $Au_1Co_2$ | 33 ± 1 | 67 ± 1 | 28 ± 1 |

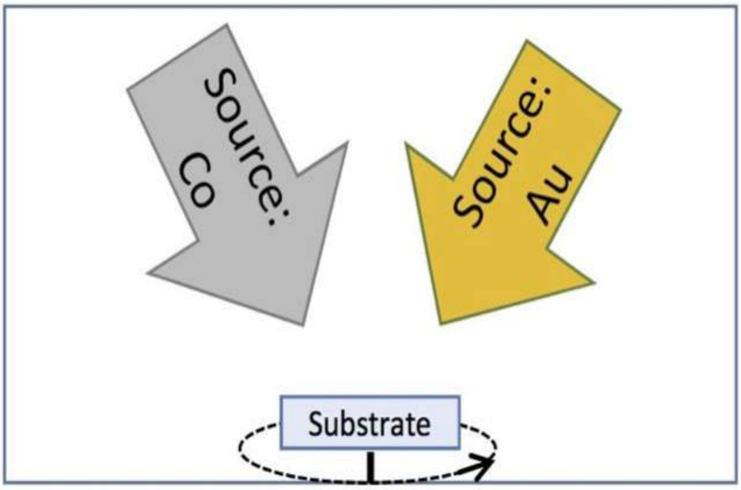

**Figure 3.1:** *The magnetron sputtering geometry for the deposition of $AuCo$ nanocomposites from Ref. [79].*

Three compositions have been considered with nominal stoichiometry 2 : 1, 1 : 1 and 1 : 2, labelled as $Au_2Co_1$, $Au_1Co_1$ and $Au_1Co_2$, respectively. As mentioned above, the nominal thickness of this set of typical $AuCo$ films is 30 $nm$; they have been coated in the same deposition batch with a $SiO_2$ cap layer, in order to prevent environmental contamination and oxidation. Continuous Co film, with thickness $(22 \pm 1)\,nm$ has been also deposited to be used as reference sample.

The films' stoichiometry has been determined by Rutherford Backscattering Spectrometry (RBS) (table 3.1) performed with a HVEC 2.5 $MeV$ Van de Graaff accelerator at Legnaro National Laboratory (LNL)-INFN, using 2 $MeV$ $\alpha$-particles at normal incidence and a scattering angle of 20°. The RBS analysis togheter with scanning electron microscope (SEM) observations in cross-section mode also provided information on their thickness (table 3.1 ).

Informations on the structure and composition of the films have been mainly acquired by Extended X-ray Absorption Fine Structure (EXAFS) investigation. To provide a full description of this analysis is beyond the scope of the present thesis and the experimental details are reported elsewhere [79, 80]. In this section, we want just to summarize the principal results. EXAFS experiments have been performed at both Au $L_3$-edge and Co $K$-edge at $T = 80\,K$ at the Italian Beamline BM08 of the European Synchrotron ESRF (Grenoble, France). As an example, the typical spectra for the $Au_1Co_2$ sample are displayed in figure 3.2(a)

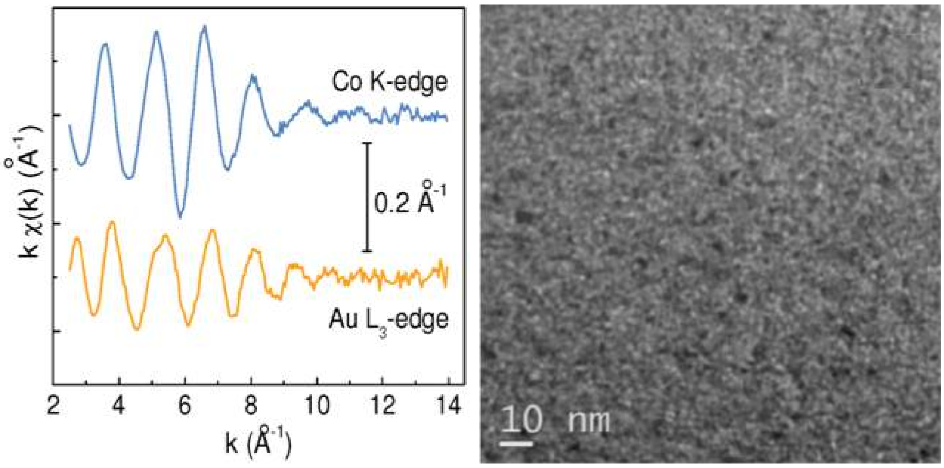

(a) (b)

**Figure 3.2:** *EXAFS spectra (a) and bright-field TEM image (b) for the $Au_1Co_2$ sample.*

In all the cases studied, the EXAFS analysis has evidenced a $Au - Co$ interatomic correlation signal unambigously revealing the formation of a $AuCo$ alloy. A low first shell coordination number has been inferred, compared to bulk $Au$ and $Co$, and no significant signal, except for that from the first intermetallic atomic coordination, has been detected. These results are consistent with an amorphous-like or poorly nanocrystalline structure. The $AuCo$ alloy is the prevalent phase in all of the films even if the EXAFS analysis has also indicated the presence of segregated Co in the form of structurally disordered nanoparticles ($\sim\ 2\,nm$ in size [79]) dispersed within the alloyed AuCo matrix, in general agreement with it has been observed in similar samples [27]. The estimated volume fractions of the different phases are reported in table 3.2. Both the percentage of Co in the alloys and the fraction of segregated Co in the films increase with decreasing the Au:Co ratio. Figure 3.2(b) shows a typical in-plane view by transmission electron microscopy in bright-field (BF-TEM) for the $Au_1Co_2$ thin sample (analysis performed with a Field emission FEI TECNAI F20 Super Twin FEG (S) TEM). The BF-TEM contrast is quite

**Table 3.2:** *Column 1: labels of the samples. Columns 2 and 3: volume fractions of the AuCo alloy, with its stoichiometry, and of segregated $Co$ (to convert atomic fractions to volume fractions, elemental atomic weights and densities have been used)*

| Samples | Volume fractions | |
|---|---|---|
| | Alloy (vol %) | Co (vol %) |
| $Au_2Co_1$ | $Au_{80}Co_{20}$ 90 ± 7 | 10 ± 3 |
| $Au_1Co_1$ | $Au_{73}Co_{27}$ 75 ± 10 | 25 ± 5 |
| $Au_1Co_2$ | $Au_{57}Co_{43}$ 65 ± 9 | 35 ± 5 |

uniform with some black and white spots of a few nanometers in size; the BF-TEM contrast is dominated by mass-contrast with negligible contribution from diffraction contrast in agreement with the above mentioned poorly crystalline nature of the films evidenced by EXAFS analysis. Therefore, we can qualitatively interpret the BF-TEM image as arising from a nanocomposite films, made by some segregated $Au$-rich nanostructures (dark spots) and some $Co$-rich nanostructures (white spots), both embedded in a $AuCo$ alloy, which constitutes the dominant phase. It appears quite evident that AuCo alloy and segregated Co are substantially indistinguishable and the same conclusion holds for the other samples.

## 3.2 Magnetic results

The magnetic properties of the AuCo films have been studied in the $6\,K - 300\,K$ temperature range with the SQUID magnetometer (section 2.2) and, at $T = 300\,K$, with the MOKE apparatus (section 2.1). For the analyses, the sputtered samples have been cleaved according to the crystallographic orientation of the substrate, so to obtain pieces of $(5 \times 5)\,mm^2$. The SQUID hysteresis loops have been corrected for the diamagnetic contributions of the $Si$ substrate and $SiO_2$ cap layer; in addition, to facilitate the comparison, they are shown normalized to the saturation magnetization ($M_s$). $M_s$ has been determined as the ratio between the magnetic moment and the magnetic film volume.

Table 3.3 reports the values of $M_s$ for the AuCo samples, measured at temperature $T = 6K$ and $T = 300\,K$ in $H = 50\,kOe$. In the reference Co film, $M_s = (1250 \pm 60\,emu/cm^3)$ at $T = 6\,K$ and, within the experimental error, it does not depend appreciably on temperature in the investigated $T$ range; it is substantially lower than the value expected for bulk hcp Co ($1446\,emu/cm^3$ at $T = 0\,K$ [81]) and its reduction may be ascribed to the nanocrystalline structure of the film, implying the presence of a large fraction of atoms located at the grain boundaries and, hence, a reduced atomic density [82, 83, 84]. However, this value is in general agreement with other results on thin Co films [85]. $M_s$ increases with increasing the $Co$ content in the films. One can easly realize that the saturation magnetization values are higher than the magnetization contributions provided by the $Co$ particles (the $M_s$ value of the reference $Co$ film has been attributed to the segregated cobalt for this calculation). Hence, in all the samples, the $AuCo$ alloy has a net magnetization, namely is ferromagnetic. Based on the volume fractions in table 3.2, calculated values of saturation magnetization for the $AuCo$ alloy at $T = 6\,K$ are $\sim 230\,emu\,/\,cm^3$ for $Au_2Co_1$, $\sim 280\,emu\,/\,cm^3$ for $Au_1Co_1$, and $\sim 500\,emu\,/\,cm^3$ for $Au_1Co_2$ (the relative error associated to these values ranges between $20\,\%$ and $35\,\%$).

**Table 3.3:** *Column 1: labels of the samples. Column 2: saturation magnetization ($M_s$) measured at $T = 6\,K$ in $H = 50\,kOe$. Column 3: $M_s$ at $T = 300\,K$. The main error source is the uncertainty of the sample thickness.*

| Sample | $M_s$ at $T = 6\,K$ $(emu/cm^3)$ | $M_s$ at $T = 300\,K$ $(emu/cm^3)$ |
|---|---|---|
| $Au_2Co_1$ | 325 ± 22 | 232 ± 15 |
| $Au_1Co_1$ | 523 ± 20 | 480 ± 18 |
| $Au_1Co_2$ | 755 ± 28 | 733 ± 27 |

### 3.2.1 Measured hysteretic behavior

Information on the magnetic properties of the samples and on their magnetic structure has been gained by the analyses of the hysteresis loops.

First, let us consider the sample $Au_1Co_2$. Figure 3.3 show the loops measured at $T = 20\,K$ along two in-plane orthogonal directions corresponding to the sides of the sample. Along one direction, the loop appears highly squared, with the ratio between the remanet magnetization and saturation magnetization $M_r/M_s = 0.97$; the loop measured in the orthogonal direction has a lozenge shape with a smaller squareness ratio, $M_r/M_s \sim 0.41$ and shows a very peculiar feature, namely the crossing of the two branches (3.3).

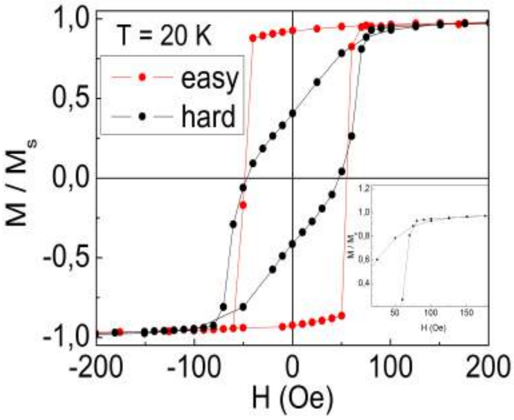

**Figure 3.3:** *In-plane hysteresis loops measured on sample $Au_1Co_2$ at $T = 20\,K$ along the easy (red) and hard (black) orthogonal axes. Inset of frame: enlarged view of the hard axis loop.*

A similar magnetic behavior is observed at higher temperature, up to $T = 300\,K$. Figures 3.4(a) and 3.4(b) show the hysteresis loops at $T = 100\,K$ and $T = 300\,K$, respectively.

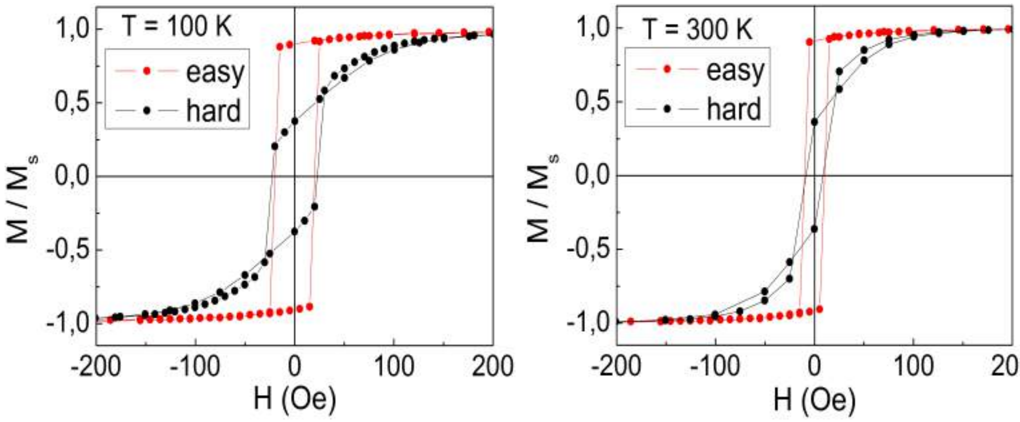

(a) (b)

**Figure 3.4:** *In-plane hysteresis loops measured on sample $Au_1Co_2$ along the easy (red) and hard (black) orthogonal axes at $T = 100\,K$ (a) and $T = 300\,K$ (b), respectively*

In addition, the curves of $H_c$ and $M_r/M_s$ vs. T, measured along the easy and hard axes, are shown in figures 3.5(a) and 3.5(b).

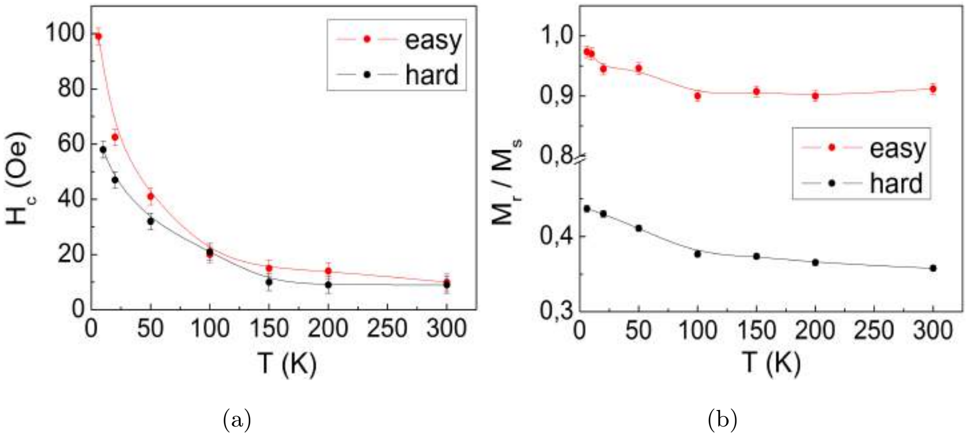

(a) (b)

**Figure 3.5:** *(a) Coercivity $H_c$ and (b) squarness ratio $M_r$ / $M_s$ vs. $T$ measured on sample $Au_1Co_2$ along the easy (red) and hard (black) orthogonal axes. In some cases, the error bar is smaller or comparable to the symbol size. Solid lines are guides to the eye.*

Hence, the magnetic behavior is clearly anisotropic and the direction corresponding to the high-remanence loop is a preferential magnetization axis, that we will indicate as the easy axis; accordingly, the orthogonal direction is indicated as the hard axis. To elucidate this last point, we have carried out measurements by MOKE ($T = 300\,K$), which have confirmed that the loops with higher and lower remanence are those measured along the sides of the sample. The squarness ratio as a function of the angle is shown in figure 3.6.

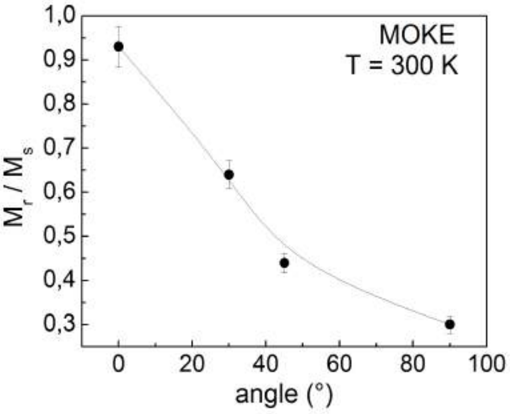

**Figure 3.6:** *Squarness ratio ($M_r$ /$M_s$) as a function of the angle (direction $0°$ is along one side of the squared sample) for sample $Au_1Co_2$.*

Sample $Au_1Co_1$ exhibits a similar magnetic behavior. Figures 3.7(a) and 3.7(b) show typical hysteresis loops, measured along two orthogonal directions, at $T = 50\,K$, $T = 100\,K$ and $T = 300\,K$, respectively.

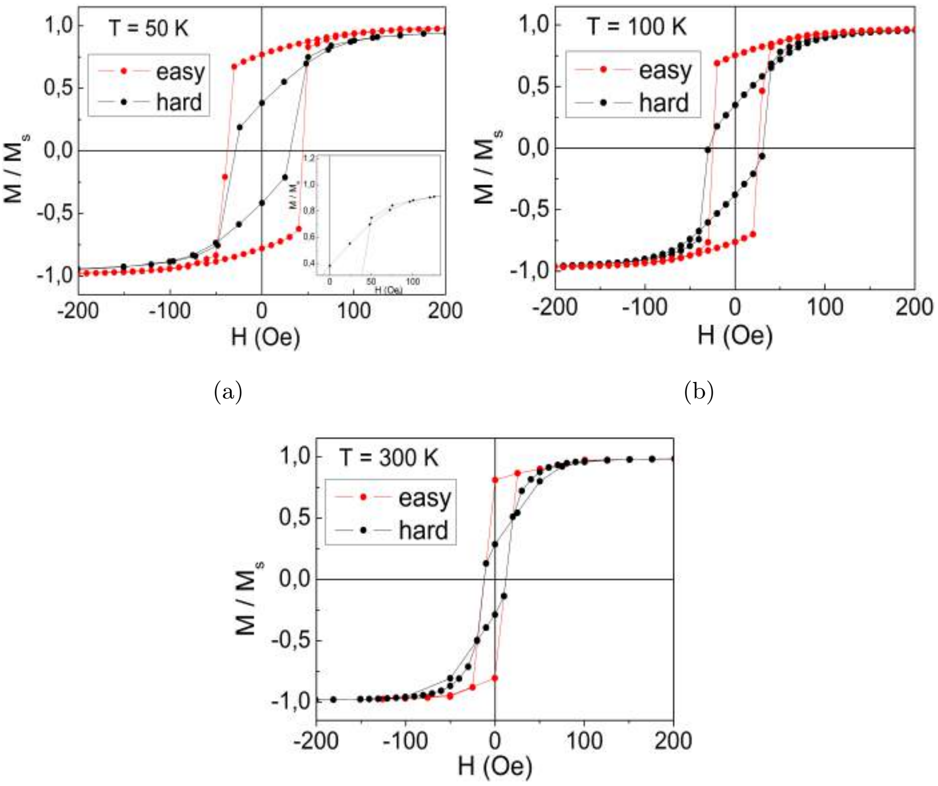

(a)

(b)

(c)

**Figure 3.7:** *In-plane hysteresis loops measured on sample $Au_1Co_1$ along the easy (red) and hard (black) orthogonal axes at $T = 50\,K$ (a) $T = 100\,K$ (b) and $T = 300\,K$ (c). Inset of frame (a): enlarged view of the hard axis loop.*

$H_c$ and $M_r\,/\,M_s$ vs. $T$ are displayed in figures 3.8(a) and 3.8(b).

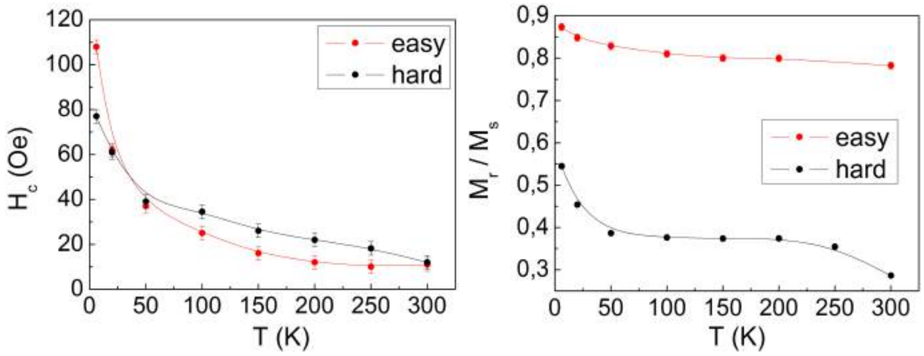

(a)

(b)

**Figure 3.8:** *(a) Coercivity $H_c$ and (b) squarness ratio $M_r\,/\,M_s$ vs. $T$ measured on sample $Au_1Co_1$ along the easy (red) and hard (black) orthogonal axes. In some cases, the error bar is smaller or comparable to the symbol size. Solid lines are guides to the eye.*

It is possible to distinguish an easy magnetization axis, corrisponding to the direction along which the high-remanence loops are measured (squareness values slightly lower than in $Au_1Co_2$ are found at all temperatures, actually), and an hard one, corrisponding to the direction along which the low-remanence loops are measured. It is evident, also in this case, the appearance of the branch-crossing effect along the hard magnetization axis (3.7(a) and 3.7(b)). In this sample too, MOKE measurements are performed to confirm that the loops with higher and lower remanence were those measured along the sides of the samples (figure 3.9).

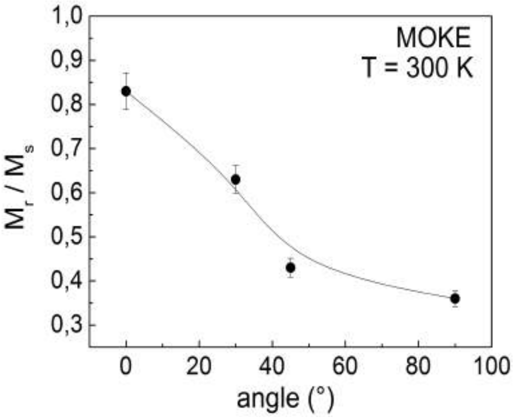

**Figure 3.9:** *Squarness ratio ($M_r$ /$M_s$) as a function of the angle (direction $0°$ is along one side of the squared film) for sample $Au_1Co_1$.*

Passing to the sample richer in Au, the loops measured at 0° and 90° are shown in figure 3.10(a). The sample appears isotropic in the plane, but it turns to anisotropic with rising temperature. A hysteretic behavior, similar to those found in $Au_1Co_2$ and $Au_1Co_1$ is observed (figure 3.10(b)), which persists at higher temperature.

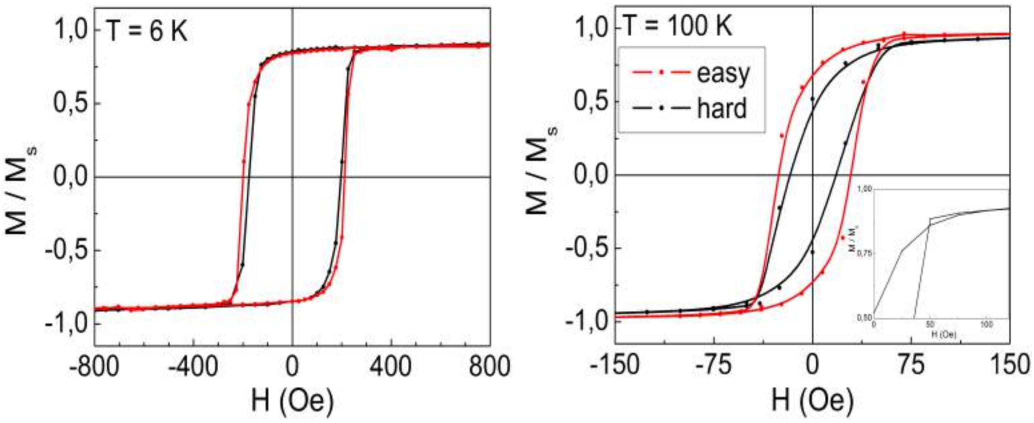

(a) (b)

**Figure 3.10:** *In-plane hysteresis loops measured on sample $Au_2Co_1$ along the easy (red) and hard (black) orthogonal axes at $T = 6\,K$ (a) and $T = 100\,K$ (b). Inset of frame (b): enlarged view of the hard axis loop.*

$H_c$ and $M_r\,/\,M_s$ vs. $T$ are shown in figure 3.11(a) and 3.11(b), respectively.

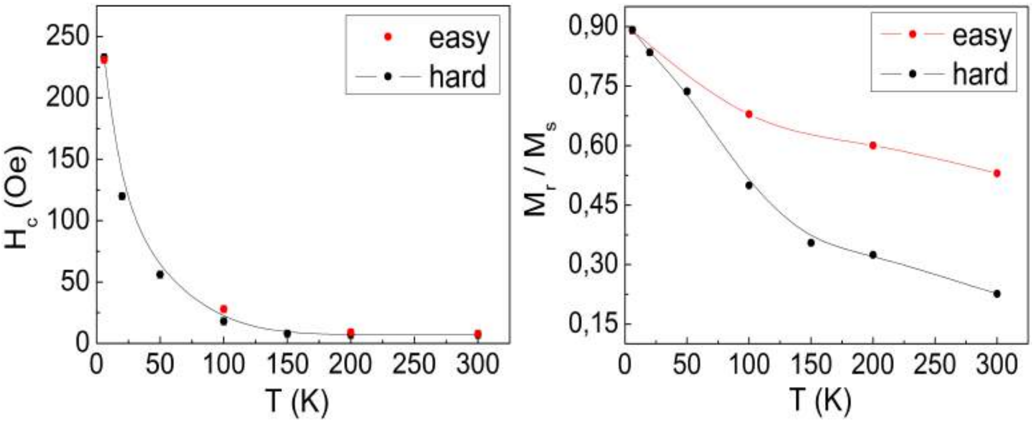

(a) (b)

**Figure 3.11:** *(a) Coercivity $H_c$ and (b) squarness ratio $M_r\,/\,M_s$ vs. $T$ measured on sample $Au_2Co_1$ along the easy (red) and hard (black) orthogonal axes. In some cases, the error bar is smaller or comparable to the symbol size. Solid lines are guides to the eye.*

At the lowest temperature, $H_c$ is higher than in the other investigated samples and it strongly decreases with increasing temperature especially up to $\sim\,100\,K$ (there is only a small difference in $H_c$ along the easy and hard magnetization directions); the squarness ratio exhibits a similar decreasing trend (the values measured along the easy axis are obviously larger than those measured in the hard direction). Hence, the magnetic behavior of sample $Au_2Co_1$ is somewhat different compared to the other films and, in this respect, a remarkable difference is also a clear non saturation tendency of the loops, which becomes more pronounced with increasing temperature (hence, for this sample, the values of $M_s$ in Table 3.3, taken as those measured in $H = 50\,kOe$, may be slightly underestimated; in any case, the saturation magnetization value is expected to lie within the indicated error band). This effect is well visible in figure 3.12 showing the first quadrant of the loop at $T = 300\,K$ (at high field, the trend of $M$ vs. $H$ does not visibly depend on the measurement direction). It should also be noted that a reduction of $M_s$ of $\sim 30\,\%$ is experienced with increasing the temperature from $6\,K$ to $300\,K$, whilst it is not larger than 8% in other samples ( table 3.3).

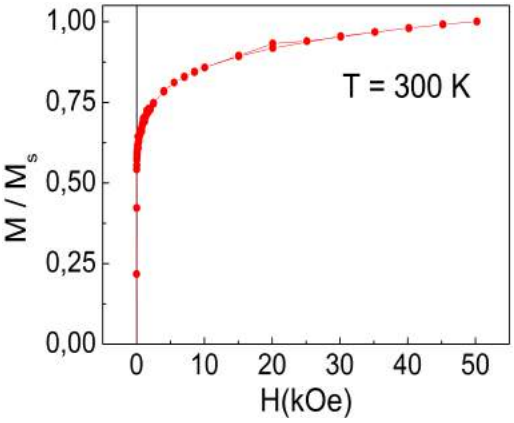

**Figure 3.12:** *First quadrant of the loop measured on* $Au_2Co_1$ *at* $T = 300\,K$*.*

In order to better elucidate the behavior of sample $Au_2Co_1$, the magnetization $M$ has been measured for increasing temperature in the $6\,K$ - $300\,K$ range in $H_{appl} = 20\,Oe$, after cooling the sample from room temperature down to $6\,K$ both without external field (zero-field-cooling, ZFC) and in $H_{appl}$ (field-cooling, FC). The result is shown in figure 3.13(a). Magnetic irreversibility, i.e. difference between FC and ZFC magnetization, is clearly visible from $T = 6\,K$ to $T \sim 215\,K$, where the ZFC displays a peak. Some features are noteworthy: the value of $M_{FC}$ at $T = 6\,K$ corresponds to $\sim 70\,\%$ of the total measured $M_s$ ($\sim 325\,emu\,/\,cm^3$, see table 3.3) in agreement with the presence of a large fraction of ferromagnetically soft phase; moreover, in the whole temperature range, the FC branch exhibits a downward concavity, consistent with the existence of a monotonically decreasing ferromagnetic background.

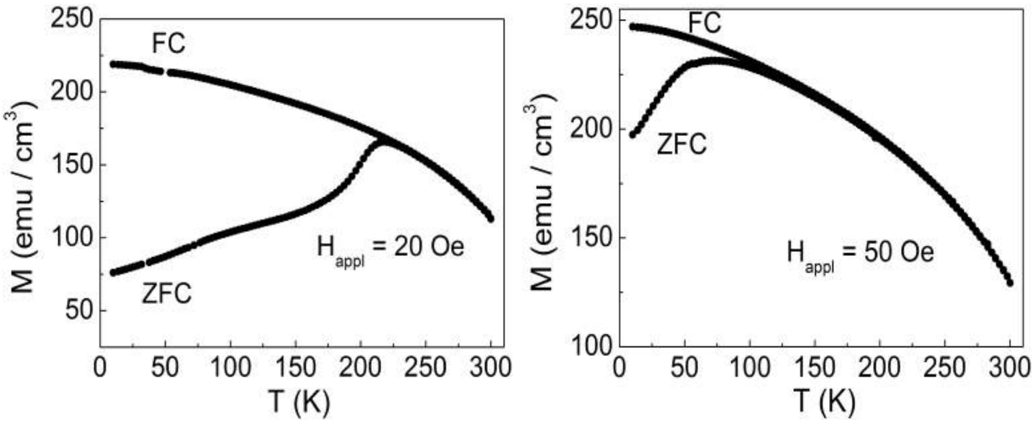

(a) (b)

**Figure 3.13:** *Zero-field-cooling (ZFC) and field-cooling (FC) magnetization as a function of temperature measured on sample $Au_2Co_1$ in applied magnetic field $H_{appl} = 20\,Oe$ (a) and $H_{appl} = 50\,Oe$ (b).*

A similar ZFC-FC magnetization measurement in $H_{appl} = 50\,Oe$ is shown in figure 3.13(b). Compared to the previous case, with increasing $H_{appl}$ the ZFC peak appears at lower temperature, as expected for an assembly of nanoparticles undergoing magnetic relaxation [86]; for $T > 100\,K$ the ZFC and FC branches are superposed and show a monotonous decreasing trend.

The obtained experimental results, namely the observed anisotropic magnetic behavior, despite the deposition procedure which favors an uniform coverage of the substrate, and the branch-crossing effect could be hints of the coexistance of two magnetic interacting phases. Structural results point out the attention on the existance of two phases: a $AuCo$ alloy in which $Co$ particles are embedded in. In this class of samples, the magnetic exchange coupling of the Co particles with the surrounding matrix is expected to result in an increase of their effective magnetic size, with respect to their structural size (3.1). Moreover, since the fraction of Co particles in the films increases with decreasing the $Au : Co$ ratio (table 3.2) and their interdistance reduces and possibly vanishes, the exchange interaction may be transmitted to neighboring particles through the ferromagnetic matrix, leading to the formation of magnetically coupled clusters, namely aggregates of Co particles.

In $Au_2Co_1$ the segregated cobalt is just a small fraction ($\sim$ 10 vol %, see table 3.2) and the AuCo alloy has a weaker ferromagnetism compared to the matrix in the other films, being richer in Au. Hence, we hypothesize a weaker magnetic coupling between the Co particles and the AuCo matrix and between neighboring Co particles in this film, compared to $Au_1Co_2$ and $Au_1Co_1$, which results in Co clusters with smaller magnetic size. This can account for the larger $H_c$ of $Au_2Co_1$ at $T = 6\,K$ ($\sim 235\,Oe$), compared to the other films.

With increasing temperature, the strong thermal dependence of $M_s$ and the marked non-saturation tendency of the hysteresis loop (figure 3.12) suggest that the smallest Co clusters undergo a magnetic relaxation process, similar to superparamagnetism [86]. In addition, the magnetic irreversibility effect, clearly observed through ZFC-FC measurements (figures 3.13(a) and 3.13(b)), confirms our hypothesis of magnetically relaxing Co clusters [86, 87]. Accordingly, $H_c$ reduces strongly with increasing temperature, especially in the $6\,K - 100\,K$ range ($H_c \sim 20\,Oe$ at $T = 100\,K$, see figure 3.10(b)). A similar, even if less marked, decrease of $H_c$ at low temperature is also visible in $Au_1Co_2$ and $Au_1Co_1$ (figures 3.5(a), 3.8(a)). Hence, we cannot completely exclude the possibility that a very small fraction of relaxing Co clusters also exists in these two samples, even if the coercivity trend would be the only appreciable hint of this. Moreover, it is interesting to note that similar values of $H_c$ are measured in the three samples for $T \geq 100\,K$. This suggests that, above this temperature, the magnetic behavior of $Au_2Co_1$ is also ruled by the AuCo matrix and by the fraction of the non-relaxing Co clusters and, for this reason, hysteretic properties emerge similar to those observed in the other samples.

### 3.2.2 Micromagnetic simulations and interpretation

In the previous subsection, I have reported about a particular hysteretic behavior observed in the samples $Au_1Co_2$, $Au_1Co_1$ and, above $T \sim 100\,K$, in $Au_2Co_1$, featuring anisotropy and crossed branches of the hard-axis loops. As for this last phenomenon, it could be partially related to an unusual behavior of negative remanent magnetization (NMR), also known as negative coercivity or inverted hysteresis loop. In a usual situation, the magnetization along the $x$-axis, for example, is positive (negative) when the strength of an applied magnetic field is reduced to zero from the saturation field in the $+x$ ($-x$) direction. This common behavior of positive remanent magnetization occurs because the magnetizations at the remanent state are relaxed to the easy axes with $\mathbf{M}$ pointing to the same direction of $\mathbf{H}$. In the case of NMR, the magnetizations at the remanent state also reside at the easy axes, but the majority of $\mathbf{M}$ points to the opposite direction of $\mathbf{H}$ [88]. This phenomenon, which was first observed in amorphous *GdCo* films [89], is found in numerous magnetic structures as, for example, systems consisting of two magnetic phases that are coupled antiferromagnetically and have different magnetizations and anisotropy strengths [90, 91, 92, 93]; even if it is also observed in ferromagnetically coupled bilayers, each layer of them possesses a uniaxial anisotropy [94]. In addition, this phenomenon appears in trench patterned ferromagnetic permalloy ($Py$, $Ni_{80}Fe_{20}$) thin films, demonstrating as the superficial patterning can significantly modify the magnetic response of a material [95]. A completely different system showing NMR consists of particles over a wide size range deposited on non-magnetic matrix [96, 97, 98, 99].

In our case, we have ascribed the observed hysteretic behavior to the coexistance of two different magnetic phases, that we have identified with the $AuCo$ matrix and the $Co$ clusters [100]. The two phases are intimately mixed and the magnetization process is expected to be governed by the subtle interplay between the strength and directions of their magnetic anisotropy, strength of the exchange interaction, and the external applied magnetic field. Since most of these parameters cannot be experimentally determined and because of the inherent complexity of the system, to achieve a full comprehension of the magnetization process in the investigated sample is a quite difficult task. We have obtained valuable informations by considering a simpifield model of a ferromagnetic two-phase system and performing micromagnetic calculations using the three-dimensional Object Oriented MicroMagnetic Framework (OOMMF) software. The program applies the Landau Lifshitz Gilbert (LLG) equation to simulate the spin configuration and to compute the energy and magnetization of nanostructures [101]. It is a finite difference code which requires discretization of a chosen geometry over a grid of identical prism-cells in which the magnetization is supposed to be uniform. LLG equation is :

$$\frac{d\mathbf{M}}{dt} = -\gamma \mathbf{M} \times \mathbf{H}_{eff} - \frac{\gamma\alpha}{M_s}\mathbf{M} \times (\mathbf{M} \times \mathbf{H}_{eff}) \tag{3.1}$$

where $\mathbf{M}$ is the pointwise magnetization, $H_{eff}$ is the pointwise effective field defined as the energy ($E$) first derivative $\mathbf{H}_{eff} = \mu_o^{-1}\frac{\partial E}{\partial \mathbf{M}}$, $\gamma$ the gyromagnetic ratio and $\alpha$ the damping coefficient.

To simulate the studied system, we have considered the geometry shown in figure 3.14: a squared element hosting an equilateral cylinder at the center, both discretized using cells with a basis of $(1.25 \times 1.25)\,nm^2$ and height of $10\,nm$. In particular, the squared element consists of $14 \times 14$ cells and, hence, its area is $306.25\,nm^2$ in the $x - y$ plane and the thickness along the $z$ direction is $10\,nm$. The central cylinder is also $10\,nm$-thick and occupies a volume corresponding to $26.5\,\%$.

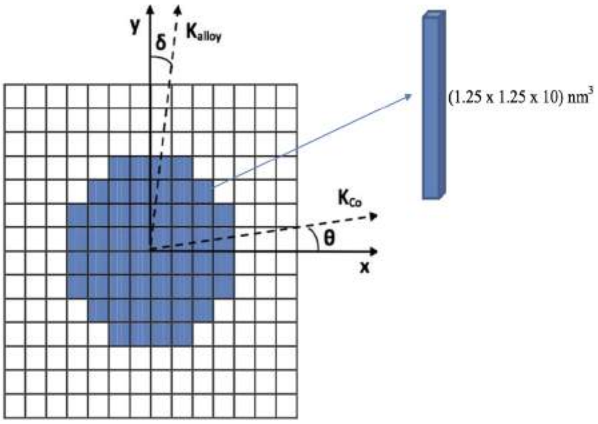

**Figure 3.14:** *Simplified scheme of the system simulated in the micromagnetic analysis. The squared element represents the* $AuCo$ *matrix and the central cylinder represents a* $Co$ *cluster. In this geometry, the volume fraction occupied by the* $Co$ *cluster is* $26.5\,\%$*. The dotted lines are the anisptropy directions for the two phases: the Co anisotropy (*$K_{Co}$*) forms an angle* $\theta$ *with the* $x$ *axis and the* $AuCo$ *anisotropy (*$K_{alloy}$*) forms an angle* $\delta$ *with the* $y$ *axis. See text for further details.*

The simulations have been carried out using a $2D$ periodic boundary conditions, which means that the geometry in figure 3.14 is periodically replicated in the whole $x-y$ plane so as to simulate an infinite film. Hence, the central element represents a $Co$ cluster (i.e., an aggregate of smaller $Co$ particles) of $10\,nm$ in size and the squared one represents the portion of surrounding $AuCo$ matrix. The precise definition of such a system has been dictated by a number of concomitant factors. The $Co$ cluster shape is cylindrical and the diameter is equal to the height in order to increase the symmetry of the structure preventing, at the same time, shape anisotropy effects and keeping the computational time under control; the choice of the $10\,nm$ size is strictly intertwined to the dimension of the prism-cells. In fact, to avoid the occurrence of fictitious effects, the side of the cells has been set so as to fulfill two main requirements: 1) to smooth the jagged perimeter of the cylinder and 2) to manage an even number of cells, preventing any artificial symmetry-breaking in the simulations. Moreover, we demand that the relative volume fractions of the cylindrical and squared elements approximately correspond to the volume fractions of the $Co$ and $AuCo$ phases in $Au_1Co_1$ (table 3.2).

Coherently with the data for $Au_1Co_1$ reported in 3.2.1, we have assigned saturation magnetization values $M_{s\_alloy} = 280\,emu\,/\,cm^3$ to the $AuCo$ matrix and $M_{s\_Co} = 1250\,emu\,/\,cm^3$ to the $Co$ cluster. The magnetic exchange stiffness for $Co$ is $A_{Co} = 3\,\mu erg\,/\,cm^3$, corresponding to the literature value (provided by the

OOMMF database [101]), whilst $A_{alloy}$ has been arbitrarily set to a value one order of magnitude smaller ($A_{alloy} = 0.2\,\mu erg\,/\,cm^3$) to take the $Co$ dilution in the alloyed phase into account [102]. With this choice of $A_{alloy}$ the ferromagnetic exchange length of the $AuCo$ phase, $L_{alloy}$, is shorter than the $Co$ clusters' interdistance [103], so to avoid the cluster-cluster interaction. The stiffness of the exchange interaction between the two phases has been set to $1.6\,\mu erg\,/\,cm^3$, i.e., an intermediate between $A_{Co}$ and $A_{alloy}$. The anisotropy coefficients are $K_{Co} = 5 \times 10^6\,erg\,/\,cm^3$ for the Co element, corresponding to the literature value [40], and $K_{alloy} = 2.4 \times 10^6\,erg\,/\,cm^3$ for the $AuCo$ alloy, about half of the former ($K_{alloy} \setminus K_{Co} \sim 0.48$). The anisotropy axes of both phases lie in the $x - y$ plane as schematized in figure 3.14: the $Co$ anisotropy direction is defined by the angle $\theta$ it forms with the x-axis whilst the $AuCo$ anisotropy direction is defined by the angle $\delta$ it forms with the y-axis.

The hysteresis loops have been obtained by calculating the equilibrium spin configuration for each value of the external field applied along the $x$ and $y$ axes through the LLG equation. The simulated cycles will be shown as normalized, in ordinate, to the saturation magnetization and, in abscissa, to the anisotropy field of the matrix $H_K = \frac{2K_{alloy}}{M_{s\_alloy}}$.

In a first set of simulations, the value of $\delta$ has been kept fixed to 0° (namely, the $AuCo$ anisotropy direction is along y) and $\theta$ has been varied between 0° and 90°. Selected results are shown in figure 3.15: for each $\theta$, the loops measured along y (red line) and along x (black line) are displayed. At all $\theta$ values an anisotropic hysteretic behavior is observed and the high-remanence loop is measured along the y axis, namely along the anisotropy direction of the $AuCo$ matrix. Hence, we indicate the y axis as the easy magnetization axis of the system. For $\theta \neq 90°$, non-zero remanence is measured along the hard magnetization direction, i.e., along x. For $\theta = 90°$, namely when $K_{alloy}$ and $K_{Co}$ are parallel, the loop measured along y is perfectly squared whereas no hysteresis is observed in the x direction (figure 3.15(f)). This behavior is very close to that modeled by Stoner and Wohlfarth for a single-domain magnetic element with uniaxial anisotropy [104]. A remarkable outcome is that for small $\theta$ values, the loops measured along x show a crossing of the branches. The effect is well visible in figure 3.15 for $\theta = 5°$, 15°, and 20° (the best similarity with the experimental results is obtained for the smallest $\theta$, actually) No crossing is observed at higher $\theta$ (in figure 3.15(e), the result for $\theta = 25°$ is displayed). Hence, the main features of the hysteretic behavior of the $AuCo$ films are qualitatively well reproduced in our model by imposing $\delta = 0°$ and $0° < \theta < 25°$. The same results are obtained for negative values of $\theta$, i.e imposing a negative slope to the $K_{Co}$ axis.

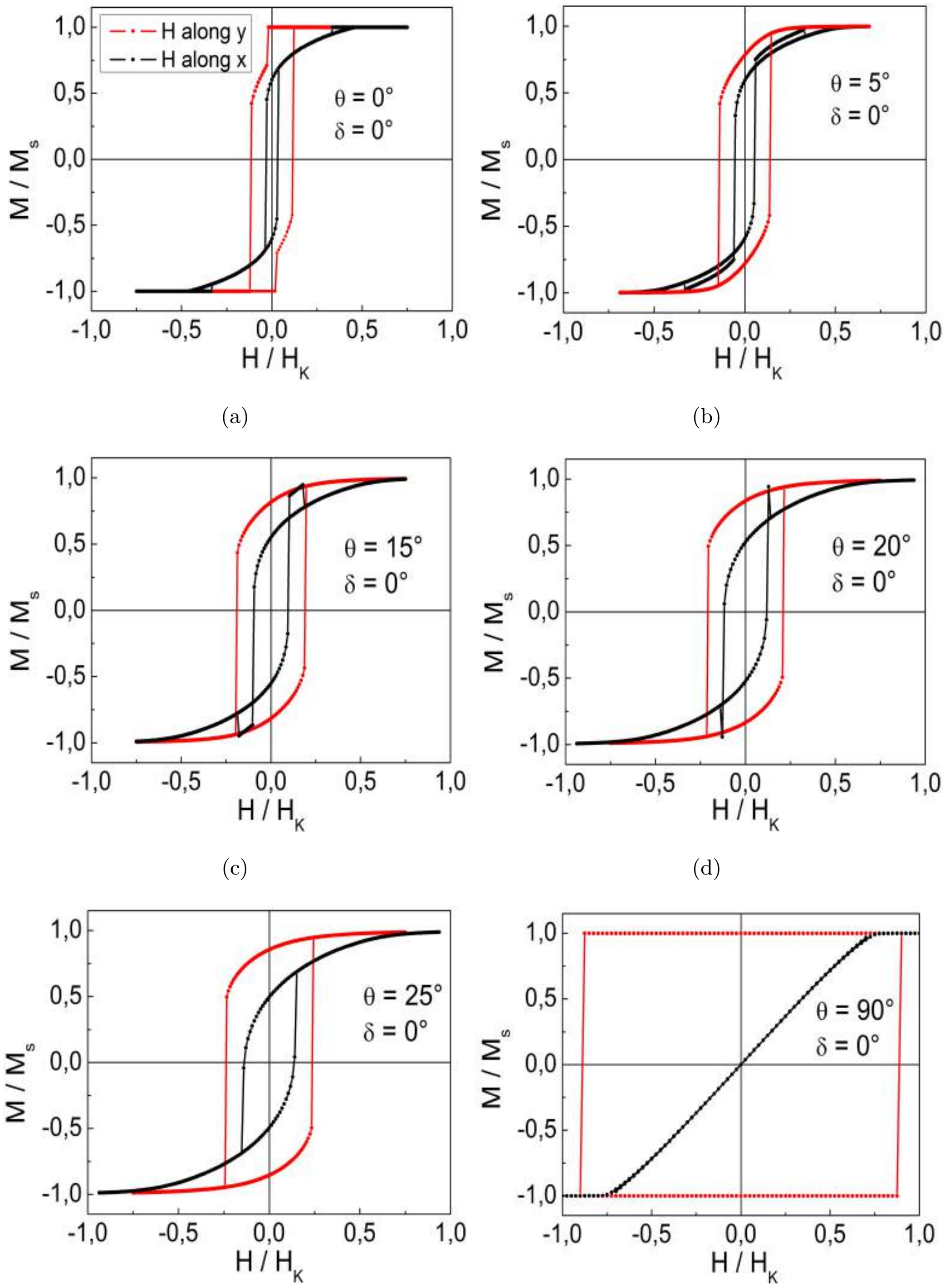

(a) (b) (c) (d) (e) (f)

**Figure 3.15:** *Simulated hysteresis loops obtained for the indicated values of* $\theta$ *and keeping* $\delta$ *fixed (*$\delta = 0°$*), with magnetic field* $H$ *along y axis (red) and the x axis (black). In this figure and in the following ones,* $H$ *values are normalized to the anisotropy field* $H_K$ *of the* $AuCo$ *matrix.*

.

To gain a deeper insight into the hysteresis process affected by branch-crossing effect, let us examine in more detail the simulated loop obtained for $\delta = 0°$, $\theta = 5°$ and magnetic field applied along x, already shown in figure 3.15($b$). Each point of the hysteresis loop corresponds to a specific configuration of the magnetization (magnetization map) of the system, modeled by the grid of cells in figure 3.14. In figure 3.16, the simulated loop is displayed (central frame) togheter with eight magnetization maps relative to the points indicated on the loop itself. The arrow, visible in each cell of the maps, indicates the orientation of the magnetic moment of the cell itself (as already explained above, the magnetization is supposed to be uniform in each cell). Therefore, the grid of arrows provide us with the informations about the current magnetization state; the magnetization is effectively defined by a vector field. The color of each cell provides information about the projection of the magnetization along x ($M_x$), namely in the direction of the applied magnetic field: blue and red designate the sign of $M_x$ (positive or negative, respectively) and the color intensity is proportional to the magnitude of $\mid M_x \mid$.

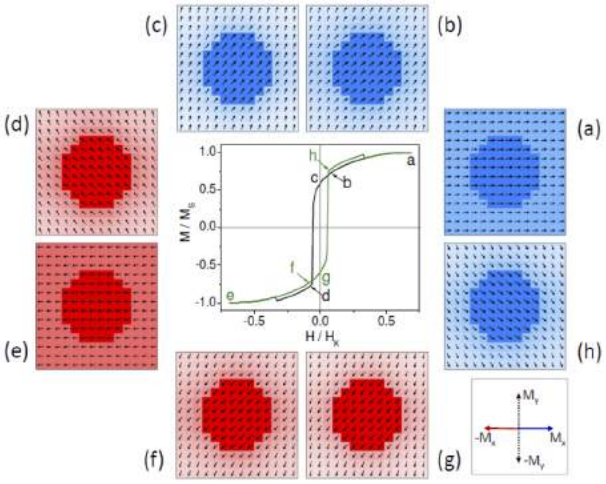

**Figure 3.16:** *Central frame: hysteresis loop calculated for* $\delta = 0°$, $\theta = 5°$ *and* $H$ *applied along the x axis (already shown in figure 3.15(b)); the descending branch (from positive to negative saturation) is the black line, whilst the ascending branch (from negative to positive saturation) is the green line (in the regions where the two branches are superposed, only the green line is visible). The magnetization maps corresponding to the indicated points of the loop are shown: they are labelled with letters from* $(a)$ *to* $(h)$*. The key frame on the bottom-left corner indicates that the blue and red colors in the maps designate the sign of the projection of the magnetization along the x axis,* $M_x$ *(positive and negative, respectively); no specific color is assigned to the magnetization projection along the y axis,* $M_y$*. See the text for further explanation.*

To mimic the experimental loop measurement procedure, our calculation of the simulated loop starts from the positive magnetic saturation state, namely from map ($a$) (different shades of blue characterize the matrix and the $Co$ cluster because of the different values of $M_{s\_Co}$ and $M_{s\_alloy}$). With decreasing the applied field, i.e., moving to point ($b$) and then to the positive remanence state ($c$), the interplay between the matrix-cluster exchange coupling and the anisotropies' strengths and directions — the misalignment $\theta$ of $K_{Co}$ plays a particularly crucial role — favors an upward orientation of the magnetization arrows in the cells. This means that the projection of the magnetization along $y$ ($M_y$) is positive. At point $d$, the negative field, applied along $x$, has been sufficient to reverse the largest fraction of the magnetization of the system. Hence, $M_x < 0$, whereas $M_y$ is still positive, even in the $Co$ cluster. In fact, the exchange coupling with the matrix dominates on $K_{Co}$ that here is forcing the $Co$ magnetization downward, because of the misalignment $\theta$. With further decreasing the field, a magnetic configuration settles on with arrows pointing downward, which results in $M_y < 0$ (this map is not shown, but the configuration is qualitatively similar to that visible also in frame $f$, along the ascending branch of the loop). A sudden jump in $M/M_s$ marks this passage from $M_y > 0$ to $M_y < 0$. Then a negative saturation is achieved at point ($e$), where $M_y = 0$. Point ($e$) marks the end of the descending branch of the loop (from positive to negative saturation). On the descending branch of the loop (from negative to positive saturation), point ($f$) is analogous to point ($b$). In this case, $K_{Co}$ and the matrix-cluster exchange coupling cooperate to produce a downward orientation of the magnetization arrows (i.e., $M_x < 0$ and $M_y < 0$). Point ($g$) is the negative remanence state. In point ($h$), analogous to ($d$), $M_x > 0$ and $M_y < 0$. Points ($d$) and ($f$) correspond to the same negative value of the applied magnetic field. The comparison of the corresponding maps reveals that the slope of the magnetization arrows with respect to the x axis, especially those of the Co cluster, is larger in map ($f$) than in map $d$. As a consequence, $\mid M_x \mid$ calculated in ($f$) is smaller than in ($d$). Similarly, points ($b$) and ($h$) correspond to the same positive field. The slope of the arrows in ($b$) is larger than in ($h$) and, hence, $M_x$ in ($b$) is smaller than in ($h$).

The following general behavior emerges from the analysis of the maps: at any field within the range where the branch-crossing effect occurs in the third (first) quadrant of the loop, the slope of the $Co$ magnetization and the slope of $K_{Co}$ have the opposite sign along the descending (ascending) branch and have the same sign along the ascending (descending) one.

Then, we have studied the case of $\theta = 0°$ and variable $\delta$. The results are shown in figure 3.17: for $\delta = 5°$ (3.17(a)), the loop with higher remanence is measured along $y$ and crossed branches are found in the loop along $x$; for $\delta = 15°$ (3.17(b)) the highest remanence is measured in the $x$ direction (the loops have similar remanence, actually) and no branch-crossing is visible; as expected, for $\delta = 90°$ (3.17(c)), a Stoner-Wohlfarth behavior is produced, with easy magnetization direction along the $x$ axis.

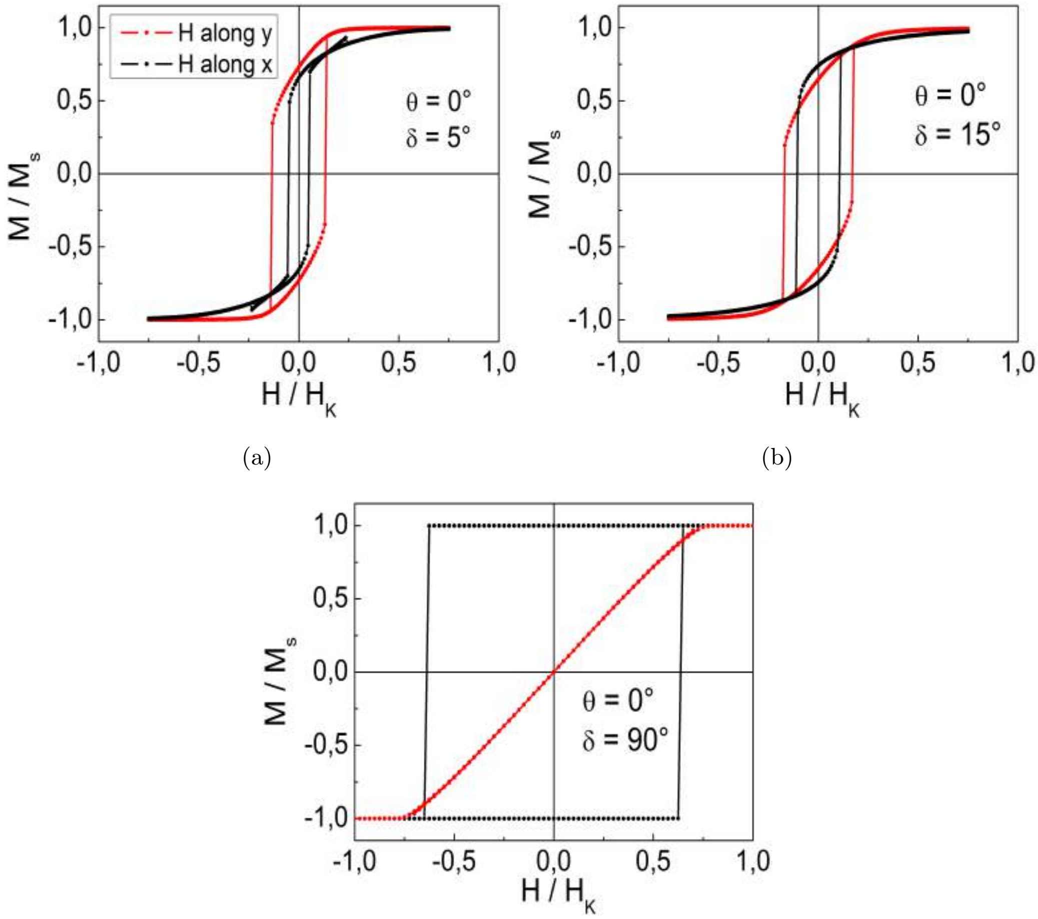

(a)

(b)

(c)

**Figure 3.17:** *Simulated hysteresis loops obtained for $\theta = 0°$ and for the indicated values of $\delta$, with magnetic field $H$ applied along the y axis (red) and the x axis (black).*

.

In figure 3.18 we show the simulations obtained for $\theta = 5°$ and $\delta = 5°$ (3.18(a)), $\delta = 10°$ (3.18(b)), $\delta = 20°$ (3.18(c)). Given the results for $\theta = 5°$ and $\delta = 0°$ (3.15(a)), the branch-crossing effect is seen to reduce with increasing the misalignment of $K_{alloy}$ with respect the $y$ axis and no effect is observed for $\delta = 20°$.

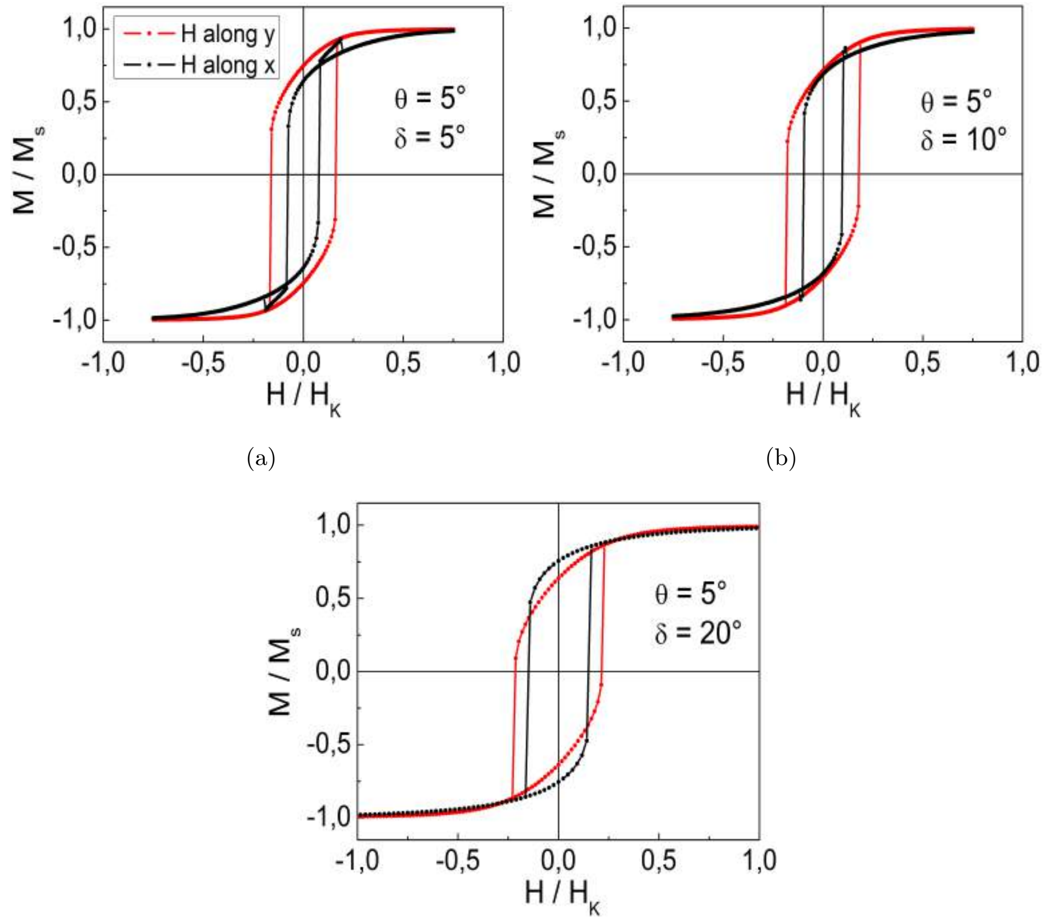

(a)

(b)

(c)

**Figure 3.18:** *Simulated hysteresis loops obtained for* $\theta = 5°$ *and for the indicated values of* $\delta$*, with magnetic field* $H$ *applied along the y axis (red) and the x axis (black).*

.

If we focus the attention on the simulations presenting the branch-crossing effect consider the ratio between the remanence measured along $y$ ($M_{ry}$) and that measured along $x$ ($M_{rx}$), we obtain: $M_{ry} \,/\, M_{rx} = 1.32$ for $\delta = 0°$ and $\theta = 5°$ (3.15(a)); $M_{ry} \,/\, M_{rx} = 1.11$ for $\delta = 5°$ and $\theta = 0°$ (3.17(a)); $M_{ry} \,/\, M_{rx} = 1.17$ for $\delta = 5°$ and $\theta = 5°$ (3.18(a)). Thus, the misalignment of $K_{alloy}$ is detrimental not only for the branch-crossing effect but also for the anisotropic character of the hysteretic behavior, since it tends to smooth the difference between easy and hard axes.

Based on the simulations for our micromagnetic two-phase system, key ingredients for observing anisotropic hysteretic behavior and branch-crossing effect are that the $AuCo$ has a well-defined anisotropy direction (the $y$ axis, in our reference frame in figure 3.14) and that the $Co$ clusters' anisotropy lies almost orthogonally to that of the matrix, i.e, it is just slightly misaligned with respect to the $x$ axis.

Now, the point is whether these requirements can be fulfilled in real samples. The possibility that the anisotropy ruling the magnetic behavior has a magnetocrystalline origin appears unlikely. In fact, the $AuCo$ alloy presents a poorly crystalline structure, which implies a distribution of locally varying easy axes, possibly resulting in a vanishingly small averaged anisotropy [105]. In this view, we are not able to account for the appearance of a net uniaxial magnetocrystalline anisotropy of the matrix. As for Co clusters, if the prevalent type of anisotropy was the magnetocrystalline one, they shoul possess a preferential crystallographic orientation in the plane of the film so that their anisotropy vectors would lie within a cone of limited angular width. In any case, the structural analyses exclude an in-plane texturing of the $Co$ phase [79]. We must consider a different scenario and we propose that both phases have dominant magnetoelastic anisotropy (see chapter 1). Cobalt is a magnetostrictive material [40] and the $AuCo$ alloy is likely to possess the same property [106]. It is well known that all films have a state of residual stress due to extrinsic factors (typically, the mismatch in the thermal expansion coefficients of both the film and the substarte) and to intrinsic factors (growth processes, grain structure, substitutional or interstitial impurities) [42, 16]; in the case of composite films, lattice and thermoelastic mismatch among the different phases must be also taken into account [107, 108]. Several of these factors may operate simultaneously so that the final stress distribution in the film results from their balance. Despite the fact that most of the models on the mechanical properties of film-substrate systems, such as the well-known Stoney theory [109], assume a spatial stress uniformity, a non-uniform stress distribution is much more likely to occur in practice [110] due, for instance, to a deviation between the ideal isotropic properties of the substrate and the real properties. A non-uniform stress distribution may be settled in our films, which implies that the average stress along two orthogonal directions may be different [16, 111, 112]. Although, at present, we are not able to unambiguously account for a non-uniform stress state in our sample, the observation that easy and hard magnetization axes are along the samples' sides suggests that the stress distribution originates from reproducible intervention of precise factors, presumably connected with the silicon substrate and/or with the production procedure of the samples. This item certainly deserves further attention also in the perspective of achieving a control of the stress state and thus governing the magnetoelastic anisotropy.

A small difference between the stress acting along $y$ and along $x$ on $AuCo$ ($\sigma_{y\_alloy}$

and $\sigma_{x\_alloy}$, respectively) and $Co$ ($\sigma_{y\_Co}$ and $\sigma_{x\_Co}$, respectively) is sufficient to generate the inherent anisotropic character that emerges in the hysteretic magnetic behavior, depending on the interplay between their strength and the sign of the magnetostrictive coefficients ($\lambda_S$). In this framework, two main pictures can be drawn. In the first one, the $Co$ and $AuCo$ alloy have magnetostriction constants of different signs. Since $Co$ has a negative $\lambda_S$ [40], a positive $\lambda_S$ is assigned to $AuCo$. We hypothesize that along the $y$ axis the two phases are subjected to a stress with the same — taken as positive to preserve the coherence with the coordinate system adopted in figure 3.14 — and that $\sigma_{y\_alloy} > \sigma_{x\_alloy}$ and $\sigma_{y\_Co} > \sigma_{x\_Co}$. In this way, the anisotropy axis of the $AuCo$ matrix is along the $y$ direction and the anisotropy of the $Co$ clusters preferentially lies along the $x$ direction. In the second picture, both $Co$ and $AuCo$ have negative $\lambda_S$. We assume that, along the $y$ axis, a negative stress acts on $AuCo$ and a positive one acts on $Co$ and that $\mid \sigma_{y\_alloy} \mid > \mid \sigma_{x\_alloy} \mid$ and $\sigma_{y\_Co} > \sigma_{x\_Co}$. In this way too, the anisotropy directions for the $AuCo$ matrix and for the $Co$ clusters are along $y$ and $x$, respectively. Taking the micromagnetic results into account, the required small misalignment of $K_{Co}$ with respect to the $x$ axis, may be accounted for in terms of the competition between the dominant magnetoelastic anisotropy and the magnetocrystalline one, presumed to act on the $Co$ clusters along random directions.

Hence, by assuming that the anisotropy of $AuCo$ and $Co$ has a prevalent magnetoelastic character, different situations can be envisaged, which fulfill the requirements indicated by the micromagnetic study. By the light of this statement, our initial choice of setting $K_{Co}$ to the magnetocrystalline anisotropy of bulk cobalt may appear not appropriate (also in consideration of the poor crystallinity of the Co phase in real samples) and also the choice of $K_{alloy}$ has been arbitrary. Calculations carried out using different values of $K_{Co}$ and $K_{alloy}$, but in same relationship, produce similar results, indicated that the outcomes do not strictly depend on the assigned anisotropy coefficients. As an example, figure 3.19 shows the hysteresis loops calculated for $\theta = 5°$ and $\delta = 0°$, as in figure 3.15(b), and imposing $K_{alloy} = 0.66 \times 10^6 \, erg\,/\,cm^3$ (namely, about an order of magnitude less with respect to the value settled for the previous simulations) and $K_{Co} = 1.38 \times 10^6 \, erg\,/\,cm^3$ ($K_{alloy} \setminus K_{Co} \sim 0.48$).

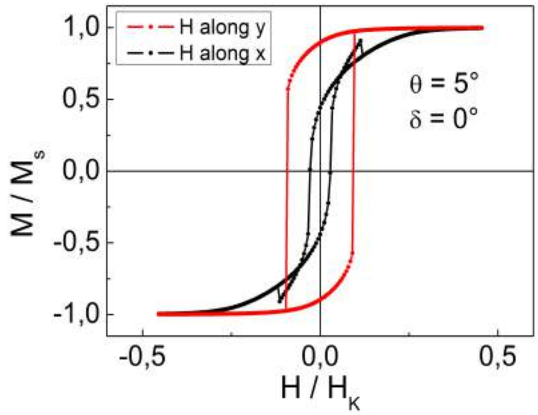

**Figure 3.19:** *Simulated hysteresis loops obtained for* $\theta = 5°$ *and* $\delta = 0°$, *with magnetic field* $H$ *applied along the y axis (red) and the x axis (black). The settled anisotropy coefficients are* $K_{alloy} = 0.66 \times 10^6\, erg\,/\,cm^3$ *and* $K_{Co} = 1.38 \times 10^6\, erg\,/\,cm^3$.

Moreover, figure 3.20(a) shows the loops obtained imposing both to the $AuCo$ matrix and to the $Co$ element the same anisotropy ($K_{alloy} = K_{Co} = 2.4 \times 10^6\, erg\,/\,cm^3$), whilst in figure 3.20(b) $K_{alloy} = 5 \times 10^6\, erg\,/\,cm^3$ and $K_{Co} = 2.4 \times 10^6\, erg\,/\,cm^3$ (namely, compared to the previous simulations, the anisotropy values for $AuCo$ and $Co$ have been exchanged). In both cases, we have set $\theta = 5°$ and $\delta = 0°$.

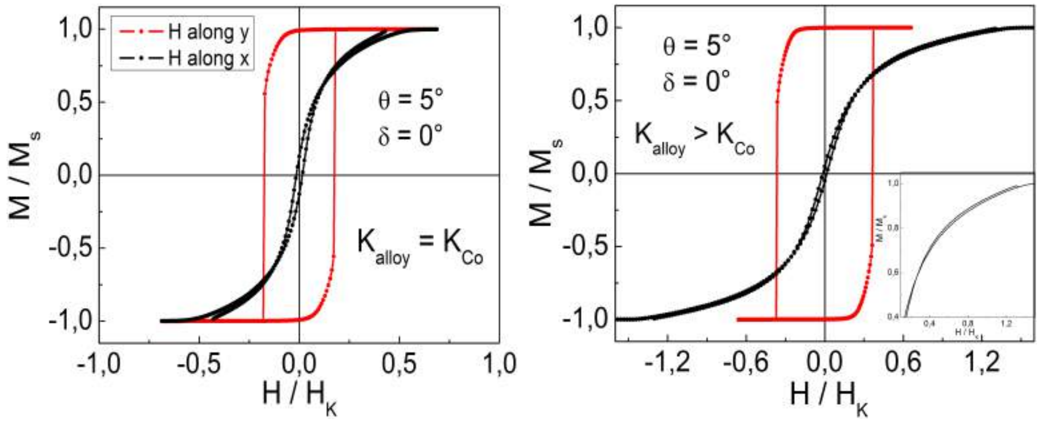

(a) (b)

**Figure 3.20:** *Simulated hysteresis loops obtained for* $\theta = 5°$ *and* $\delta = 0°$, *with magnetic field* $H$ *applied along the* $y$ axis (red) and the $x$ one (black). In (a) $K_{alloy} = K_{Co} = 2.4 \times 10^6\, erg\,/\,cm^3$; in (b) $K_{alloy} = 5 \times 10^6\, erg\,/\,cm^3$ and $K_{Co} = 2.4 \times 10^6\, erg\,/\,cm^3$. Inset of frame (b) : enlarged view of the loop measured with $H$ applied along the $x$ axis.

.

The main features of the hysteretic behavior are still visible even if the remanent magnetization measured along $x$ is substantially smaller than in figure 3.15(b); a characteristic that worsens the qualitative agreement with the experimental results. Finally, we have addressed the case of a sample with a higher $Co$ content. For this purpose, we have reduced the extension of the squared element drawn in figure 3.16, down to a size of 12 × 12 cells. In this way, the volume occupied by the $Co$ inclusion is $\sim$ 35 %, corresponding to the fraction that exists in sample $Au_1Co_2$ (table 3.2). Accordingly, we have assigned a magnetization $M_{s\_alloy} = 500\, emu\,/\,cm^3$(see section 3.2). All the remaining parameters are unchanged with respect to the simulations in figure 3.15. In particular, we present the results obtained for $\theta = 5°$ and $\delta = 0°$ (3.21(a)) and $\theta = 0°$ and $\delta = 5°$ (3.21(b)) to be compared with those in figures 3.15(b) and 3.17(a), respectively.

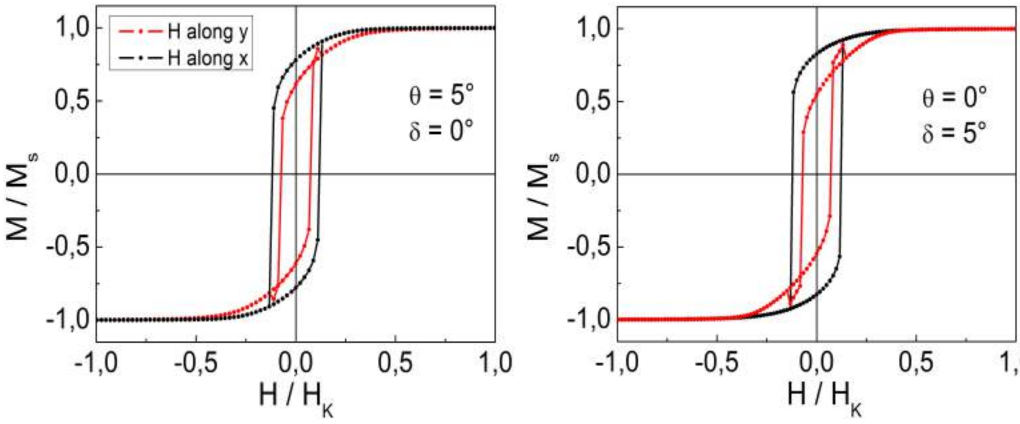

(a) (b)

**Figure 3.21:** *Simulated hysteresis loops obtained simulating a system slightly different from that schematized in figure 3.14, namely in which the volume fraction occupied by the* $Co$ *cluster is higher (*$\sim$ 35%*). Loops calculated for (a)* $\theta = 5°$ *and* $\delta = 0°$ *and (b)* $\theta = 0°$ *and* $\delta = 5°$*, with magnetic field* $H$ *applied along the* $y$ *(red) and the* $x$ *axis (black).*

.

The noteworthy outcome is that, in both cases, the high-remanence loop is that one measured along $x$ and cross-branching effect is visible in the loop along $y$. Hence, the easy and hard axes are exchanged with respect to the previous simulations, a situation that cannot be distinguished by experiments on the real samples.
Regarding the possibility of simulating the magnetic behavior of sample $Au_2Co_1$, the approach used for the other two samples is adversely affected by the inherent difficulty of assessing the fractions of non-relaxing and relaxing $Co$ clusters, which should be treated as two different magnetic phases, actually. However, it is worth mentioning that loops calculated for a smaller $Co$ element in figure 3.14 (correspond-

ing to a volume fraction of $\sim$ 10 %, table 3.2) and with the appropriate value of $M_{s\_alloy}$ (see section 3.2), show basic characteristics close to those found for sample $Au_1Co_1$.

Basically, our micromagnetic model, which takes the nanocomposite nature of our films into account, qualitatively well reproduced the observed experimental hysteretic behavior. Both experimental and theoretical results bring us to hypothesize that the anisotropy ruling the overall magnetic behavior has a prevalent magnetoelastic nature.

Chapter 4

# $80\,nm$ - thick continuous films

This chapter is mainly focused on the magnetic properties of the $80\,nm$-thick $AuCo$ continuous films. After a brief introduction on the compositional and structural properties of these samples (section 4.1), section 4.2 points the attention on both their hysteretic properties and how the magnetization reorentation process changes with respect to that observed in the thinner samples. The aim of this study is to highlight how the thickness influences the magnetic response of our $AuCo$ continuous films.

## 4.1 Compositional and structural features

As for the thinner samples (see section 3.1), a set of three typical films, with nominal thickness $\sim 80\,nm$ and $Au : Co$ concentration ratios of $2 : 1$, $1 : 1$ and $1 : 2$ (labelled as $Au_2Co_1$, $Au_1Co_1$ and $Au_1Co_2$), have been deposited at room temperature on natively oxidized (100)-silicon substrates with the magnetron co-sputtering apparatus used to grow the $30\,nm$-thick samples. The films have been realized at the same deposition conditions and a continuous $Co$ film, with thickness $(90 \pm 3)\,nm$, has been also deposited to be used as reference sample. Informations about the composition and the thickness of these films, acquired by RBS analyses together with SEM observations in cross-section mode, are reported in table 4.1.

**Table 4.1:** *Column 1: labels of the samples. Columns 2 and 3: Au and Co content in the films. Column 4: thickness of the films*

| Samples | Composition | | Thickness (nm) |
|---|---|---|---|
| | Au (at %) | Co (at %) | |
| $Au_2Co_1$ | 68 ± 1 | 32 ± 1 | 87 ± 3 |
| $Au_1Co_1$ | 47 ± 1 | 53 ± 1 | 87 ± 3 |
| $Au_1Co_2$ | 32 ± 1 | 68 ± 1 | 72 ± 3 |

Strucural results are substantially in agreement with those obtained on the thinner samples. EXAFS analysis has evidenced the presence of two phases: a $AuCo$ alloy, the prevalent phase which has an amorphous-like or poorly nanocrystalline nature, and segregated cobalt, in form of structurally disordered $Co$ nanoparticles dispersed within the $AuCo$ matrix, which mean size is about $2\,nm$, as revealed by XRD analysis [79]. To best fit the EXAFS spectra of the samples richer in $Au$, a very small amount of segregated $Au$ has been also considered. The BF-TEM analysis is in agreement with the EXAFS results and it highlights the inherent disorder of our systems. The estimated volume fractions of the different phases are reported in table 4.2. Also in this case, both the percentage of $Co$ in the alloy and the fraction of segregated $Co$ increase with decreasing the $Au : Co$ ratio.

**Table 4.2:** *Column 1: labels of the samples. Columns 2 and 3: volume fractions of the AuCo alloy, with its stoichiometry, and of segregated $Co$ and $Au$ (to convert atomic fractions to volume fractions, elemental atomic weights and densities have been used)*

| Samples | Volume fractions | | |
|---|---|---|---|
| | Alloy (vol %) | Co (vol %) | Au (vol %) |
| $Au_2Co_1$ | $Au_{80}Co_{20}$ 84 ± 8 | 11 ± 3 | 5 ± 4 |
| $Au_1Co_1$ | $Au_{73}Co_{27}$ 71 ± 10 | 28 ± 6 | 1 ± 0.8 |
| $Au_1Co_2$ | $Au_{57}Co_{43}$ 68 ± 9 | 32 ± 5 | 0 |

## 4.2 Magnetic results

The magnetic characterization of the $AuCo$ films has been carried out using the SQUID magnetometer (section 2.2) in a maximum applied field of $50\,kOe$, between $6\,K$ and $300\,K$. As in the case of the thinner samples, the sputtered films have been cleaved according to the crystallographic orientation of the substrate, so as to obtain pieces of about $(5 \times 5)\,mm^2$. The experimental loops magnetization have been corrected by subtracting the contribution of the diamagnetic substrate. In order to evaluate the saturation magnetization, the magnetic moment measured by SQUID has been divided by the magnetic film volume. The saturation magnetization of the reference $Co$ film has been also measured at $T = 6\,K$ and $T = 300\,K$. In the following, the SQUID hysteresis loops will be shown as normalized to $M_s$. To better elucidate the hysteretic behavior of the examined samples, their magnetic properties have been also investigated by measuring loops at room temperature using the MOKE apparatus (section 2.1).

In table 4.3, the values of saturation magnetization for the $AuCo$ samples, measured at $T = 6\,K$ and $T = 300\,K$ with an applied field $H = 50\,kOe$, have been reported.

**Table 4.3:** *Column 1: labels of the samples. Columns 2: saturation magnetization ($M_s$) measured at temperature $T = 6\,K$ in $H = 50\,kOe$. Column 3: $M_s$ at $T = 300\,K$. The main error source is the uncertainty of the sample thickness.*

| Sample | $M_s$ at $T = 6\,K$ $(emu/cm^3)$ | $M_s$ at $T = 300\,K$ $(emu/cm^3)$ |
|---|---|---|
| $Au_2Co_1$ | 289 ± 9 | 182 ± 5 |
| $Au_1Co_1$ | 566 ± 18 | 520 ± 16 |
| $Au_1Co_2$ | 755 ± 27 | 741 ± 27 |

The results are in agreement with the $M_s$ values of the $30\,nm$-thick samples (table 3.3) and figure 4.1 shows the values of $M_s$ as a function of the $Co$ volume fraction for both the thicker films and the thinner ones. In both cases, the saturation magnetization proportionally increases with increasing the $Co$ content.

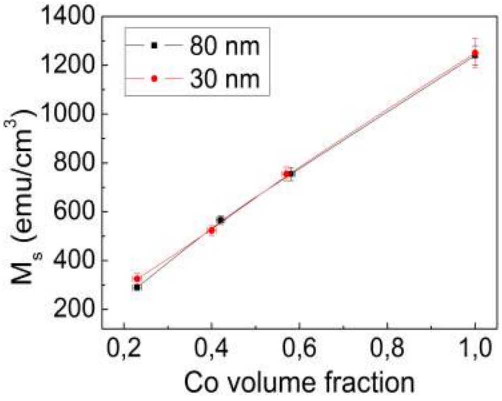

**Figure 4.1:** *Saturation magnetization values measured at $T = 6\,K$ in $H = 50\,kOe$ in function of the $Co$ volume fraction in the film: $80\,nm$-thick samples (black squares) and $30\,nm$-thick samples (red circles). In some cases, the error bar is smaller or comparable to the symbol size. Solid lines are guides to the eye.*

At the lowest T, the value of the saturation magnetization of the reference $Co$ film is slightly lower than the one measured on the 22 $nm$-thick $Co$ sample (see section 3.2) and, within the error, it is not seen to appreciably depend on temperature in the investigated $T$ range. This is probably due to the absence of a cap layer and it is reasonable to assume an oxidation process at the surface of the sample as confirmed by our low temperature magnetic analysis. Previous works on $Co\,/\,CoO$ systems [113], obtained by exposing the freshly deposited $Co$ layer to a pure oxygen atmosphere, established about $\sim\ 3\,nm$ as the thickness of the oxidated surface. Taking this thickness value into account, the calculated value of the saturation magnetization is $M_s\ =\ 1240 \pm 40\, emu\,/\,cm^3$ at $T\ =\ 6\,K$. Based on both the volume fractions of the different phases (table 4.2) and on the saturation magnetization values of the films (table 4.3) and using, for the segregated cobalt, the $M_s$ of the reference $Co$ sample, calculated values of saturation magnetization for the $AuCo$ alloys at $T\ =\ 6\,K$ are $\sim\ 190\, emu/cm^3$ for sample $Au_2Co_1$, $\sim\ 310\, emu/cm^3$ for $Au_1Co_1$ and $\sim\ 530\, emu/cm^3$ for $Au_1Co_2$ (because of the uncertainties on the data in tables 4.2 and 4.3, the relative error associated to these values ranges between 22 % and 38 %).

### 4.2.1 Measured hysteretic behavior and interpretation

Information on the magnetic properties of the $AuCo$ samples and on their magnetic structure has been gained by the study of the hysteresis loops and, in the case of the samples richer in $Co$, by a Magnetic Force Microscopy (MFM) analysis (in collaboration with the Instituto Nazionale di Ricerca Metrologica (I.N.RI.M)).
First, let us consider the sample $Au_1Co_2$. Figures 4.2(a) and 4.2(b) show the loops measured along two in-plane orthogonal directions corresponding to the sides of the sample at $T\ =\ 6\,K$ and $T\ =\ 300\,K$, respectively. In both cases, the film appears isotropic and this feature is preserved in all the investigated range of temperatures ($6\,K$ - $300\,K$).

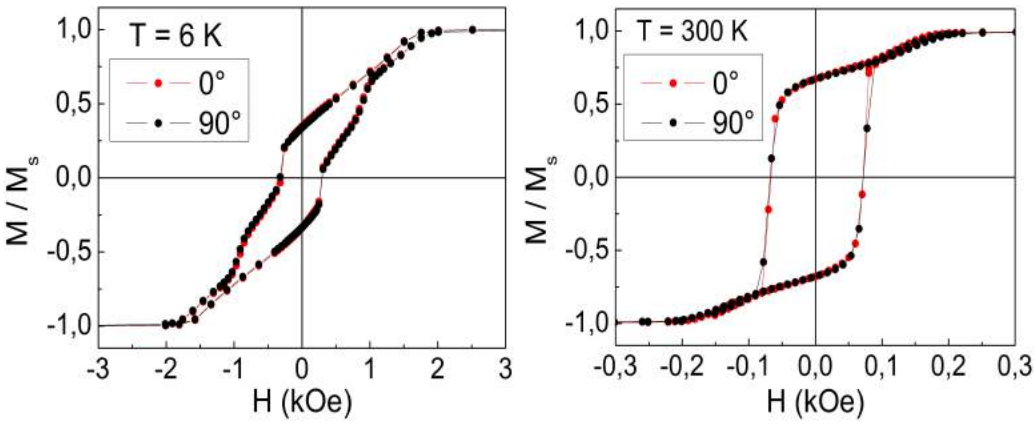

(a) (b)

**Figure 4.2:** *In-plane hysteresis loops measured on sample* $Au_1Co_2$ *along two orthogonal directions, labelled as* $0^\circ$ *(red) and* $90^\circ$ *(black), at* $T = 6\,K$ *(a) and* $T = 300\,K$ *(b).*

.

The $H_c$ and $M_r\,/\,M_s\,vs\,T$ dependencies are displayed in figures 4.3(a) and 4.3(b).

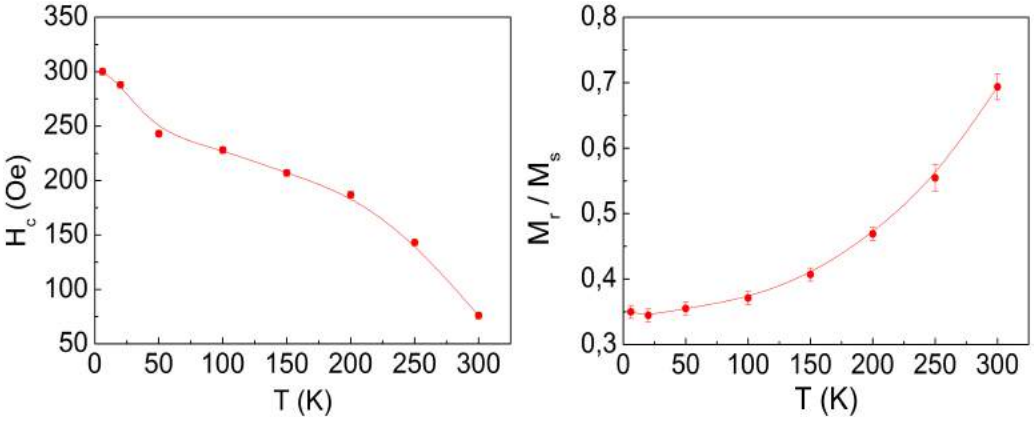

(a) (b)

**Figure 4.3:** *(a) Coercivity* $H_c$ *and (b) squarness ratio* $M_r\,/\,M_s$ *vs.* $T$ *measured on sample* $Au_1Co_2$*. In some cases, the error bar is smaller or comparable to the symbol size.*

.

The hysterestic behavior is clearly different with respect to that observed in the thinner $Co$-rich sample ( subsection 3.2.1): $H_c$ values are higher in all the investigated temperature range (figure 4.3(a)) and $M_r\,/\,M_s$ values visibly increase with rising temperature (figure 4.3(b)). Moreover, the shape of the hysteresis loop measured at $T = 300\,K$ closely resembles that of a system with a stripe domain magnetic structure [42, 52] displaying two distinct slopes: a steep magnetization jump occuring close to the coercitive field ($H_c$) and a linear behavior between remanence and saturation. Typically, in this magnetic configuration, the presence of both easy in-plane and slightly tilted out of the surface plane anisotropy directions gives rise to the, so called, "rotatable anisotropy" [114, 115]: the average stripe domain orientation defines an in-plane easy axis that corresponds to the direction of the last in-plane saturating field. Hence, it implies that the shape of the hysteresis loops should be the same in all in-plane directions. Figure 4.4(a) shows the longitudinal MOKE measurements with a magnetic field applied along three different orientations at $T = 300\,K$ whilst, in figure 4.4(b), a typical MFM image, taken at the remanence state after applying an in-plane saturating field at room temperature, is displayed.

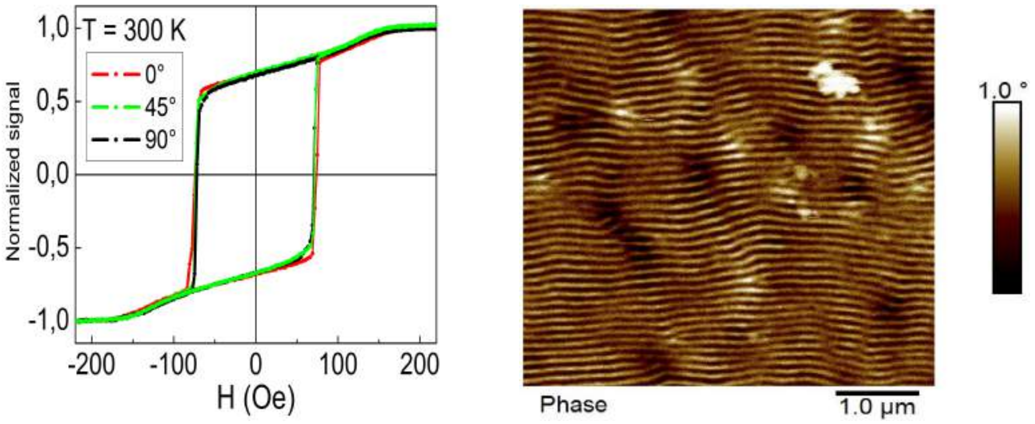

(a) (b)

**Figure 4.4:** *(a) In-plane hysteresis loops measured on sample* $Au_1Co_2$ *at* $T = 300\,K$ *by MOKE magnetometry along three different orientations of the applied field, labelled as* $0°$ *(red),* $45°$ *(green) and* $90°$ *(black). Direction* $0°$ *is along one side of the sqaured sample. (b) MFM image of the remanent domain structure after applying an in-plane saturating field at* $T = 300\,K$*. The scanning area is of* $5\,\mu m \times 5\,\mu m$*.*

.

As expected, a stripe domain structure is observed (4.4(b)). The magnetization of the film at remanence, after being saturated in one of the in-plane directions, lies within a plane that is normal to the film surface and oscillates between pointing slightly upward (bright contrast) and slightly downward (dark contrast) relative to the film plane. Under an in-plane applied field, the stripe domain experience a relaxation process [117] wherein the region of the stripes whose magnetization is parallel to the applied field grows through domain wall movement giving rise to the characteristic shape of the hysteresis loop (figures 4.2(b) and 4.4(a)). The period of the stripes is estimated to be $w_{ex} \sim 125\,nm$. The presence of dark spots in the MFM image is probably related to defects which, acting as pinning centers, reduce the distance between the stripes; the narrow gap could lead to a local increase of the dipolar interactions between neighboring stripes inducing a simple domain structure [116].

A stripe domain structure is only energetically favorable when the contribution of the perpendicular magnetic anisotropy (PMA) to the overall magnetic behavior is strength enough. Figure 4.5 shows the hysteresis loops measured with both in-plane and out-of-plane applied field at $T = 6\,K$ (4.5(a)) and $T = 300\,K$ (4.5(b)).

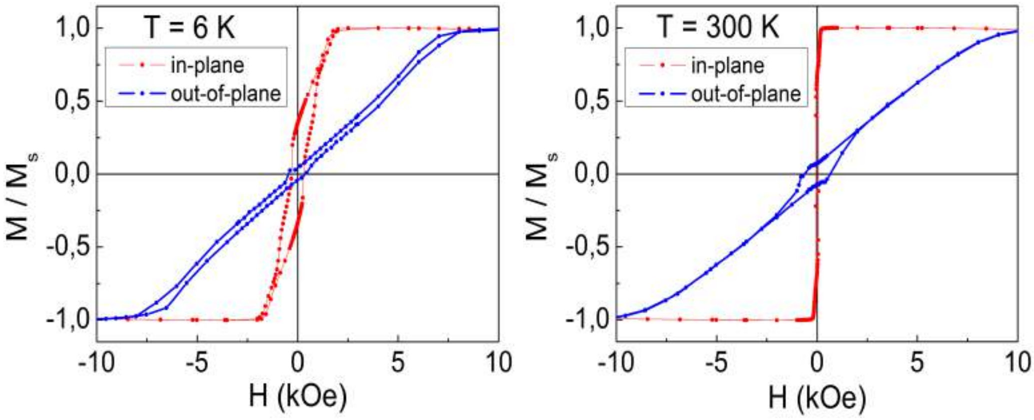

(a) (b)

**Figure 4.5:** *Magnetic hysteresis loops measured on sample $Au_1Co_2$ with in-plane applied magnetic field (red) and out-of-plane applied magnetic field (blue): at $T = 6\,K$ (a) and $T = 300\,K$ (b). The displayed in-plane hysteresis loops are measured along the $0°$ direction.*

.

The comparison between the in-plane and out-of-plane saturation fields ($H_K$) suggests that the overall magnetization easy axis mainly lies in the plane of the film. The PMA decreases passing from $6\,K$ to $300\,K$ and this effect is probably responsable for the increase of the in-plane squarness ratio with rising temperature (4.3(b)); however, at $T = 300\,K$, as confirmed by the MFM analysis (4.4(b)), the PMA strength is sufficient to sustain a stripe domain configuration. The presence of a stripe domain configuration can be evaluated in term of the PMA and the demagnetizing film energy densities ratio $Q = \frac{K_N}{2\pi {M_s}^2}$, where $K_N$ is the PMA energy density [119, 120]. The PMA energy density $K_N$ can be estimated from the in-plane hysteresis loops by the Stoner-Wohlfarth model [104] as $K_N = \frac{M_s H_K}{2}$. Its value decreases from $K_N \sim 7.6 \times 10^5\,erg/cm^3$ at $T = 6\,K$ down to $K_N \sim 9.3 \times 10^4\,erg/cm^3$ at

$T = 300\,K$. Thus, estimated $Q$ values go from $\sim 0.21$ down to $\sim 2.7 \times 10^{-2}$ with increasing temperature. These results are consistent with the presence of a weak stripe domain structure [51] with a significant amount of magnetization component parallel to the sample plane: the magnetization vector performs a weak out-of-plane oscillation around an average in-plane magnetization direction that lies along the stripe domain direction (4.4(b)).

The formation of a stripe domain structure is related to the existance of a critical thickness below which the shape anisotropy is too large for the stripe domain to exist. The critical thickness ($t_c$) can be fairly accurately expressed by the simple equation [121]:

$$t_c = 2\pi\sqrt{\frac{A}{K_N}}\,, \tag{4.1}$$

where $A$ is the exchange stiffness of the material under consideration. In our case, at room temperature, $K_N$ has been experimentally determined whilst a value of $A$ is quite difficult to estimate also due to the inherent structural disorder of such a system. Firstly, $A$ has been calculated as a weighted mean by multiplying the values attributed to the magnetic phases constituting the film ($A_{Co} = 3\,\mu erg/cm$ and $A_{alloy} = 0.2\,\mu erg/cm$, see subsection 3.2.2 for further details) by the relative volume of each phase (see table 4.2), so as to take the nanocomposite nature of our system into account. However, by setting $A \sim 1.1\,\mu erg/cm$, the value of $t_c$ strongly disagree with the sample thickness ($t_c \sim 216\,nm$). Secondly, by the light of the experimental results, we have supposed that the value of the critical thickness corresponds to the sample one. This assumption brings us to give a plausible estimation of the overall exchange stiffness of the material ($A \sim 1.2 \times 10^{-7}\,erg/cm$); in particular, this value will be used in the following chapter to simulate the hysteretic behavior of a Nano Holes Array system grown in the same deposition batch of the $Au_1Co_2$ continuous film. Moreover, taking these values into account and assuming a Landau domain structure, we can also estimate the stripe domain period of our sample as [120]:

$$w_{th} = 4\sqrt{2t\sqrt{\frac{A}{K_N}}}\,, \tag{4.2}$$

where $t$ is the sample thickness. The result ($w_{th} \sim 163\,nm$) is a good estimate of the experimental one ($w_{ex} \sim 125\,nm$).

To further underline the nanocomposite nature of this system and the consequent complex mechanism which rules the overall hysteretic behavior, figure 4.6 shows an enlarged view of the superposed hysteresis loops measured at $T = 6\,K$, $T = 50\,K$, $T = 100\,K$ and $T = 150\,K$, respectively. The decrease of the temperature and the resulting increase of the PMA leads to highlight diverse magnetic phases characterized by different coercitive fields.

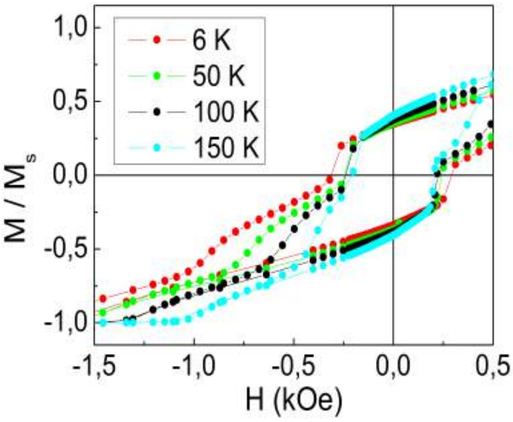

**Figure 4.6:** *Enlarged view of the superposed magnetic in-plane hysteresis loops measured on sample $Au_1Co_2$ at $T = 6\,K$ (red), $T = 50\,K$ (green), $T = 100\,K$ (black) and $T = 150\,K$ (sky blue).*

Considering now the sample $Au_1Co_1$, the loops measured at $T = 6\,K$ along two in-plane orthogonal directions corresponding to the sides of the sample are shown in figure 4.7

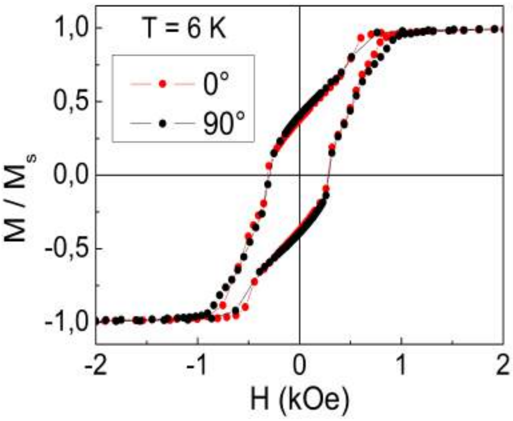

**Figure 4.7:** *In-plane hysteresis loops measured on sample $Au_1Co_1$ at $T = 6\,K$ along two orthogonal directions, labelled as $0°$ (red) and $90°$ (black).*

The sample appears isotropic in the plane, but it turns to anisotropic with rising temperature. Figures 4.8(a) and 4.8(b) shows the hysteresis loops measured along the two orthogonal directions at $T = 130\,K$ and $T = 300\,K$, respectively.

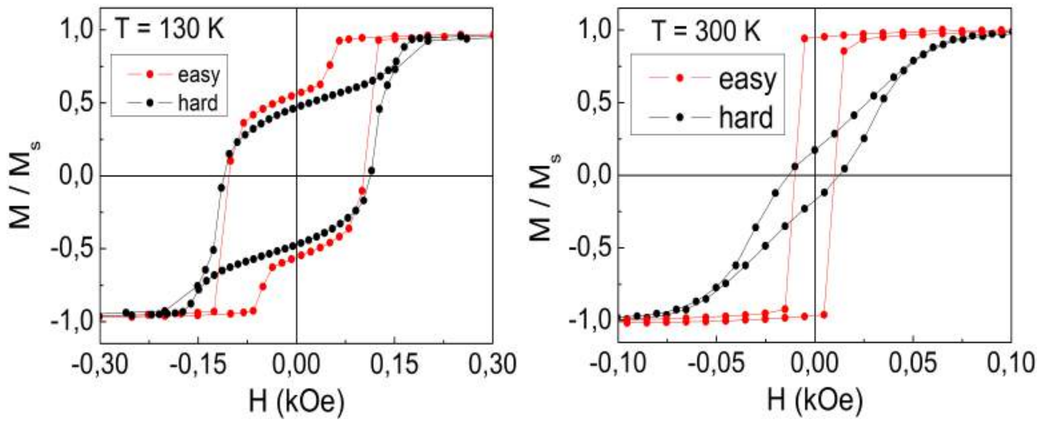

(a) (b)

**Figure 4.8:** *In-plane hysteresis loops measured on sample $Au_1Co_1$ along the easy (red) and hard (black) orthogonal axes at $T = 130\,K$ (a) and $T = 300\,K$ (b).*

At $T = 300\,K$, the magnetic behavior is clearly anisotropic: along one direction the loop is highly squared, being the ratio between remanent magnetization and saturation magnetization $M_r\,/\,M_s \sim 0.90$, while, along the orthogonal direction, the loop appears stretched and $M_r\,/\,M_s \sim 0.15$. The applied field direction corresponding to the high-remanence loop is a preferential magnetization axis, i.e an in-plane easy axis; accordingly, the orthogonal one represents an in-plane hard magnetization axis. Loops measurements by MOKE magnetometry, performed at different angles ($T = 300\,K$), support this assumption.

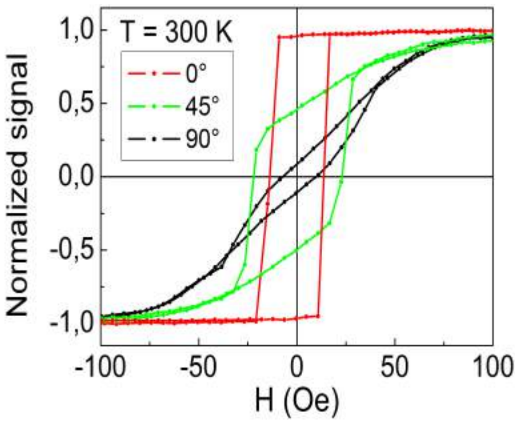

**Figure 4.9:** *In-plane hysteresis loops measured on sample $Au_1Co_1$ at $T = 300\,K$ by MOKE magnetometry along three different directions labelled as $0°$ (red), $45°$ (green) and $90°$ (black). Direction $0°$ is along one side of the squared sample.*

The loops with the higher and lower remanence are those measured along the side of the sample, as in the case of the thinner film (see subsection 3.2.1).
At $T = 130\,K$ the hysteretic behavior is different with respect to that observed at room temperature. Starting from positive saturation, both the hysteresis loops (figure 4.8(a)) show a first step followed by an almost linearly decreasing of the magnetization with decreasing the applied field and, finally, a second steep magnetization jump at the coercivity field, $H_c$. These irreversible switchings of the magnetization are more pronounced for the loop measured along the easy axis whilst the linear behavior is well visible in the loop measured along the hard direction.
The curves of $M_r\,/\,M_s$ vs $T$, measured along the easy and hard axes, are shown in figure 4.10.

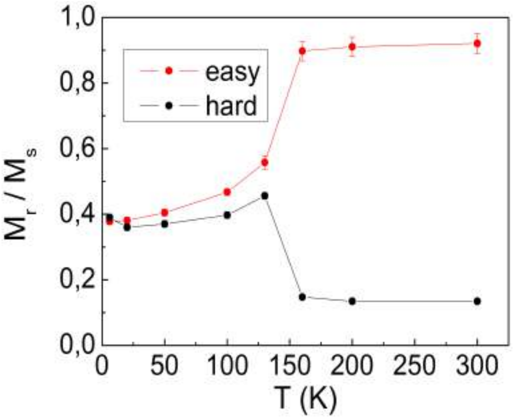

**Figure 4.10:** *Squarness ratio $M_r\,/\,M_s$ vs $T$ measured on sample $Au_1Co_1$ along the easy (red) and hard (black) orthogonal axes. In some cases, the error bar is smaller or comparable to the symbol size. Solid lines are guides to the eye.*

The anisotropic character of the magnetization reversal process begins to be evident at $T \sim 100\,K$ and an abrupt change of the magnetic behavior occurs at $T \sim 150\,K$. Beyond this temperature, the hysteretic properties are similar to those found in the $Au_1Co_1$ thinner sample, except for the crossing of the branches of the loops measured along the hard magnetization direction (see subsection 3.2.1). Figure 4.11 shows the trend of $H_c$ vs $T$ measured on both the thicker sample and the thinner one along their easy magnetization axes (the curves measured along the hard magnetization axes display similar features).

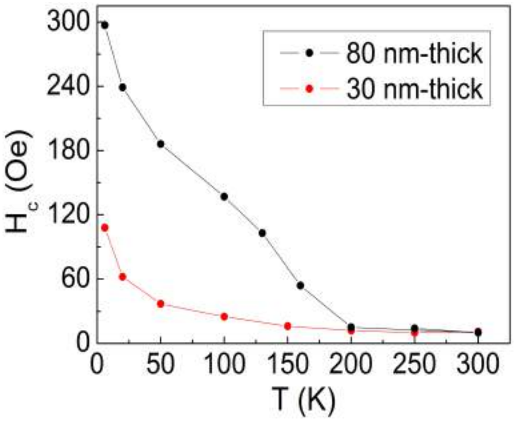

**Figure 4.11:** *Coercitivity $H_c$ vs $T$ measured on sample $Au_1Co_1$: $80\,nm$-thick sample (black), $30\,nm$-thick sample (red). In both cases, the values measured along the easy magnetization axis are shown. In some cases, the error bar is smaller or comparable to the symbol size. Solid lines are guides to the eye.*

At low temperature ($T \leq 150\,K$), the values of $H_c$ are higher for the thicker sample and the gap increases with decreasing the temperature, whilst beyond $T \sim 150\,K$ the curves are superposed.

By the light of these results, the in-plane hysteretic behavior at low $T$, similar to that observed in the sample richer in $Co$, could be an hint of the presence of a PMA. Figure 4.12 shows the hysteresis loops measured with both in-plane and out-of-plane applied field at $T = 6\,K$ and $T = 300\,K$, respectively.

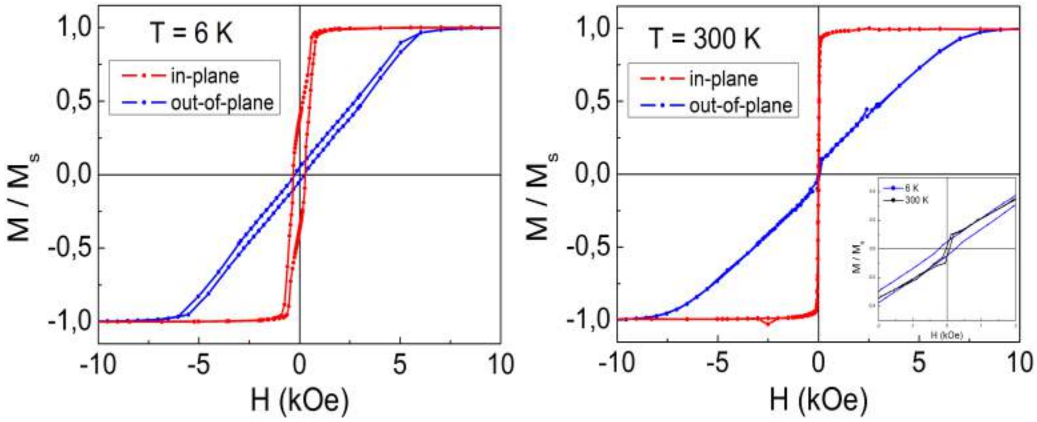

(a) (b)

**Figure 4.12:** *Magnetic hysteresis loops measured on sample $Au_1Co_1$ with in-plane (red) and out-of-plane (blue) applied field: at $T = 6\,K$ (a) and $T = 300\,K$ (b). The displayed in-plane hysteresis loops are measured along the easy direction. The inset of frame (b): enlarged view of the out-of-plane loops measured at $T = 6\,K$ (blue) and $T = 300\,K$ (black).*

The PMA is clearly observed at $T = 6\,K$ whilst it is substantially absent at $T = 300\,K$. To estimate the PMA contribution to the overall magnetic behavior, we can evaluate the $Q$ factor. Its value is $\sim 0.15$ at $T = 6\,K$ (similar to that calculated for the sample richer in $Co$, $Q \sim 0.21$) and it rapidly decreases with temperature; beyond $T \sim 100\,K$, $Q$ is smaller with respect to that calculated for the sample $Au_1Co_2$ at $T = 300\,K$. As expected, MFM analyses at $T = 300\,K$ reveal a substantially planar magnetic structure.

As for the sample $Au_2Co_1$, the magnetic behavior is isotropic in all the investigated temperature range and, as an example, figure 4.13 shows the hysteresis loops measured along two orthogonal directions corresponding to the side of the squared sample at $T = 6\,K$ and $T = 100\,K$, respectively.

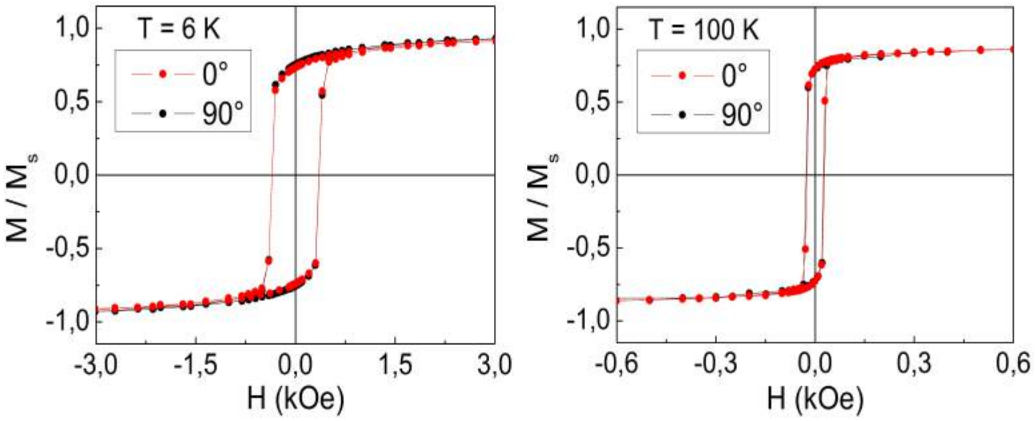

(a) (b)

**Figure 4.13:** *In-plane hysteresis loops measured on sample* $Au_2Co_1$ *along two orthogonal directions, labelled as* $0°$ *(red) and* $90°$ *(black) at* $T = 6\,K$ *(a) and* $T = 100\,K$ *(b).*

$H_c$ and $M_r\,/\,M_s$ are plotted as functions of $T$ in figures 4.14(a) and 4.14(b), respectively.

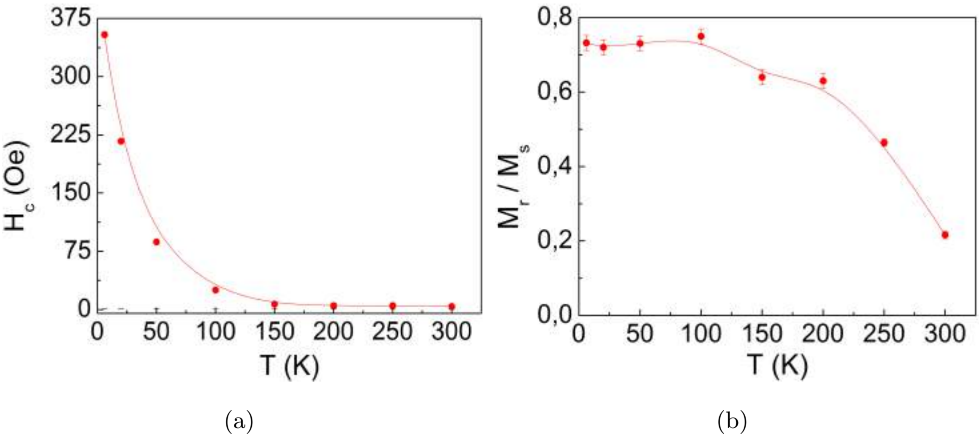

(a) (b)

**Figure 4.14:** *(a) Coercitivity $H_c$ and (b) squarness ratio $M_r\,/\,M_s$ vs $T$ measured on sample $Au_2Co_1$. In some cases, the error bar is smaller or comparable to the symbol size. Solid lines are guides to the eye*

At the lowest temperature $H_c$ is higher than in the other investigated samples ($H_c \sim 354\,Oe$) and it strongly decreases with increasing temperature especially up to $T \sim 100\,K$ (at $T = 100\,K$, $H_c \sim 25\,Oe$).

The overall hysteretic behavior of the sample richer in $Au$ is somewhat different compared to the other films and, a remarkable difference is also a clear non-saturation tendency of the loops, which becomes more pronounced with increasing temperature (hence, for this sample, the values of $M_s$ in table 4.3, taken as those measured at $H = 50\,kOe$, may be slightly underestimated; however, the saturation magnetization value is expected to lie within the indicated error bar). This effect is well visible in figure 4.15 showing the first quadrant of the loop measured at $T = 300\,K$. It is to be noted that a reduction of $M_s \sim 37\%$ is experienced with increasing temperature from $T = 6\,K$ up to $T = 300\,K$, whilst it is not larger than $\sim 8/\%$ in the samples richer in $Co$.

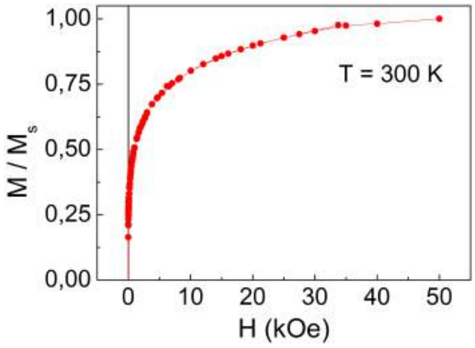

**Figure 4.15:** *First quadrant of the loop measured on sample $Au_2Co_1$ at $T = 300\,K$.*

As in the case of the $Au_2Co_1$ thinner sample, the magnetization $M$ has been measured for increasing temperature in the $6\,K$-$300\,K$ range in $H_{appl} = 20\,Oe$, after cooling the sample from room temperature down to $6\,K$ both without an external field (zero-field-cooling, ZFC) and in $H_{appl}$ (field-cooling, FC). The results are shown in figure 4.16(a).

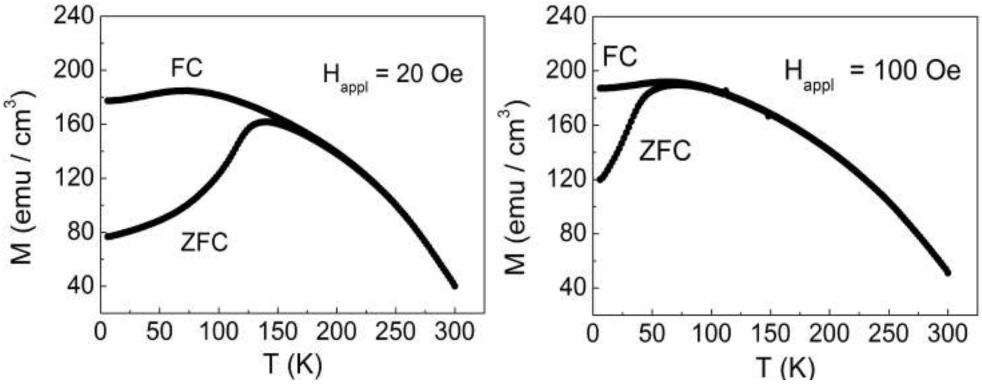

(a) (b)

**Figure 4.16:** *Zero-field-cooling (ZFC) and field-cooling (FC) magnetization as function of temperature measured on sample $Au_2Co_1$ in applied magnetic field $H_{appl} = 20\,Oe$ (a) $H_{appl} = 100\,Oe$ (b).*

Magnetic irreversibility, namely the difference between FC and ZFC magnetization, is clearly observed from $T = 6\,K$ up to $T \sim 150\,K$, where the ZFC displays a peak. Some features have to be underlined. The value of $M_{FC}$ at $T = 6\,K$ corresponds to more than $60\,\%$ of the total measured $M_s$ ($\sim 289\,emu/cm^3$, see table 4.3) in agreement with the presence of a large fraction of ferromagnetically soft phase; moreover, for $T > 150\,K$, the ZFC and FC branches exhibit a downward concavity, consistent with the existance of a monotically decreasing ferromagnetic background. A similar ZFC-FC magnetization measurement in $H_{appl} = 100\,Oe$ is shown in figure 4.16(b). Compared to the previous case, with increasing $H_{appl}$, the ZFC peak appears at lower temperature, as expected for an assembly of nanoparticles undergoing magnetic relaxation [86]; for $T > 70\,K$ the ZFC and FC branches are superposed and show a monotonous decreasing trend.

The strong thermal dependence of $M_s$, the trend of $H_c$ vs $T$ (figure 4.14(a)), the marked non-saturation tendency with increasing temperature (figure 4.15) and the magnetic irreversibility effect, clearly observed through ZFC-FC measurements (figures 4.16(a) and 4.16(b)), are features similar to those observed in the $Au_2Co_1$ thinner sample. The magnetic behavior seems consistent with the presence of $Co$

clusters (i.e, aggregates of $Co$ particles) which, due to the increasing of the temperature, undergo magnetic relaxation processes similar to superparamagnetism [87]: $H_c$ and $M_r\,/\,M_s$ are not seen to go to zero at high $T$, as expected in the case of ideal superparamagnetism [40]. However, some features bring us to hypothesize that their magnetic size is different with respect to that characterizing the magnetic $Co$ clusters of the $Au_2Co_1$ thinner sample; in particular, it can account for both larger $H_c$ of the thicker film at low $T$ (at $T = 6\,K$, $H_c \sim 354\,Oe$) compared to that of the thinner one (at $T = 6\,K$, $H_c \sim 235\,Oe$) and the diverse area of the magnetic irreversibility region, visible by the comparison between the figures 4.16(a) and 3.13(a). A different strength of the exchange coupling between the $Co$ particles and the ferromagnetic $AuCo$ matrix and between neighboring $Co$ particles could lead to a diverse magnetic size and, consequently, to a distinct amount of relaxing and non-relaxing $Co$ clusters. In this framework, the presence of a larger amount of non-relaxing $Co$ clusters could explain the trend of $M_r\,/\,M_s$ at low T even if, at high $T$ ($T > 100\,K$), as experienced, the overall hysteretic behavior is mainly ruled by magnetic relaxation processes.

Moreover, as in the case of the films richer in $Co$, sample $Au_2Co_1$ presents an amount of PMA as highlighted in figure 4.17, which shows the hysteretic loops measured at $T = 6\,K$ with both in-plane and out-of-plane applied field.

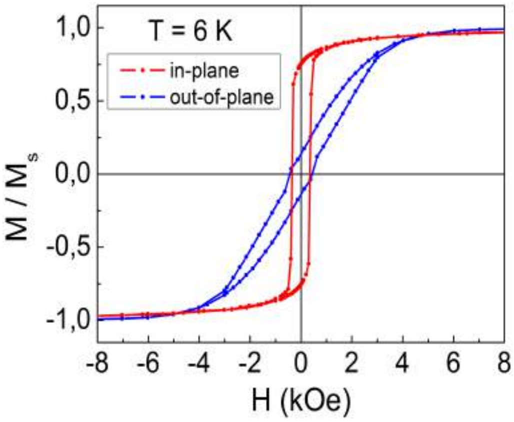

**Figure 4.17:** *Magnetic hysteresis loops measured on sample* $Au_2Co_1$ *at* $T = 6\,K$ *with in-plane magnetic field (red) and out-of-plane magnetic field (blue).*

However, it is difficult to give an estimate of the contribution of the PMA to the overall magnetic behavior because of the presence of the superparamagnetic-like behavior affecting the magnetization reorentation process.

The presence of PMA, as confirmed by our experimental observations, is a common feature of the 80 $nm$-thick continuous films and it influences the overall magnetic behavior. The existance of an easy out-of-plane magnetization axis is probably related to a partially spin reorentation transition (SRT) from in-plane to out-of-plane with increasing the film thickness. This phenomenon is quite well known and it is observed in $CoFeTaB$ [122] and $FeBSi$ [51] magnetostrictive amorphous films deposited by sputtering technique. In such systems, the presence of an effective perpendicular anisotropy component is due to an increase of the stress present in the film. A similar mechanism can be accounted for our structures; for the investigated thickness range, an increase of the thickness usually leads to an increase of the stress present in the films [123] which influences the magnetoelastic anisotropy ruling the magnetic behavior.

The presence of PMA depends on the $Au : Co$ ratio and it increases with increasing the $Co$ content. Sample $Au_1Co_2$ exhibits a weak stripe domain magnetic structure whilst, in the sample richer in $Au$, its existence (at very low $T$) may be partially masked by a dominant superparamagnetic-like behavior. As for sample $Au_1Co_1$, the presence of a perpendicular anisotropy component strongly decreases with increasing the temperature and it vanishes at $T \sim 150\,K$; this effect marks the occurance of a spin reorentation temperature-driven transition from a slightly out-of-plane to a substantial in-plane alignment of the magnetization vector and it manifests itself through an abroupt change in the shape of the measured in-plane hysteresis loops. An analogous phenomenon has also been observed in $CoFeTaB$ amorphous films [122] and it is reasonably related to a temperature dependent magnetostrictive interaction [44]. In our case, the transition is also accompanied by a change from isotropic to anisotropic behavior with increasing temperature. At high $T$, namely when the magnetization mainly lies in the plane of the sample, the magnetic behavior is similar to that observed in the $Au_1Co_1$ thinner film and, as well depicted in the previous chapter, it could be a hint of the coexistence of at least two magnetostrictive interacting phases, namely a $AuCo$ alloy and $Co$ clusters, subjected to a non-uniform in-plane stress distribution.

Chapter 5

# Nano Holes Array Systems

This chapter is mainly dedicated to the analysis of the magnetic properties of $AuCo$ nanostructures in form of Nano Holes Array (NHA) systems. Section 5.1 briefly describes the syntesis procedure and the morphological properties whilst section 5.2 presents the preliminary magnetic results obtained on these structures. The aim of the following chapter is to highlight how the nanostructuring process influences the overall hysteretic behavior.

## 5.1 Synthesis procedure and morphological properties

To provide a full description of both the synthesis procedure and the morphological characterization is beyond the scope of the present thesis; only the principal results are reported in this section, further informations can be found in [79].

NHAs have been produced by Nano Sphere Litography (NLS) [124, 125], a high-throughput and cost-effective technique which allows to finely tune the morphology of the NHA and it consists in employing a Self-Assembles Monolayer (SAM) of Polystyrene (PS) nanospheres as a deposition mask. In our case, a hexagonal close-packed single monolayer has been used as the mask and the steps needed to complete the preparation of the NHAs are summarized in figure 5.1.

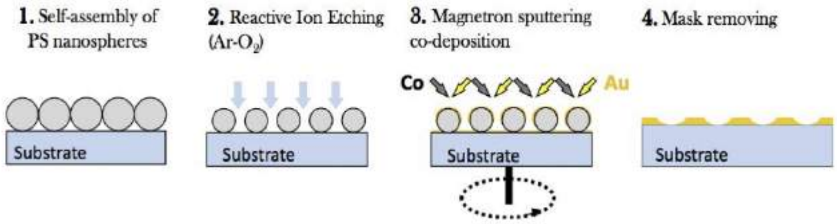

**Figure 5.1:** *Schematic diagram of the synthesis process of the NHAs: 1) self-assembly of a PS nanospheres mask on a silicon substrate; 2) Reactive Ion Etching process using as etching gas a mixture of Argon and Oxygen; 3) co-sputtering deposition of $Au$ and $Co$; 4) removal of the PS mask by an adhesive tape.*

The self-assembly of the PS nanospheres mask on a natively oxidized (100)-silicon substrate has been followed first by the Reactive Ion Etching process (RIE) in order to reduce the PS nanospheres diameter and, then, by the magnetron co-sputtering deposition. NHAs have been deposited in the same batch of the $80\,nm$-thick films according to the process parameters detailed in section 3.1. Three compositions have been produced with nominal stoichiometry $2:1$, $1:1$ and $1:2$; labelled as $Au_2Co_1$_NHA, $Au_1Co_1$_NHA and $Au_1Co_2$_NHA, respectively. It is reasonable to assume that, given the gap between the etched nanospheres ($\sim 240\,nm$), the mechanisms of growth of the metallic coating are the same as for the continuous samples. After the deposition, the PS nanospheres mask has been removed by an adhesive tape. The final result is a $AuCo$ film which contains hexagonal arrays of nanoholes. The morphological features have been studied through $SEM$ and $AFM$ analyses. The following pictures display SEM and BF-SEM representative images of our systems, respectively.

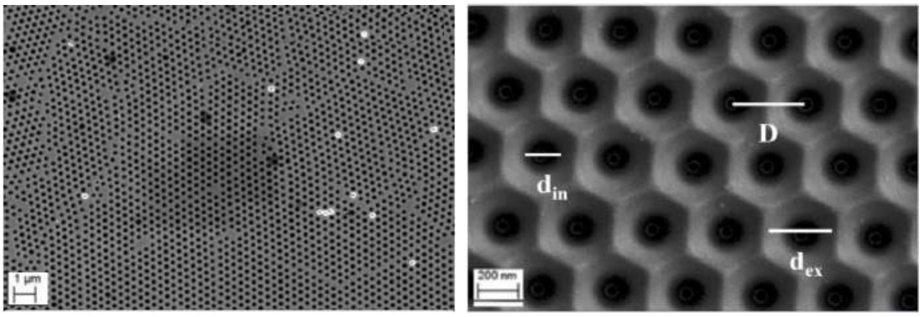

(a) (b)

**Figure 5.2:** *(a) SEM image of a representative NHA aquired at a magnification of $50\,kX$; (b) FE-SEM image of a representative NHA aquired at a magnification of $100\,kX$ by the secondary electron detection in order to enhance the morphological features. See text for further details.*

Figure 5.2(a) is an overview of our structures and, despite an hexagonal short range order, it is evident the lack of a long range order; the BF-SEM image (figure 5.2(b)), representing a zoom of a specific area, highlights how the morphology of the NHA is very complex. Due to the deposition process, part of the sputtered material has been also deposited in an anular region underlying the PS nanospheres [79]. The highest ring surrounding the holes, which presents cusp-like structures seemingly positioned at the edge of an hexagon, decreases towards the voids according to a spherical profile. In the figure 5.2(b) three different distances are highlighted: the distance between adjacent holes ($D = 522 \pm 12\,nm$), the diameter of the uncovered area ($d_{in} = 280 \pm 10\,nm$) and the diameter of the spherical-shaped pores ($d_{ex} = 510 \pm 50\,nm$).

The thickness of the NHAs have been evalueted through AFM measurements as the height of the highest point of the ring surrounding the holes; the results are in agreement with this thickness being about $\sim 10\,\%$ less than that measured on the corresponding continuous film. The values of the thickness of our systems are reported in table 5.1.

**Table 5.1:** *Column 1: labels of the samples. Column 2: thickness of the NHAs.*

| Sample | thickness (nm) |
|---|---|
| $Au_2Co_1$_NHA | 79 ± 5 |
| $Au_1Co_1$_NHA | 79 ± 5 |
| $Au_1Co_2$_NHA | 65 ± 5 |

## 5.2 Magnetic results

The hysteretic properties of the NHAs have been studied in the $6\,K$-$300\,K$ temperature range using the SQUID magnetometer (section 2.2) and, at room temperature, with the MOKE apparatus (section 2.1), as well. As in the case of the corresponding continuous films, the samples have been cleaved according to the crystallographic orientation of the substrate so to obtain pieces of about $(5 \times 5)\,mm^2$. The SQUID hysteresis loops have been corrected for the diamagnetic contribution of the $Si$ substrate and normalized to the measured saturation magnetic moment.

The values of saturation magnetization ($M_s^{exp}$) for the NHAs, measured at $T = 6\,K$ and $T = 300\,K$ in $H = 50\,kOe$, are reported in table 5.2 (columns 2 and 3, respectively); they have been obtained by dividing the measured magnetic moment by the volume occupied by both the sputtered material and the holes. In order to compare these results with those obtained on the continuous films, we have corrected the $M_s^{exp}$ values considering the effective volume occupied by the magnetic material. In this frame, the table 5.2 also displays the saturation magnetization values ($M_s^{th}$) calculated as the ratio between $M_s^{exp}$ and the fill factor ($f$) for both $T = 6\,K$ and $T = 300\,K$. This parameter, assuming a hexagonal-ordered array of cylindrical-shaped holes, can be written as:

$$f = 1 - [(d'/2D) \cdot \frac{2\pi}{\sqrt{3}}] , \tag{5.1}$$

where $D$ is the distance between adjacent holes (see section 5.1) and $d'$ is the diameter of the cylindrical holes, evaluated, in our case, as $d' = \frac{d_{in}+d_{ex}}{2}$. The result is $f = 0.48 \pm 0.08$.

**Table 5.2:** *Column 1: labels of the samples. Columns 2 and 3: saturation magnetization ($M_s^{exp}$) measured in $H = 50\,kOe$ at $T = 6\,K$ and $T = 300\,K$, respectively. Columns 4 and 5: saturation magnetization ($M_s^{th}$) calculated taking the effective volume occupied by the magnetic material into account at $T = 6\,K$ and $T = 300\,K$, respectively; the main error source is the uncertainty of the fill factor.*

| Samples | $M_s{}^{exp}$ $(emu/cm^3)$ | | $M_s{}^{th}$ $(emu/cm^3)$ | |
|---|---|---|---|---|
| | $T = 6\,K$ | $T = 300\,K$ | $T = 6\,K$ | $T = 300\,K$ |
| $Au_2Co_1$_NHA | 105 ± 7 | 62 ± 4 | 220 ± 40 | 129 ± 23 |
| $Au_1Co_1$_NHA | 260 ± 17 | 236 ± 15 | 540 ± 100 | 490 ± 90 |
| $Au_1Co_2$_NHA | 400 ± 30 | 376 ± 29 | 820 ± 150 | 780 ± 140 |

The calculated $M_s^{th}$ values are in agreement with those measured on the corresponding continuous films (see table 4.3); figure 5.3 shows the comparison at $T = 6\,K$.

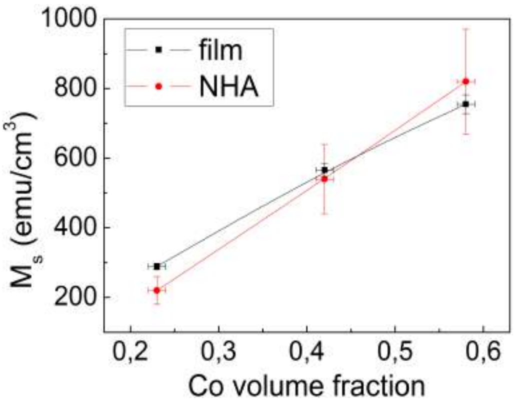

**Figure 5.3:** *Saturation magnetization values measured at $T = 6\,K$ for the $80\,nm$-thick continuous films (black squares) and $M_s^{th}$ values calculated at $T = 6\,K$ for the NHAs (red circles) in function of the $Co$ volume content in the sample. Solid lines are guides to the eye.*

### 5.2.1 Measured hysteretic behavior and micromagnetic simulations

The magnetic analysis has been carried out both from an experimental point of view, through the study of the hysteretic properties and the use of the MFM technique, and from a micromagnetic point of view employing the OOMMF software [101]. First, let us consider the magnetic behavior of the sample richer in $Au$. Figure 5.4(a) shows the hysteresis loops measured at $T = 6\,K$ along two orthogonal directions, corresponding to the side of the squared sample in order to mantain the same measurement procedure used for the continuous films. The sample appears isotropic and this behavior persists at higher temperature. A marked non-saturation tendency occurs with increasing the temperature; in this frame, figure 5.4(b) displays the first quadrant of the hystersis loop measured at $T = 300\,K$. Because of this feature, the values of $M_s^{exp}$ in table 5.2, taken as those measured at $H = 50\,kOe$, may be slightly underestimated.

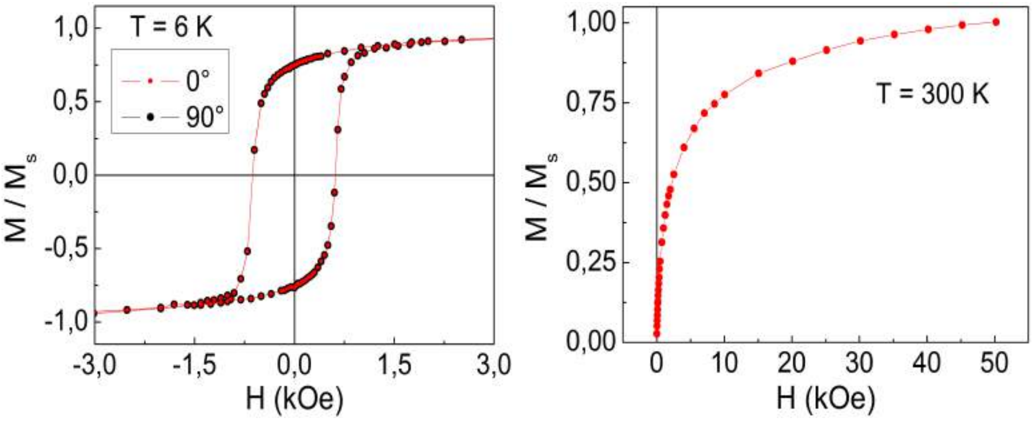

(a) (b)

**Figure 5.4:** *(a) In-plane hysteresis loop measured on sample* $Au_2Co_1$*_NHA at* $T = 6\,K$ *along two orthogonal directions, labelled as* $0°$ *(red) and* $90°$ *(black). (b) First quadrant of the hysteresis loop measured at* $T = 300\,K$*.*

$H_c$ and $M_r\,/\,M_s$ are plotted as functions of $T$ in figures 5.5(a) and 5.5(b), respectively.

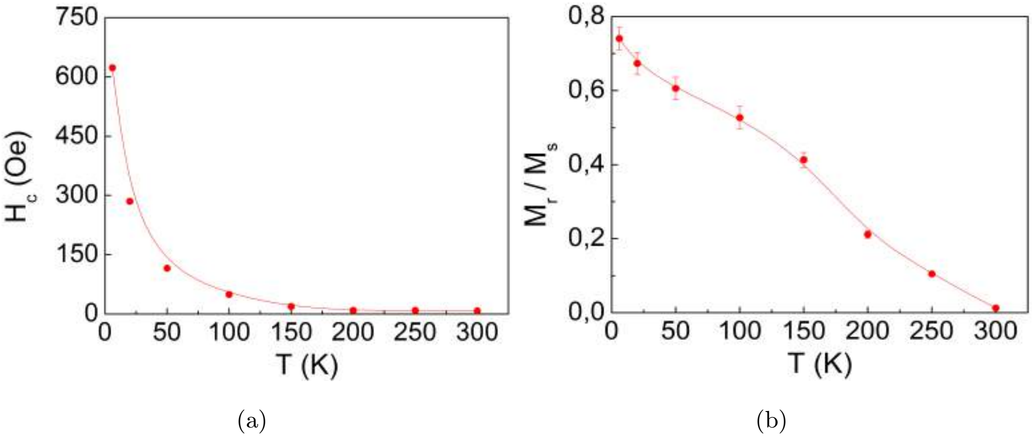

**Figure 5.5:** *(a) Coercivity $H_c$ and (b) squarness ratio $M_r\,/\,M_s$ vs $T$ measured on sample $Au_2Co_1$_NHA. In some cases, the error bar is smaller or comparable to the symbol size. Solid lines are guides to the eye.*

The clear non-saturation tendency of the room temperature magnetization loop, the trend of $H_c$ and $M_r\,/\,M_s$ vs $T$ and the strong thermal dependence of the saturation magnetization (a reduction of $M_s^{exp} \sim 41\,\%$ is experienced with increasing temperature from $T = 6\,K$ to $T = 300\,K$, see table 5.2) are features similar to those observed in the corresponding continuous sample. Hence, the overall hysterestic behavior is consistent with the presence of small $Co$ clusters, in form of aggregates of magnetically interacting $Co$ nanoparticles, which, due to the increasing of the temperature, undergo a magnetic relaxation process. However, in this case, this superparamagnetic-like behavior is more marked: at the lowest temperature $H_c$ is higher than in the $Au_2Co_1$ continuous film ($H_c \sim 623\,Oe$) and the decrease of the squarness ratio with increasing temperature appears more evident. The overall magnetic behavior seems to be completely ruled by very fine $Co$ entities which are blocked at low temperature and undergo a relaxation process as temperature is increased: at $T = 300\,K$, both the coercitivity and the squarness ratio are nearly to zero.

The hysteretic behavior of the NHAs richer in $Co$ presents similar features. Figures 5.6(a) and 5.6(b) show the hysteresis loops measured at $T = 6\,K$ along two orthogonal directions on the samples $Au_1Co_1$_NHA and $Au_1Co_2$_NHA, respectively. As in the case of the continuous films, the applied field directions correspond to the sides of the NHAs. At the lowest $T$, the samples appear isotropic and this magnetic behavior persists up to higher temperatures.

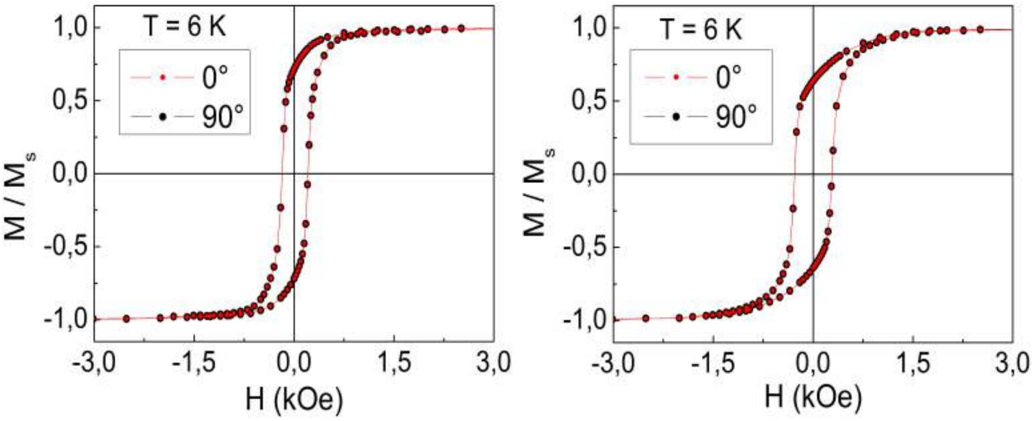

(a) (b)

**Figure 5.6:** *In-plane hystersis loops measured at* $T = 6\,K$ *along two orthogonal directions, labelled as* $0°$ *(red) and* $90°$ *(black): (a)* $Au_1Co_1$*_NHA and (b)* $Au_1Co_2$*_NHA.*

An hexagonal arrangement of the holes should favour a six-fold simmetry of the magnetic anisotropy [59, 66] with alternating hard magnetization axis and easy magnetization axis every 30° degrees, according to the symmetry of the lattice. In our specific case, as well depicted in figure 5.2(a), showing the lack of a hexagonal long range order, the overall magnetization is prevented from following the in-plane directions imposed by the local easy axes, hence, preferred in-plane magnetization directions are not expected. The isotropic character of the hysteretic behavior of our systems is highlighted by the previously shown low temperature SQUID loops and by the data presented in figures 5.7(a) and 5.7(b) showing the room temperature hystersis loops measured by MOKE magnetometry rotating the direction of the applied magnetic field of 30° degrees.

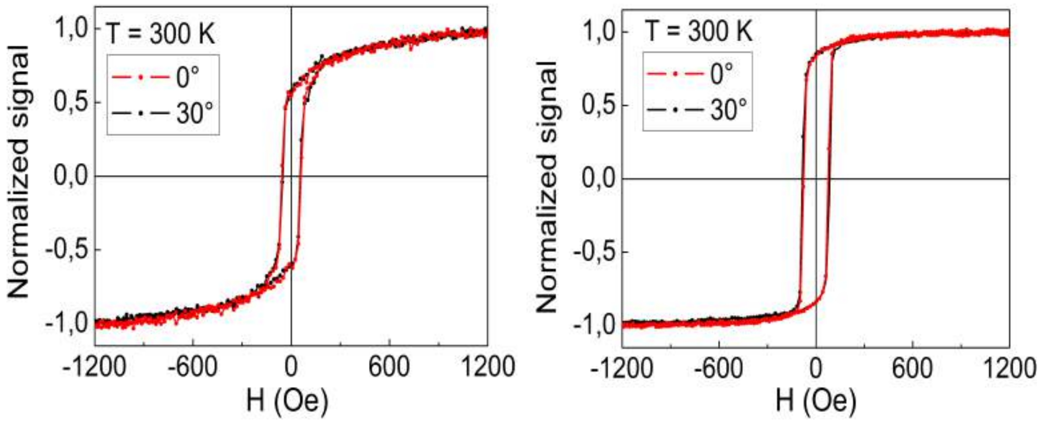

(a) (b)

**Figure 5.7:** *In-plane hysteresis loops measured at* $T = 300\,K$ *by MOKE magnetometry along two different orientations of the applied field, labelled as* $0°$ *(red) and* $30°$ *(black): (a)* $Au_1Co_1$*_NHA and (b)* $Au_1Co_2$*_NHA.*

The curves of $H_c$ and $M_r\,/\,M_s$ vs $T$ for the two samples are displayed superposed in figures 5.8(a) and 5.8(b), respectively.

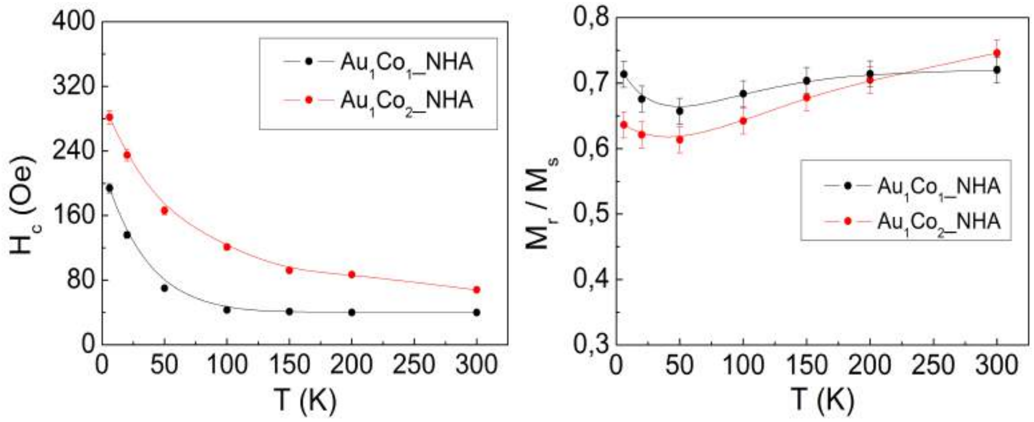

(a) (b)

**Figure 5.8:** *(a) Coercivity* $H_c$ *and (b) squarness ratio* $M_r\,/\,M_s$ *vs* $T$ *measured on samples* $Au_1Co_1$*_NHA (black) and* $Au_1Co_2$*_NHA (red). In some cases, the error bar is smaller or comparable to the symbol size. Solid lines are guides to the eye.*

The hysteretic properties are different with respect to those observed in the corresponding continuous films; the loops' shape — in particular, in the field region close to the remanent state — and the trend of $H_c$ and $M_r\,/\,M_s$ vs $T$ are a clear evidence of that. Hence, the experimental observations show that the shape anisotropy induced by the nanostructuring process influences the overall hysteretic behavior. To highlight what is its role in determining the magnetization reversal process and how its contribution changes with varying the temperature, we can analyze both what is the relation between the coercive field and the saturation magnetization and how these two quantities evolve as a function of the temperature. In both the studied cases, we will show the results obtained on the sample $Au_1Co_2$_NHA; similar conclusions can be drawn for the sample $Au_1Co_1$_NHA.

Figure 5.9(a) displays the trend of $H_c\,/\,{M_s}^{exp}$ vs $T$. If the hysteretic behavior of the system was only ruled by the contribution of the shape anisotropy induced by the nanostructuring process the two quantities should vary proportionally and, hence, the ratio between coercivity and saturation magnetization should be constant (within the error). Figure 5.9(a) shows that the ratio increases with decreasing temperature (very markedly at low $T$) and, hence, the experimental evidence is a hint of the probable existence of other sources of anisotropy which, at low $T$, contribute to the magnetization reversal process.

Figure 5.9(b) shows the trend of $H_c$ and ${M_s}^{exp}$ as a function of the temperature; both curves are normalized to the corresponding value at $T\,=\,6\,K$.

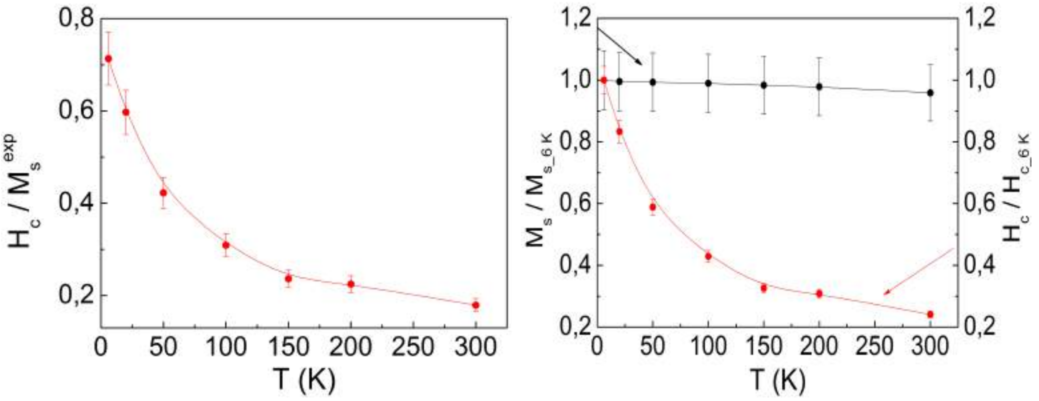

(a) (b)

**Figure 5.9:** *(a) Ratio* $H_c\,/\,{M_s}^{exp}$ *measured on sample* $Au_1Co_2$*_NHA. (b) Coercivity* $H_c$ *(red) and saturation magnetization* ${M_s}^{exp}$ *(black) vs* $T$ *measured on sample* $Au_1Co_2$*_NHA. Both the curves are normalized to the corresponding value at* $T\,=\,6\,K$*. In some cases, the error bar is smaller or comparable to the symbol size. Solid lines are guides to the eye.*

As well highlighted, the curves display different features: the trend of the saturation magnetization appears nearly constant, whilst the coercive field increases with decreasing temperature, very markedly at low T ($T \leq 150\,K$).
Hence, the outcomes underline that the induced shape anisotropy mainly rules the magnetization reversal process at room temperature whilst the decrease of the temperature activates magnetic mechanisms which significantly influence the overall hysteretic behavior. Figures 5.10(a) and 5.10(b) display the hysteresis loops measured at $T = 6\,K$ with both in-plane and out-of-plane applied field for the samples $Au_1Co_1$_NHA and $Au_1Co_2$_NHA, respectively.

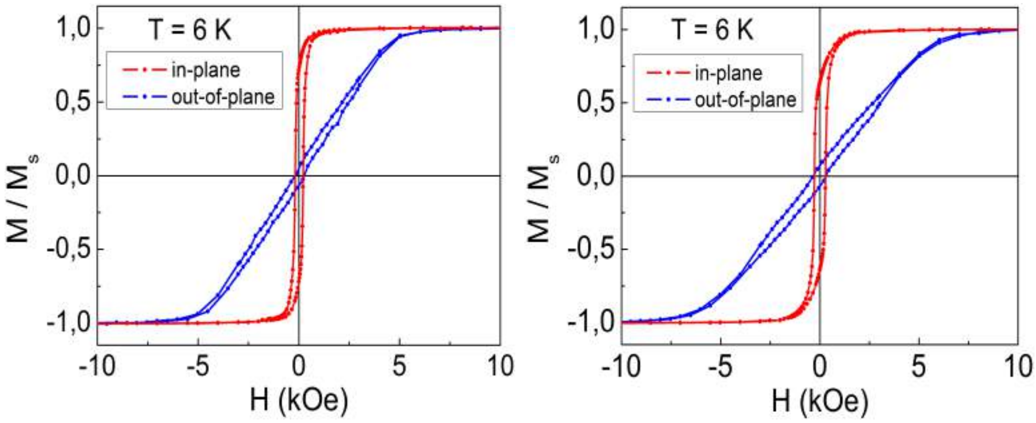

(a) (b)

**Figure 5.10:** *Magnetic hysteresis loops measured at $T = 6\,K$ with in-plane (red) and out-of-plane (blue) applied field: (a) $Au_1Co_1$_NHA and (b) $Au_1Co_2$_NHA.*

At the lowest $T$, despite the magnetization mainly lies in the plane of the film, it is clearly visible the presence of a PMA contribution which disappears with increasing temperature; at $T = 300\,K$, its presence is totally absent.
In order to elucidate the experimental results and to better understand the role of the induced shape anisotropy, micromagnetic calculations have been performed using the OOMMF software [101]. We have simulated the magnetic behavior of an ideal hexagonally ordered nanoholes array. The total volume of the modelled system is $(520 \times 900 \times 70)\,nm^3$, discretized using cells with a basis of $(10 \times 10)\,nm^2$ and an height of $7\,nm$. $2D$ periodic boudary conditions have been applied to avoid effects due to the finite size of the modelled system. In particular, the chosen geometry takes the morphological properties of our structures into account (see section 5.1) and figure 5.11 displays both a section (figure 5.11(a)) and a three-dimensional overview (figure 5.11(b)) of the simulated system. Our micromagnetic model neglets

the presence of the magnetic material located close to the centre of the nanoholes as its amount is expected to be neglibible [79] and, consequently, that is expected to give a negligible contribution to the overall magentization process.

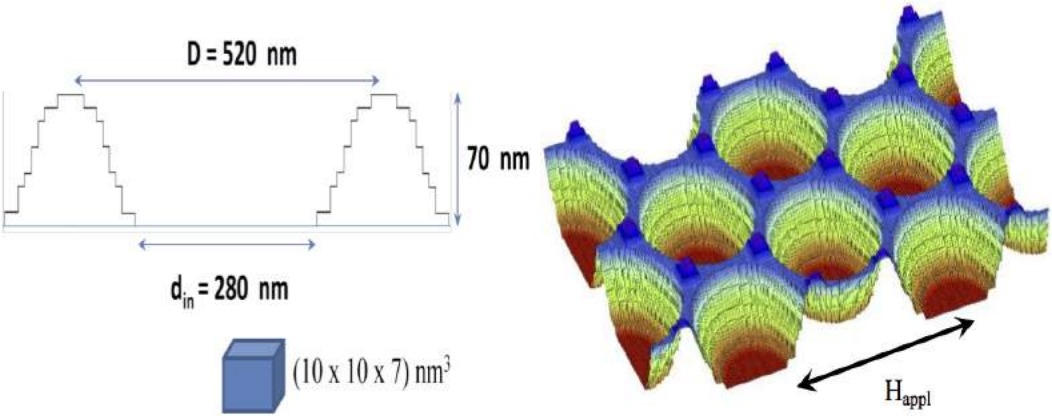

(a) (b)

**Figure 5.11:** *(a) Section and (b) $3D$ overview of the simulated system. The distance between the adjacent holes is $D = 520\,nm$, the diameter of the holes located in the lower layer is $d_{in} = 280\,nm$ and the height of the system is $70\,nm$. The highest ring surrounding the nanoholes presents cusp-like structures located at the edge of a hexagon and it decreases towards the voids according to a spherical-like profile. In (b) the direction of the in-plane applied magnetic field ($H_{appl}$) is displayed.*

The magnetic parameters have been coerently settled with the experimental data of the $Au_1Co_2$ continuous film at $T = 300\,K$; namely, the temperature for which the effects related to the induced shape anisotropy seems more marked. The saturation magnetization of the system has been fixed to $M_s = 741\,emu\,/\,cm^3$ (see table 4.3) whist the assigned exchange stiffness is $A = 1.2 \times 10^{-7}\,erg\,/\,cm$, corresponding to the estimated value in order to explain the formation of a stripe domain structure at $T = 300\,K$ (see subsection 4.2.1 for further details). The shape anisotropy is assumed to be the only source of magnetic anisotropy of the simulated system so to verify its role in controlling the magnetization reversal process. The calculated hysteresis loops have been obtained by applying an external magnetic field both in-plane, along an easy magnetization direction (see figure 5.11(b)), and perpendicular to the surface plane of the system in order to verify if the only presence of the shape anisotropy is sufficient to explain the existence of PMA. In both cases, to mimic the experimental loop measurement procedure our calculations start from the positive magnetic saturation state. The in-plane and out-of-plane simulated hysteresis loops are displayed in figures 5.12(a) and 5.12(b), respectively; in both cases, the corresponding room temperature experimental loop measured with SQUID magnetometry is superposed.

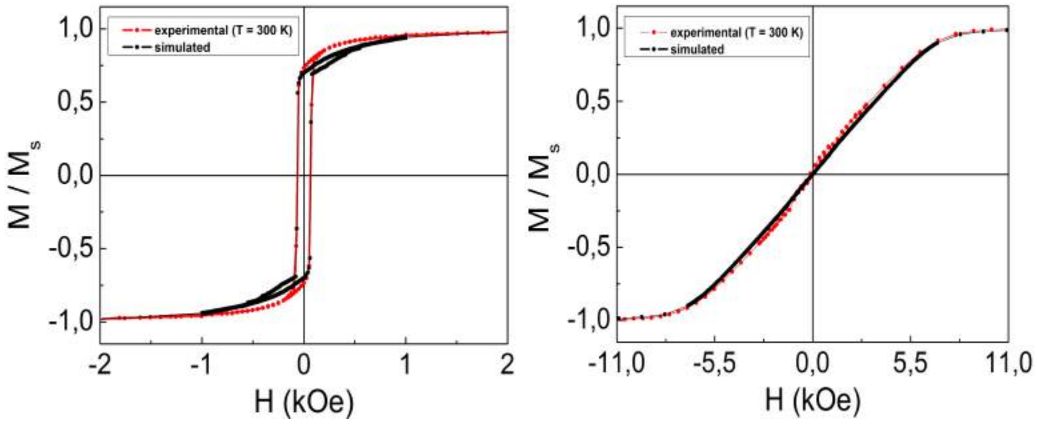

(a) (b)

**Figure 5.12:** *(a) In-plane hysteresis loop measured on sample* $Au_1Co_2$*_NHA by SQUID magnetometry at* $T = 300\,K$ *(red) and simulated cycle calculated with an external magnetic field applied in the system plane, along an easy magnetization direction (black); (b) out-of-plane hysteresis loop measured on sample* $Au_1Co_2$*_NHA by SQUID magnetometry at* $T = 300\,K$ *(red) and simulated cycle calculated by applying a magnetic field perpendicular to the system plane (black).*

The micromagnetic results are in perfect agreement with the experimental ones. The in-plane hysteresis loops show similar features as the approach to the remanence state; the coercive fields, namely the switching fields, are the same, actually. Figure 5.12(b) displays the absence of a PMA contribution and it highlights that the simulated and the experimental anisotropy field, namely the magnetic field needed to align the magnetization along the out-of-plane direction, are very similar. Moreover, figure 5.13(a) shows a map of the stray magnetic field distribution at the remanence state taken from the top of our simulated system; as well depicted, the shape induces the formation of magnetic dipoles located in correspondence of the cusp-like structures. The existence of this magnetic behavior has been experimentally verified by MFM analysis, suitable technique to investigate the local magnetic structures. Figure 5.13(b) displays a typical MFM image of the sample $Au_1Co_2$_NHA taken at the remanence state after applying a saturating field along an in-plane direction at $T = 300\,K$.

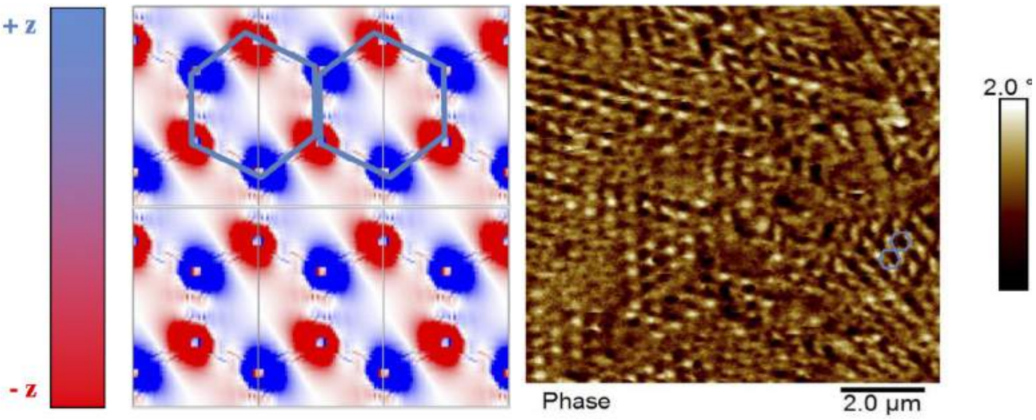

(a) (b)

**Figure 5.13:** *(a) Map of the simulated dispersed field distribution (z-component) taken at the remanence state; the strength of the stray magnetic field is presented by a colour bar. (b) MFM image of the sample* $Au_1Co_2$*_NHA taken at the remanence state after applying a saturating field along an in-plane direction at* $T = 300\,K$*; the scanning area is of* $10\,\mu m \times 10\,\mu m$*. The aim of the blue hexagons is to improve the comparison between the two images, shown at different scales.*

Basically, our micromagnetic model demonstrates how the induced shape anisotropy plays a crucial role in controlling the magnetization reversal process at high $T$.

Moreover, the calculations further confirm that other magnetic mechanisms contribute to the overall hysteretic behavior at low $T$; indeed, the simulated hysteretic features are not expected to significantly change when using, as an estimate for $M_s$, the $6\,K$ value ($M_s = 755\,emu\,/\,cm^3$, see table 4.3) in place of the $300\,K$ one ($M_s = 741\,emu\,/\,cm^3$).

The strength of the coercive field and the presence of PMA at low $T$ could be related to the existence of an amount of residual stress inside the system and, consequently, to the presence of a source of magnetoelastic anisotropy. However, a different scenario can be proposed. In polycrystalline NHAs, the polycrystallinity of the material related to the morphological features of the system can favour an out-of-plane orientation of the overall magentization [126]; the local easy axes of the system do not necessarily need to be aligned completely in-plane but may favour an out of plane orientation of the magnetization thanks to the interplay between the randomly oriented magnetocrystalline anisotropy and the shape anisotropy induced by the nanostructuring process. In our specific case, the presence of a fraction of small $Co$ particles or very fine $Co$ clusters could explain this magnetic behavior; at low $T$, these $Co$ entities are blocked and probably responsible for the existence of local easy magnetization axes which are slightly tilted with respect to the surface plane. An estimation of the PMA contribution in the two samples, exploiting the value of the out-of-plane saturating field [127, 128], is unable to provide exhaustive information on this item. This finding confirms that this contribution, if present, may have a reduced intensity with respect to that found in the corresponding continuous films.

Therefore, to fully understand the hysteretic behavior at low $T$, further structural and magnetic analyses should be done. The structural investigations could verify the possible existence of unpatterned regions and what is their actual occupied area; MFM measurements at low $T$ could elucidate the presence and the position of magnetic domains with a remarkably out-of-plane magnetization component. In addition, the existence of a PMA contribution originated by the presence of a residual stress in the system, or of a random magnetocrystalline anisotropy, to take the contribution of $Co$ clusters into account, could be introduced in our simulated system, so to compare the effects of the two presented scenarios on the hysteretic behavior of the samples.

In conclusion, it is evident that the induced shape anisotropy has a crucial impact on the overall hysteretic behavior. In particular, the hysteretic properties of the NHA samples are different with respect to those observed in the corresponding continuous films, leading to hyphotesize a significant reduction of the magnetoelastic contribution to the magnetization reversal process.

# Conclusions

The research presented in this thesis has been mainly focused on the magnetic analysis of $AuCo$ nanocomposite systems in form of both continuous films and Nano Holes Array structures, grown by sputtering co-deposition technique. This method, working far from the thermodinamic equilbrium, has turned out to be effective in alloying $Au$ and $Co$. In more detail, the structural investigations have indicated that the samples mainly consist of an almost amorphous alloy in which $Co$ nanoparticles are dispersed and the two phases are finely intermixed. Indeed, the study of the hysteretic properties has revealed the nanocomposite magnetic structure of these systems disclosing peculiar magnetic behaviors. Moreover, the micromagnetic analysis has offered an important tool to gain insight into the origin of the magnetization reversal process.

Firstly, we have analyzed the magnetic properties of $30\,nm$-thick continuous films with different atomic ratio of the constituent metals. They show an unexpected hysteretic behavior, characterized by in-plane anisotropy and branch-crossing effect in the loops measured along the hard magnetization direction, despite the deposition procedure which favours an uniform coverage of the substrate. These peculiar hysteretic features have been identified as a hint of the coexistence of at least two magnetic interacting phases: a prevalent ferromagnetic $AuCo$ alloy in which $Co$ clusters, namely aggregates of magnetically interacting $Co$ nanoparticles, are dispersed. This hypothesis has been supported by calculations performed on a micromagnetic model composed of two exchange-coupled ferromagnetic phases. Those calculations have succeeded in attaining general guidelines regarding how the observed hysteretic properties may originate in the investigated material. Both experimental and theoretical results bring us to assume that the anisotropy ruling the magnetic behavior of the two magnetic phases has a prevalent magnetoelastic nature. This implies that both phases must be magnetostrictive and subjected to a non-uniform in-plane stress distribution. This last observation, in particular, can offer interesting implications for the creation of novel engineered structures; this feature could be intentionally induced exploiting flexible substrates so to obtain a fine control of the overall anisotropy and, hence, of the loop shape.

Secondly, in order to study how the thickness influences the magnetic response of our $AuCo$ samples, we have focused our attention on $80\,nm$-thick continuous films with the same nominal stoichiometry of the thinner ones. Our magnetic analyses have revealed how the presence of a perpendicular magnetic anisotropy is a common feature of the thicker films; the existence of an easy out-of-plane magnetization axis is probably related to a partial spin reorentation transition from in-plane to out-of-plane with increasing the film thickness. Indeed, the increase of the thickness influences the overall hysteretic behavior; it can lead to an increase of the stress present in the films and, accordingly, enhance the strength of the magnetoelastic anisotropy thus promoting the spin reorentation. Moreover, as well highlighted by our magnetic analyses, another parameter which influences the presence of the PMA is the $Au$:$Co$ ratio. The strength of the PMA has been found to increase with increasing the $Co$ content. At $T = 300\,K$, the formation of a weak stripe domain magnetic structure occurs in the sample richer in $Co$ whilst the balanced composition presents hysteretic features similar to those observed in the corresponding thinner film and the PMA contribution to the overall magnetic behavior is absent. The room temperature hysteretic behavior of the sample richer in $Au$ is dominated by a superparamagnetic-like behavior and the possible presence of PMA at low $T$ is unstimable.

Finally, we have studied the magnetic behavior of $AuCo$ nanostructures in form of Nano Holes Array systems. These samples have been produced by Nano Sphere Litography and grown in the same deposition batch of the $80\,nm$-thick continuous films. The aim of this study has been to highlight how the nanostructuring process influences the overall hysteretic behavior. Our magnetic analyses have been mainly focused on the samples richer in $Co$ which present magnetic features significantly different with respect to those observed in the corresponding continuous films. The magnetic behavior of the sample richer in $Au$ is completely ruled by a superparamagnetic-lile behavior, consistent with the presence of very fine $Co$ clusters, in form of magnetically interacting $Co$ nanoparticles, which display the presence of magnetic relaxation processes. The study of the hysteretic properties of the samples richer in $Co$ has highlighted that the shape anisotropy induced by the nanostructuring process plays a crucial role in determining the overall hysteretic behavior leading to hyphotesize a significant reduction of the magnetoelastic anisotropy contribution to the magnetization reversal process. In this frame, the experimental observations have been supported by calculations based on a micromagnetic system modelled on the basis of the morphological features of our samples. At low $T$, the experimental evidence of the presence of a weak PMA contribution has been discussed in terms of the presence in the samples of a small amount of residual stress and/or of contribution of $Co$ nanoparticles or of very fine $Co$ clusters. As discussed in the chapter 5, further analyses should be done in order to better elucidate this last point.

In conclusion, the research work presented in this thesis demonstrates that the studied $AuCo$ nanostructures must be treated as fully-fledged composite systems; the obtained results enlarge the knowledge on nanoscale composite magnetic materials and suggest interesting implications in the prospective to obtain a fine tuning of their overall magnetic anisotropy and, accordingly, of their magnetic hysteretic properties.

# Bibliography

[1] Liu F, Hou Y and Gao S (2014) Exchange-coupled nanocomposites: chemical synthesis, characterization and applications. Chemical Society Reviews,**vol. 43**, **no. 23** : pp. 8098 - 8113.

[2] S. Gupta, R. Ranjit, C. Mitra, P. Raychaudhuri, and R. Pinto, *Appl. Phys. Lett.*, **78**, 362 (2001).

[3] Y.-H. Huang, X. Chen, Z.-M. Wang, C.-S. Liao, C.-H. Yan, H.-W. Zhao, and B.-G. Shen, J. Appl. Phys., **91**, 7733 (2002).

[4] Yoshizawa, Y.; Oguma, S.; Yamauchi, K. New Fe-based soft magnetic alloys composed of ultrafine grain structure. *J. Appl. Phys.* **1988**, 64, 6044 - 6046.

[5] Kronm*ü*ller, H.; Fischer, R.; Seeger, M.; Zern, A. Micromagnetism and microstructure of hard magnetic materials.*J. Phys. D Appl. Phys.* **1996**, 29, 2274 - 2283.

[6] Spizzo, F.; Bonfiglioli, E.; Tamisari, M.; Gerardino, A.; Barucca, G.; Notargiacomo, A.; Chinni, F.; Del Bianco, L. Magnetic exchange coupling in IrMn/NiFe nanostructures: From the continuous film to dot arrays.*Phys. Rev. B* **2015**, 91, 064410 - 064419.

[7] Prejbeanu, I.L.; Kerekes, M.; Sousa, R.C.; Sibuet, H.; Redon, O.; Dieny, B.; Noziéres, J.P. Thermally assisted MRAM.*J. Phys. Condens. Matter* **2007**, 19, 165218-165223.

[8] F. Spizzo, M. Tamisari, F. Chinni, E. Bonfiglioli, A. Gerardino, G. Barucca, D. Bisero, S. Fin, L. Del Bianco, J. Magn. Magn. Mater., **400**, 242 - 247.

[9] Dieny, B.; Speriosu, V.S.; Parkin, S.S.P.; Gurney, B.A.; Wilhoit, D.R.; Mauri, D. Giant magnetoresistive in soft ferromagnetic multilayers. *Phys. Rev. B* **1991**, 43, 1297 - 1300.

[10] W. H. Meiklejohn and C. P. Bean, *Phys. Rev.* **102**, 1413 (1956).

[11] J. Nogués and I. K. Schuller, *J. Magn. Magn. Mater.* **192**, 203 (1999).

[12] J. Nogués, J. Sort, V. Langlais, V. Skumryev, S. Suriñach, J. S. Munõz, and M. D. Baró, *Phys. Rep.* 422, 65 (2005).

[13] Fullerton, E.E.; Jiang, J.S.; Bader, S.D. Hard/soft magnetic heterostructures: Model exchange-spring magnets. *J. Magn. Magn. Mater.* **1999**, 200, 392 - 404.

[14] Wang, J.-P.; Shen, W.K.; Bai, J.M.; Victora, R.H.; Judy, J.H.; Song, W.L. Composite media (dynamic tilted media) for magnetic recording. *Appl. Phys. Lett.* **2005**, 86, 142504.

[15] Johnson, K.E. Magnetic materials and structures for thin-film recording media. *J. Appl. Phys.* **2000**, 87, 5365 - 5370.

[16] Chason, E.; Guduru, P.R. Tutorial: Understanding residual stress in polycrystalline thin films through real-time measurements and physical models.*J. Appl. Phys.* **2016**, 119, 191101 - 191121.

[17] Fernández-Martiínez, I.; Costa-Krämer, J.L.; Briones, F. Stress and magnetoelastic properties control of amorphous $Fe_{80}Bo_{20}$ thin films during sputtering deposition. *J. Appl. Phys.* **2008**, 103, 113902 - 113905.

[18] Shin, J.; Kim, S.H.; Suwa, Y.; Hashi, S.; Ishiyama, K. Control of in-plane uniaxial anisotropy of $Fe_{72}Si_{14}B_{14}$ magnetostrictive thin film using a thermal expansion coefficient. *J. Appl. Phys.* **2012**, 111, 07E511.

[19] Pandey, H.; Rout, P.K.; Anupam; Joshi, P.C.; Hossain, Z.; Budhani, R.C. Magnetoelastic coupling induced magnetic anisotropy in Co2(Fe/Mn)Si thin films. *Appl. Phys. Lett.* **2014**, 10, 022402 - 022405.

[20] Barraud, C.; Deranlot, C.; Seneor, P.; Mattana, R.; Dlubak, B.; Fusil, S.; Bouzehouane, K.; Deneuve, D.; Petroff, F.; Fert, A. Magnetoresistance in magnetic tunnel junctions grown on flexible organic substrates. *Appl. Phys. Lett.* **2010**, 96, 072502 - 072503.

[21] Dai, G.; Zhan, Q.; Liu, Y.; Yang, H.; Zhang, X.; Chen, B.; Li, R.-W. Mechanically tunable magnetic properties of $Fe_{81}Ga_{29}$ films grown on flexible substrates. *Appl. Phys. Lett.* **2012**, 100, 122407.

[22] Canet, F.; Bellouard, C.; Joly, L.; Mangin, S. Magnetic behavior of exchange - coupled $Fe_{30}Au_{70}\,/\,Fe_{65}Au_{35}$ bilayers. *Phys. Rev. B* **2004**, 69, 094402 - 094411.

[23] Toal, B.; Mc Millen, M.; Murphy, A.; Hendren, W.; Arredondo, M.; Pollard, R. Optical and magneto - optical properties of gold core cobalt shell magnetplasmonic nanowire arrays. *Nanoscale* **2014**, 6, 12905 - 12911.

[24] Bogani, L.; Cavigli, L.; de Julián Fernández, C.; Mazzoldi, P.; Mattei, G.; Gurioli, M.; Dressel, M.; Gatteschi, D. Photocoercivity of nano - stabilized Au:Fe superparamagnetic nanoparticles. *Adv. Mater.* **2010**, 22, 4054 - 4058.

[25] David, S.; Polonschii, C.; Gheorghiu, M.; Gáspár, S.; Gheorghiu, E. Magneto - plasmonic biosensor with enhanced analytical response and stability. *Biosens. Bioelectron.* **2015**, 63, 525 - 532.

[26] Li, L.; Chai, S.H.; Binder, A.; Brown, S.; Yang, S.-Z.; Dai, S. Synthesis of MCF - supported AuCo nanoparticle catalysts and the catalytic performance for the CO oxidation reaction. *RSC Adv.* **2015**, 5, 100212 - 100222.

[27] Yang, K.; Clavero, C.; Skuza, J. R.; Varela, M.; Lukaszew, R.A. Surface plasmon rsonance and magneto - optical enhancement on Au-Co nanocomposite thin films. *J. Appl. Phys.* **2010**, 107, 103924 - 103925.

[28] R. A. Lukaszew, Handbook of Nanomagnetism Applications and Tools. Taylor & Francis Group, LLC 2016.

[29] H. Okamoto, T. Massalski, T. Nishizawa, and M. Hasebe, " The Au - Co system", *Bull. Alloy Phase Diagrams*, vol. 6, no. 5, pp. 449 - 454, Oct. 1985.

[30] C. Clavero, A. Cebollada, G. Armelles, and O. Fruchart, Growth mode, magnetic and magneto-optical properties of pulsed-laser-deposited Au/Co/Au(111) trilayers, *J. Magn. Magn. Mater.*, **322**, 647 - 652 (2010).

[31] I. Nedkov and M. Ausloos (eds.), *Nano-Crystalline and Thin Film Magnetic Oxides*, 3 - 26. © 1999 Kluwer Academic Publishers.

[32] G. A. Prinz, "Spin-Polarized Transport", *Phys. Today*, vol.**48**, no.4, pp.58, 1995.

[33] G. A. Prinz, "Magnetoelectronics", *Science*, vol.**282**, no.5394, pp. 1660, 1998.

[34] S. A. Wolf, D. D. Awschalom, R. A. Buhrman, J. M. Daughton, S. von Molnar, M. L. Roukes, A. Y. Chtchelkanova and D. M. Treger, "Spintronics: A Spin-Based Electronics Vision for the Future", *Science*, vol.294, no.5546, pp.1488, 2001.

[35] I. Zutic, J. Fabian and S. Das Sarma, "Spintronics: Fundamentals and applications",*Rev. Mod. Phys.*, vol.**76**, no.2, pp. 323, 2004.

[36] S. S. P. Parkin, C. Kaiser, A. Panchula, P. M. Rice, B. Hughes, M. Samant and S. H. Yang, "Giant tunnelling magnetoresistance at room temperature with $MgO$ (100) tunnel barriers" *Nat. Mater.*, vol.**3**, pp.862, 2004.

[37] S. Yuasa, T. Nagahama, A. Fukushima, Y. Suzuki and K. Ando, "Giant room - temperature magnetoresistance in single-crystal $Fe/MgO/Fe$ magnetic tunnel junctions", *Nat. Mater.*, vol.**3**, pp.868, 2004.

[38] Y. Tserkovnyak, A. Brataas, G. E. W. Bauer and B. I. Halperin, "Nonlocal magnetization dynamics in ferromagnetic heterostructures ", *Rev. Mod. Phys.*, vol.**77**, no.4, pp.1375, 2005.

[39] W. J. Gallagher and S. S. P. Parkin, "Development of the magnetic tunnel junction MRAM at IBM: From first junctions to a 16-Mb MRAM demonstrator chip", *IBM J. Res. Dev.*, vol.**50**, no.1, pp.5, 2006.

[40] Cullity, B.D.; Graham, C.D. *Introduction to Magnetism and Magnetic Materials*, 2nd ed.; IEEE Press: Piscataway, NJ, USA, 2009.

[41] A. Aharoni, *Introduction to the Theory of Ferromagnetism* (Oxford University Press, 2000).

[42] Pei Zou, Winnie Yu and James A. Bain, *IEEE Trans. Magn.*, vol. 38, No. 5, Sep. 2002.

[43] Zhang Hao, Li Yuan-Yuan, Yang Mei-Yin, Zhang Bao, Yang Guang, Wang Shou-Guo, Wang Kai-You. Tuning the magnetic anisotropy of CoFeB grown on flexible substrates. *Chinese Physics* **B**, 24(7): 077501.

[44] Ran Wang, Ya-Xuan Shang, Rui Wu, Jin-Bo Yang, Yang Ji, *Chin. Phys. Lett.* Vol. 33, No. 4 (2016) 047502.

[45] C. Sommers, J. Zabloudil, C. Uiberacker, P. Weinberger, and L. Szunyogh, *Phys. Rev. B* **58**, 5539 (1998).

[46] A. Kukunin, J. Prokop, and H. J. Elmers, *Phys. Rev. B* **76**, 134414 2007.

[47] R. Allenspach, M. Stampanoni, and A. Bischof, *Phys. Rev. Lett.* **65**, 3344 (1990).

[48] S. Puütter, H. F. Ding, Y. T. Millev, H. P. Oepen, and J. Kirschner, *Phys. Rev. B* **64**, 092409 2001.

[49] F. El Gabaly, S. Gallego, C. Muoz, L. Szunyogh, P. Weinberger, C. Klein, A. K. Schmid, K. F. McCarty, and J. de la Figuera, *Phys. Rev. Lett.* **96**, 147202 2006 .

[50] B. Schulz and K. Baberschke, *Phys. Rev. B* **50**, 13467 1994 .

[51] M. Coïsson, F. Celegato, E. Olivetti, P. Tiberto, F. Vinai, and M. Baricco, *J. Appl Phys.* **104**, 033902 (2008).

[52] Nobuo Saito, Hideo Fujiwara and Yutaka Sugita, *J. Phys. Soc. Jpn.*, vol. 19, No. 7, July, 1964.

[53] A. O. Adeyeye, S. Goolaup, N. Singh, W. Jun, C. C. Wang, S. Jain and D. Tripathy, "Reversal Mechanisms in Ferromagnetic Nanostructures", *IEEE Trans. Magn.*, vol.44, no.7, pp.1935, 2008.

[54] C. C. Wang, A. O. Adeyeye and N. Singh, "Magnetic and transport properties of multilayer nanoscale antidot arrays", *Appl. Phys. Lett.*, vol.88, no.22, pp. 222506, 2006.

[55] V. M. Prida, K. R. Pirota, D. Navas, A. Asenjo, M. Herna?ndez-Va?lez and M. Va?zquez, "Self-Organized Magnetic Nanowire Arrays Based on Alumina and Titania Templates", *J. Nanosci. Nanotechnol.*, vol.7, pp.272-85, 2007.

[56] P. Vavassori, V. Metlushko, R. M. Osgood, III,, M. Grimsditch, U. Welp, G. Crabtree, Wenjun Fan, S. R. J. Brueck, B. Ilic and P. J. Hesketh "Magnetic information in the light diffracted by a negative dot array of Fe", *Phys. Rev. B*, vol.59, no.9, pp.6337, 1999.

[57] I. Guedes, M. Grimsditch, V. Metlushko, P. Vavassori, R. Camley, B. Ilic, P. Neuzil, and R. Kumar, "Domain formation in arrays of square holes in an Fe film", *Phys. Rev. B*, vol. 66, no. 1, pp. 014434, 2002.

[58] I. Guedes, N. J. Zaluzec, M. Grimsditch, V. Metlushko, P. Vavassori, B. Ilic, P. Neuzil, and R. Kumar, "Magnetization of negative magnetic arrays: Elliptical holes on a square lattice", *Phys. Rev. B*, vol. 62, no.11, pp. 719, 2000.

[59] C. C. Wang, A. O. Adeyeye, and N. Singh, "Magnetic antidot nanostructures: effect of lattice geometry", *Nanotechnology*, vol. 17, no.6, pp. 1629, 2006.

[60] P. Vavassori, G. Gubbiotti, G. Zangari, C.T. Yu, H. Yin, H. Jiang, G.J. Mankey, "Magnetization reversal in micro-size negative dot arrays in permalloy film", *J. Magn. Magn. Mater.*, vol. 242-245, no. 1, pp. 585, 2002.

[61] P. Vavassori, G. Gubbiotti, G. Zangari, C. T. Yu, H. Yin, H. Jiang, and G. J. Mankey, "Lattice symmetry and magnetization reversal in micron-size antidot arrays in Permalloy film", *J. Appl. Phys.*, vol.91, no.10, pp. 7992, 2002.

[62] N. G. Deshpande, M. S. Seo, X. R. Jin, S. J. Lee, Y. P. Lee, J. Y. Rhee, and K. W. Kim, "Tailoring of magnetic properties of patterned cobalt antidots by simple manipula- tion of lattice symmetry", *Appl. Phys. Lett.*, vol. 96, no. 12, pp. 122503-3, 2010.

[63] D. Tripathy and A. O. Adeyeye, *New J. Phys.* **13**, 023035 (2011).

[64] J. Gräfe, M. Weigand, N. Träger, G. Schütz, E. J. Goering, M. Skripnik, U. Nowak, F. Haering, P. Ziemann, and U. Wiedwald, *Phys. Rev. B* **93**, 104421 (2016).

[65] C. T. Yu, H. Jiang, L. Shen, P. J. Flanders, and G. J. Mankey, "The magnetic anisotropy and domain structure of permalloy antidot arrays", *J. Appl. Phys.*, vol.87, no.9, pp.6322, 2000.

[66] F. García-Sánchez, E. Paz, F. Pigazo, O. Chubykalo-Fesenko, F. J. Palomares, J. M. González, F. Cebollada, J. Bartolomeé and L. M. Garciía, "Coercivity mechanisms in lithographed antidot arrays", *EuroPhysic. Lett.*, vol.84, no. 6, pp. 67002, 2008.

[67] A.Zvezdin and V.Kotov. *Modern magnetooptics and magnetooptical materials.* Taylor & Francis Group, New York, 1997.

[68] G. R. Fowles, *Introduction to Modern Optics* (Dover Publications, Inc., 1989).

[69] You C. Y., Shin S. C.; *J. Appl. Phys.*; 84 (1998) 541

[70] C. A. F. Vaz, J. A. C. Bland, and G. Lauhoff, Rep. Prog. Phys. **71**, 056501 (2008).

[71] S. D. Bader, J. Magn. Magn. Mater. **100**, 440 (1991) .

[72] V. Antonov, B. Harmon and A. Yaresko. *Electronic Structure and Magneto-Optical properties of Solids.* Kluwer Academic Publishers, Moscow, 2004.

[73] P. Vavassori; J. Appl. Phys; 77 (2000) 1605.

[74] J. Zak, E. R. Moog, C. Liu, and S. D. Bader, *Phys. Rev. B* **43**, 6423 1991.

[75] "Exchange coupling and spatial confinement in IrMn/NiFe films and nanodots" Master Degree Thesis, Chinni Federico.

[76] Quantum Design; MPMS XL Options Manual (1999)

[77] B.D. Josephson, *Phys. Lett.*, Vol. 1 pp. 251 - 253, 1962.

[78] T. Van Duzer and C. W. Turner, Superconductive devices and Circuits *Prentice Hall PTR*, QC611.92V36 2nd ed. 1998.

[79] V. Mattarello, PhD Thesis " Au-Co Thin Films and Nanostructures for MagnetoPlasmonics" Department of Chemical Sciences, University of Padua, Italy (2016).

[80] Maurizio, C.; Michieli, N.T.; Kalinic, B.; Mattarello, V.; Bello, V.; Wilhelm, F.; Ollefs, K.; Mattei, G. Local structure and X-ray magnetic circular dichroism of $Au$ in $Au - Co$ nanoalloys. *Applied Surface Science* 433 (2018) 596-601.

[81] Wohlfarth E. P. 1980 *Ferromagnetic Materials* vol. 1 ed E. P. Wohlfarth (Amsterdam: North-Holland) p. 1.

[82] T. Haubold, R. Birringer, B. Lengeler, and H. Gleiter, Phys. Lett. A 135, 461 (1989).

[83] U. Herr, J. Jng, R. Birringer, U. Gonser, and H. Gleiter, Appl. Phys. Lett. 50, 472 (1987).

[84] W. Wagner, A. Wiedenmann, W. Petry, A. Geibel, and H. Gleiter, J. Mater. Res. 6, 2305 (1991).

[85] Beaujour, J.-M.L.; Lee, J.H.; Kent, A.D.; Krycka, K.; Kao, C.-C. Magnetization damping in ultrathin polycrystalline Co films: Evidence for nonlocal effects.*Phys Rev. B* **2006**, 74, 214405 - 214408.

[86] Dormann, J.L.; Fiorani, D.; Tronc, E. Magnetic Relaxation in Fine-Particle Systems. *In Advances in Chemical Physics*; Prigogine, I., Stuart, A.R., Eds.; J. Wiley & Sons, Inc.: New York, NY, USA, 1997; Volume XCVIII, pp. 283 - 494.

[87] Del Bianco, L.; Fiorani, D.; Testa, A.M.; Bonetti, E.; Savini, L.; Signoretti, S. Magnetothermal behavior of a nanoscale Fe/Fe oxide granular system. *Phys. Rev.* **B** 2002, 66, 174418.

[88] M. J. O'Shea, H. Jiang, P. Perera, and H. H. Hamdeh, *J. Appl. Phys.* **87**, 6137 (2000).

[89] S. Esho, *Jpn. J. Appl. Phys., Suppl.* **15**, 93 (1976).

[90] M. J. O'Shea and A. Al-Sharif, *J. Appl. Phys.* **75**, 6673 (1994).

[91] Y. Z. Wu, G. S. Dong, and X. F. Jin, *Phys. Rev. B* **64**, 214406 (2001).

[92] M. Ziese, I. Vrejoiu, and D. Hesse, *Appl. Phys. Lett.* **97**, 052504 (2010).

[93] L. V. Tho, C. G. Kim, and C. O. Kim, *J. Appl. Phys.* **103**, 07B906 (2008).

[94] S. M. Valvidares, L. M. Alvarez-Prado, J. I. Martin, and J. M. Alameda, *Phys. Rev. B* **64**, 134423 (2001).

[95] B. Mora, N. Soriano, C. Redondo, A. Arteche, D. Navas, and R. Morales, **Nano Res**. 2016, 9(8): 2347 - 2353.

[96] X. Yan and Y. Xu, *J. Appl. Phys.* **79**, 6013 (1996).

[97] R. K. Zheng, H. Liu, Y. Wang, and X. X. Zhang, *J. Appl. Phys.* **96**, 5370 (2004).

[98] J. Y. Yang, J. H. Kim, J. S. Lee, S. J. Woo, J. S. Kwak, J. P. Hong, and M. H. Jung, *Phys. Rev. B* **78**, 094415 (2008).

[99] B. S. Chun, S. D. Kim, Y. S. Kim, J. Y. Hwang, S. S. Kim, J. R. Rhee, T. W. Kim, J. P. Hong, M. H. Jung, and Y. K. Kim, *Acta. Mater.* **58**, 2836 (2010).

[100] F. Chinni, F. Spizzo, F. Montoncello, V. Mattarello, C. Maurizio, G. Mattei and L. Del Bianco, *Materials* **2017**, *10*, 717.

[101] Donahue M. J., Porter D. G.; OOMMF User's Guide, Version 1.0 Interagency Report NISTIR 6376 (National Institute of Standards and Technology, Gaithersburg, MD, 1999).

[102] Eyrich, C.; Huttema, W.; Arora, M.; Montoya, E.; Rashidi, F.; Burrowes, C.; Kardasz, B.; Girt, E.; Heinrich, B.; Mryasov, O.N.; et al. Exchange stiffness in thin film Co alloys. *J. Appl. Phys.* **2012**, 111, 07C919.

[103] Arcas, J.; Hernando, A.; Barandiaran, J.M.; Prados, C.; Vazquez, M.; Mari?n, P.; Neuweiler, A. Soft to hard magnetic anisotropy in nanostructured magnets. *Phys. Rev. B* **1998**, 58, 5193 - 5196.

[104] Stoner, E.C.; Wohlfarth, E.P. A mechanism of magnetic hysteresis in heterogeneous alloys. *IEEE Trans. Magn.* **1991**, 27, 3475 - 3518.

[105] Herzer, G. Grain size dependence of coercivity and permeability in nanocrystalline ferromagnets. *IEEE Trans. Magn.* **1990**, 26, 1397-1402.

[106] T. R. McGuire, J. A. Aboaf, and E. Klokholm, *J. Appl. Phys.*, Vol **52**, No. 3, March 1981.

[107] Serbena, F.C.; Zanotto, E.D. Internal residual stresses in glass-ceramics: A review. *J. Non-Cryst. Sol.* **2012**, 358, 975-984.

[108] Hsueh, C.H.; Becher, P.F. Residual thermal stresses in ceramic composites. Part I: With ellipsoidal inclusions. *Mater. Sci. Eng. A* **1996**, 212, 22 - 28.

[109] Stoney, G.G. The Tension of Metallic Films Deposited by Electrolysis. *Proc. R. Soc. Lond. Ser. A* **1909**, A82, 172-175.

[110] Feng, X.; Huang, Y.; Rosakis, A.J. On the Stoney formula for a thin film/substrate system with nonuniform substrate thickness. *J. Appl. Mech.* **2007**, 74, 1276 - 1281.

[111] Lee, H.; Rosakis, A.J.; Freund, L.B. Full-field optical measurement of curvatures in ultra-thin-film-substrate systems in the range of geometrically nonlinear deformations. *J. Appl. Phys.* **2001**, 89, 6116 - 6129.

[112] Huang, Y.; Ngo, D.; Rosakis, A.J. Non-uniform, axisymmetric misfit strain: In thin films bonded on plate substrates/substrate systems: The relation between non-uniform film stresses and system curvatures. *Acta Mech. Sin.* **2005**, 21, 362 - 370.

[113] Sara Laureti, Sarah Y. Suck, Helge Haas, Eric Prestat, Olivier Bourgeois, and Dominique Givord, *PRL* **108**, 077205 (2012).

[114] Alvarez-Prado L. M.,Pérez G. T., Morales R., Salas F. H. and Alameda J. M. 1997 *Phys. Rev.* **B** 56 3306.

[115] Fujiwara H., Sugita Y. and Saito N. 1964 *Appl. Phys. Lett.* **4** 199.

[116] JimBae Kim, Hiro Akinaga, and Jongryoul Kim, *Appl. Phys. Lett.* **98**, 102511 (2011).

[117] Y. Sugita and H. Fujiwara, *J. Phys. Soc. Jpn.*, vol. 20, no. 1, pp. 98 - 102, 1965.

[118] E. E. Huber and D. O. Smith, J. Appl. Phys., vol. 30, no. 4, pp. 267S - 269S, 1959.

[119] A. Hierro-Rodriguez et al., *J. Phys. D : Appl. Phys.* **46** (2013) 345001 (9pp).

[120] Hubert A. and Schäfer R. 1998 Magnetic Domains (Berlin: Springer).

[121] Y. Murayama, "Micromagnetics on stripe domain films. I. Critical cases," *J. Phys. Soc. Jpn.*, vol. 21, no. 11, pp. 2253-2266, 1966.

[122] P. Sharma, H. Kimura, A. Inoue, E. Arenholz, and J. H. Guo, *Phys. Rev. B* **73**, 052401 (2006).

[123] M. Platea, W. Brückner, H. Wendrock, R. Koch and R. Kaltofen, *J. Appl. Phys.* **99**, 033509 (2006).

[124] John C. Hulteen. Nanosphere lithography: A materials general fabrication process for periodic particle array surfaces. Journal of Vacuum Science & Technology A: Vacuum, Surfaces, and Films, 13(3):1553, may 1995.

[125] C. L. Haynes and R. P. Van Duyne. Nanosphere lithography: A versatile nanofabrication tool for studies of Size-Dependent nanoparticle optics. The Journal of Physical Chemistry B, 105(24):5599-5611, June 2001.

[126] Joachim Gräfe, Felix Haering, Thomas Tietze, Patrick Audehm, Markus Weigand, Ulf Wiedwald, Paul Ziemann, Przemysłlaw Gawroński, Gisela Schütz and Eberhard J. Goering, *Nanotechnology* 26 (2015) 225203 (6pp).

[127] S. Voltan, C. Cirillo, H. J. Snijders, K. Lahabi, A. García-Santiago, J. M. Hernández, C. Attanasio, and J. Aarts, *Phys. Rev.* **94**, 094406 (2016).

[128] Y. Murayama, *J. Phys. Soc. Jpn.* **21**, 2253 (1966).